The Dissertation Committee for Biwei Yin Certifies that this is the approved version of the following dissertation:

Optical Coherence Tomography for Retinal Diagnostics

Committee:

Thomas E. Milner, Supervisor

Henry G. Rylander III, Co-Supervisor

Michael F. Becker

Mikhail A. Belkin

Martin Poenie

James W. Tunnell

Optical Coherence Tomography for Retinal Diagnostics

by

Biwei Yin, B. E.; M. S. E.

Dissertation

Presented to the Faculty of the Graduate School of

The University of Texas at Austin

in Partial Fulfillment

of the Requirements

for the Degree of

Doctor of Philosophy

The University of Texas at Austin

August 2013

Dedication

To my parents for their unwavering support and to my wife for her encouragement.

Acknowledgements

I would like to thank my supervisor Dr. Thomas E. Milner who trained me in optical imaging system development. With his guidance, I am able to analyze problems more logically and solve problems more efficiently.

Thanks to co-supervisor Dr. Henry G. Rylander III who taught me how to design a medical imaging system more suitable for clinical application and helped me to extract useful information from clinical measurement data.

Thanks to Dr. Roman V. Kuranov, who made great contribution in the development of Dual-Wavelength Photothermal OCT.

Many thanks to my colleagues in biomedical engineering laser laboratory: Jordan Dwelle, Badr Elmaanaoui, Amit Paranjape, Shuang Liu, Bingqing Wang, Austin McAlroy, Jinze Qiu and Tianyi Wang, without whose help I could not finish projects on time.

Optical Coherence Tomography for Retinal Diagnostics

Biwei Yin, Ph.D.

The University of Texas at Austin, 2013

Supervisor: Thomas E. Milner

Co-supervisor: Henry G. Rylander III

Optical Coherence Tomography (OCT) is a non-invasive three-dimensional imaging technique. OCT synthesizes a cross-sectional image from a series of lateral adjacent depth scans, and with a two-dimensional scanning scheme, three-dimensional intensity image of sample can be constructed. Due to its non-invasive capability, OCT has been widely applied in ophthalmology, cardiology and dermatology; and in addition to three-dimensional intensity image construction, various functional OCT imaging techniques have been developed for clinical application. My research is focused on developing functional OCT systems for application in ophthalmology, including polarization-sensitive optical coherence tomography (PS-OCT) for retinal nerve fiber layer (RNFL) birefringence measurement and dual-wavelength photothermal optical coherence tomography (DWP-OCT) for microvasculature blood oxygen saturation (SO_2) measurement.

In the study, a single-mode-fiber based polarization-sensitive swept-source OCT (PS-SS-OCT) with polarization modulator, polarization-sensitive bulk-optics balanced

detection module is constructed and polarization processing methods based on Stokes vectors are applied to determine birefringence. PS-OCT is able to provide human subject's RNFL thickness, phase retardation, and birefringence information. Degradation in the degree of polarization (DOP) along depth is investigated and its difference between four quadrants of RNFL (superior, temporal, inferior and nasal) indicates the structural property difference.

DWP-OCT is a novel functional OCT system consisting of a phase-sensitive optical coherence tomography system (PhS-OCT) and two photothermal excitation lasers. PhS-OCT is based on a swept-source laser operating in the 1060 nm wavelength range; the two photothermal excitation lasers with wavelength 770 nm and 800 nm are intensity modulated at different frequencies. PhS-OCT probe beam and two photothermal excitation beams are combined and incident on the sample, optical pathlength (*op*) change on the sample introduced by two photothermal excitation beams are measured and used for blood SO_2 estimation.

A polarization microscope is proposed for future study. The polarization microscope is an imaging technique providing molecular structure and orientation based on probe light's polarization state information. The polarization microscope uses a wavelength tunable light source, and can achieve any incident polarization state by a retarder-rotator combination. Specimen's birefringence can be determined based on the changing of detected light amplitude.

Table of Contents

List of Tables

List of Figures

Chapter 1: Introduction

1.1 Organization of Dissertation

Chapter 1 is the introduction and briefly describes the history and development of optical coherence tomography (OCT) as an imaging technique. Important concepts for OCT imaging system are identified, discussed and illustrated. Different mathematical representations of light are introduced. Finally, application of OCT in ophthalmology is discussed and the motivation of this study is presented.

In chapter 2, polarization-sensitive optical coherence tomography (PS-OCT) is introduced as a useful functional OCT imaging technique. A single-mode fiber based clinical PS-OCT system and polarization processing methods are described; thickness, phase retardation and birefringence maps of human retinal nerve fiber layer (RNFL) are presented. Polarization processing method is developed to investigate the degradation of the degree of polarization (DOP) in human RNFL; clinical data is analyzed and found to indicate differences in structural properties between four quadrants (superior, temporal, inferior and nasal). An angle-resolved OCT system design is proposed based on pathlength multiplexing and a polarization-sensitive fiber-optic balanced detection module is designed.

Chapter 3 describes a novel functional OCT system: dual-wavelength photothermal optical coherence tomography (DWP-OCT). DWP-OCT incorporates microvasculature blood oxygen saturation (SO_2) measurement capability into OCT imaging technique. DWP-OCT system instrumentation and blood SO_2 estimation algorithm is provided. Phantom microvessel experiment is presented as well as measurement error analysis. An analytical model based on bioheat equation is

constructed to consider the thermal diffusion's impact on DWP-OCT blood SO_2 measurement.

Chapter 4 presents the design of a spectrally-encoded high-extinction polarization microscope, which is able to provide molecular structure and orientation based on probe light's polarization state transformation. The novel design has the capability to rapidly modulate polarization state of the incident light and can be operated in both null and non-null measurement modes.

1.2 Optical Coherence Tomography

With the invention of the laser in the early 1960s, the coherence properties of light have been utilized in various optical imaging techniques. Optical coherence tomography (OCT) is one of the optical tomography techniques based on coherence properties of light, and is of particular importance in the medical field since its invention and introduction in early 1990s. OCT is a non-invasive three-dimensional (3D) imaging technique providing advantages over competing methods in axial and lateral resolution. OCT synthesizes a cross-sectional image (B-scan image) from a series of laterally adjacent depth-scans (A-scans), and a 3D image of the sample can be constructed by recording multiple adjacent B-scans. OCT was introduced in 1991 (1) first as a time domain (TD) approach and later as a frequency domain (FD) method (2-3).

Time domain OCT is based on the principles of reflectance low-coherence interferometry (LCI) (4). A typical time domain OCT is a Michelson interferometer with the sample positioned in one arm and a mirror in reference arm; signal is acquired by translating reference mirror continuously along beam axis.

Fourier domain OCT includes spectrometer-based FD-OCT and swept-source OCT. Based on the Wiener-Khinchin theorem, in one A-scan, depth information can be provided by computing an inverse Fourier Transform of the spectrum of the backscattered and interfering light. Imaging speed is greatly improved in FD-OCT compared with TD-OCT since scanning of a reference mirror is not required. The spectrum of the backscattered light can be obtained in two instrumentation approaches: spectrometer based detection technique and a wavelength tunable laser source. FD-OCT was first presented as a spectrometer-based OCT system, and later with the advance of laser technology, swept-source lasers have played an important role in OCT imaging technique. In a swept-source OCT system, the spectrum of the backscattered light is encoded in time by serially and rapidly tuning the wavelength of laser emitting light. For equivalent signal-to-noise ratio (SNR), swept-source OCT with balanced detection provides a higher acquisition rate compared with spectrometer-based FD-OCT. Recently, swept-source OCT with A-scan rates up to 5 MHZ has been demonstrated using a Fourier domain mode locked (FDML) laser (5).

1.3 RESOLUTION, SENSITIVITY AND SNR

The quality of an OCT imaging system is usually described in terms of its resolution, sensitivity and signal-to-noise ratio (SNR).

OCT resolution includes axial and lateral resolution. Axial resolution is primarily determined by the power spectrum of the light source. The power spectrum of many light sources used in OCT can be approximated by a Gaussian spectrum, full-width-at-half-maximum (FWHM) of its autocorrelation function is provided as OCT's axial resolution as in Eq. 1.1, where $\overline{\lambda}$ is the center wavelength and $\Delta\lambda$ is the bandwidth. Light

sources with a broader bandwidth and operated at a shorter center wavelength range provides a higher axial-resolution.

$$r_z = \frac{2\ln 2\bar{\lambda}^2}{\pi\Delta\lambda} \tag{1.1}$$

Lateral resolution depends on the wavelength $\bar{\lambda}$, and sample arm imaging optics. In the focus, the lateral resolution (r_x) is given by the focus diameter in Eq. 1.2, where f is the focal length of the objective and d is the diameter of the incident beam size. Rayleigh range is defined as the single-sided depth range over which the lateral resolution is maintained within a factor of $\sqrt{2}$. Rayleigh range z_r is written in Eq. 1.3, and depth of focus is defined as twice of Rayleigh range. We can see the trade-off between lateral-resolution and depth of focus: a system with a finer lateral-resolution corresponds to a shorter depth of focus.

$$r_x = \frac{4\bar{\lambda} f}{\pi d} \tag{1.2}$$

$$z_r = \frac{\pi r_x^2}{4\bar{\lambda}} \tag{1.3}$$

The optical resolution introduced above defines the best theoretical resolution in axial direction (Z) and lateral dimension (XY). In reality, spatial sampling density is another important factor to consider. Spatial sampling density in lateral dimension is the distance between consecutive A-scans in X and between consecutive B-scans in Y; spatial sampling density in Z can be set arbitrarily by selecting the Fourier-transform length of the spectrum. True resolution of the OCT image is determined by a combination of optical resolution and spatial sampling density, and it defines the size of the smallest feature that can be visualized on the sample image (6). And according to Nyquist theorem, at least two spatial samples are required for point spread function in each dimension.

Sensitivity of OCT system is defined as the lowest signal that can be detected over the noise floor (7). Sensitivity is closely related to the signal-to-noise ratio (SNR) of the system. For a simple Michelson interferometer as shown in Fig. 1.1, the photocurrent for the interference signal of a point reflector from the sample arm and reference signal from a mirror can be written as Eq. 1.4, where I_d is the photocurrent, R is the responsivity of the photodetector, P_{ref} and P_{sam} are the power returning from reference and sample arms, $\Delta\phi$ is the phase difference of the signals returning from two arms.

$$I_d(t) = R[P_{ref} + R_{sam} + 2\sqrt{P_{ref} P_{sam}} \cos\Delta\phi(t)] \tag{1.4}$$

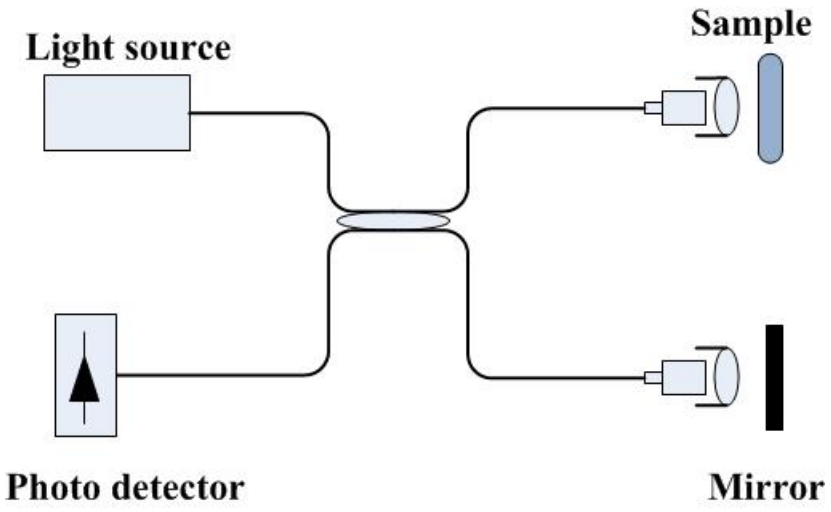

Figure 1.1: A fiber Michelson interferometer.

Power returning from reference arm is normally much larger than that from sample arm, so that the SNR of the above system can be expressed as in Eq. 1.5, where k_B is Boltzmann's constant, T is temperature, Δf and R_{eff} is the measurement bandwidth and effective noise resistance of receiver, e is charge of one electron, and RIN is relative intensity noise (RIN). Three terms in the denominator represent three major noise sources for an OCT system: thermal noise, shot noise and intensity noise.

$$SNR = \frac{2R^2 P_{ref} P_{sam}}{4k_B T \Delta f / R_{eff} + 2eRP_{ref}\Delta f + (RIN)R^2 {P_{ref}}^2 \Delta f} \tag{1.5}$$

A shot-noise limited condition refers to the condition when shot noise is the dominant noise source in the system. Under this condition, the sensitivity for a shot-noise limited system is estimated as

$$sensitivity_{snl} = 10 * \log \frac{RP_{sam}\tau}{e} \tag{1.6}$$

Where τ is the detector integration time.

From Eq. 1.5, we can see that reference power can represent the major noise source for OCT systems. When the intensity noise is dominant in the system, increasing source power will increase both numerator and denominator at the same rate, which means under this condition, increasing source power is not able to improve system SNR; SNR is proportional to P_{sam}/P_{ref}, so attenuating the reference power can improve SNR when intensity noise is dominant (8).

1.4 FUNDAMENTAL OF LIGHT

1.4.1 Maxwell's Equations

Maxwell's equations are the foundation of classical optics, it can be written as:

$$\begin{aligned} \nabla \bullet \vec{D} &= \rho \\ \nabla \bullet \vec{B} &= 0 \\ \nabla \times \vec{E} &= -\frac{\partial \vec{B}}{\partial t} \\ \nabla \times \vec{H} &= \vec{J} + \frac{\partial \vec{D}}{\partial t} \end{aligned} \tag{1.7}$$

Where $\nabla \bullet$ is divergence operator, $\nabla \times$ is curl operator, $\vec{D}$ is electric displacement in the unit of C/m^2, $\vec{B}$ is magnetic induction in the unit of Weber/m^2, $\vec{E}$ is electric field in

the unit of V/m, $\vec{H}$ is magnetic field in the unit of A/m, ρ is free charge density in the unit of C/m^3 and $\vec{J}$ is free current density in the unit of A/m^2.

To describe the material's behavior under the influence of the field, material equations are usually used. For a time-harmonic field, if it is isotropic and the bodies are at rest, the material equations can be written in a simple form:

$$\begin{aligned} \vec{J} &= \sigma \vec{E} \\ \vec{D} &= \varepsilon \vec{E} \\ \vec{B} &= \mu \vec{H} \end{aligned} \tag{1.8}$$

Where σ is conductivity in the unit of siemens/m, ε is permittivity in the unit of farads/m and μ is permeability in the unit of N/A^2. Permittivity and permeability can usually be written as in Eq. 1.9 where ε_0 is permittivity of free space (8.854…×10^{-12} F/m), ε_r is relative permittivity of material, μ_0 is permeability of free space (1.256…×10^{-6} N/A^2), μ_r is relative permittivity of material, usually equals 1. In some cases, the material property can't be described in such simple way, such as when the optical field is strong enough to introduce nonlinear effects.

$$\begin{aligned} \varepsilon &= \varepsilon_0 \varepsilon_r \\ \mu &= \mu_0 \mu_r \end{aligned} \tag{1.9}$$

In a region such as vacuum, no charges and no currents, Maxwell's equations can be simplified into wave equation to describe the wave motion (Eq. 1.10).

$$\begin{aligned} \nabla^2 \vec{E} - \frac{1}{v^2} \frac{\partial^2 \vec{E}}{\partial t^2} &= 0 \\ \nabla^2 \vec{H} - \frac{1}{v^2} \frac{\partial^2 \vec{H}}{\partial t^2} &= 0 \\ v &= 1/\sqrt{\mu_0 \mu_r \varepsilon_0 \varepsilon_r} \end{aligned} \tag{1.10}$$

v represents the velocity of wave, the velocity of light *c* in free space and refractive index of material *n* has the relation as in Eq. 1.11

$$v = c / n$$
$$c = 1/\sqrt{\mu_0 \varepsilon_0} \tag{1.11}$$
$$n = \sqrt{\mu_r \varepsilon_r}$$

1.4.2 Harmonic Waves and Wave Packets

In a homogeneous medium in region free of charges and currents, assume optical field $\vec{E}$:

$$\vec{E} = E_x \hat{x} + E_y \hat{y} + E_z \hat{z} \tag{1.12}$$

$\hat{x}$, $\hat{y}$ and $\hat{z}$ represent the unit vector for the Cartesian coordinate and each component of the field vector satisfies the wave equation in Eq. 1.10. A general time-harmonic, real, scalar plane wave of frequency ω propagating in the direction of $\hat{s}$ can be defined as a real solution of the wave equation:

$$E(\vec{r},t) = a(\vec{r})\cos[\omega(t - \frac{\vec{r} \bullet \hat{s}}{v}) + \delta] \tag{1.13}$$

Where $a(\vec{r})$ is the amplitude, $\omega(t - \frac{\vec{r} \bullet \hat{s}}{v}) + \delta$ is the phase, $\vec{r}$ is a vector that represents propagation path and δ is a constant. Wave number k is defined as

$$k = \frac{\omega}{v} = \frac{n\omega}{c} \tag{1.14}$$

And wave vector represents wave propagation direction

$$\vec{k} = k\hat{s} \tag{1.15}$$

To simplify Eq. 1.13 by using exponential, we have

$$E(\vec{r},t) = \mathrm{Re}\{a(\vec{r})e^{i(\vec{k} \bullet \vec{r} - \delta)}e^{-i\omega t}\} \tag{1.16}$$

For the linear operation, we can directly operate with the complex function in Eq. 1.16.

In the real world, waves are regarded as a superposition of monochromatic waves of different frequencies:

$$E(\vec{r},t) = \int_0^\infty a_\omega(\vec{r})\cos[\omega t - g_\omega(\vec{r})]d\omega \tag{1.17}$$

Where $g_\omega(\vec{r})$ is the wave phase surface.

Consider the superposition of plane monochromatic waves, the group velocity (v_g) and phase velocity (v_p) are written as in Eq. 1.18, where $\overline{\omega}$ and $\overline{k}$ are the mean of frequency and wave number

$$\begin{aligned} v_g &= \frac{d\omega}{dk} \\ v_p &= \frac{\overline{\omega}}{\overline{k}} \end{aligned} \tag{1.18}$$

The wave number becomes

$$k(\omega) = n(\omega)\frac{\omega}{c} \tag{1.19}$$

In Eq. 1.19, dispersion is considered, only when refractive index n is independent of ω, group velocity and phase velocity are equal.

1.4.3 Polarization of Light

For a monochromatic plane wave, the electric and magnetic field vectors are on the plane normal to the wave vector: $\vec{E}$, $\vec{H}$ and $\hat{s}$ form a right-handed orthogonal triad of vectors with the relation:

$$\sqrt{\mu}\left|\vec{H}\right| = \sqrt{\varepsilon}\left|\vec{E}\right| \tag{1.20}$$

By choosing the propagation direction of the wave along the z axis, Eq. 1.12 has field components on x-y plane.

$$\vec{E} = E_x\hat{x} + E_y\hat{y} \tag{1.21}$$

Where E_x and E_y can be written in terms of amplitude A and phase φ.

$$\begin{aligned} E_x &= \mathrm{Re}(A_x e^{-i\varphi_1}) \\ E_y &= \mathrm{Re}(A_y e^{-i\varphi_2}) \\ \varphi_1 &= \omega t - \vec{k}\bullet\vec{r} + \delta_1 \\ \varphi_2 &= \omega t - \vec{k}\bullet\vec{r} + \delta_2 \end{aligned} \tag{1.22}$$

Rewrite Eq. 1.22 and the equation can be derived to describe the locus of the points with coordinates (E_x, E_y).

$$(\frac{E_x}{A_x})^2 + (\frac{E_y}{A_y})^2 - 2\frac{E_x E_y}{A_x A_y}\cos(\varphi_2 - \varphi_1) = \sin^2(\varphi_2 - \varphi_1) \tag{1.23}$$

Two special cases can be derived from Eq. 1.23. One is linear polarization, which is when

$$\varphi_2 - \varphi_1 = m\pi \tag{1.24}$$

(m=0, ±1, ±2, …). At this condition, Eq. 1.23 can be written as Eq. 1.25:

$$\frac{E_x}{E_y} = (-1)^m \frac{A_x}{A_y} \tag{1.25}$$

The other case is circular polarization, which is when

$$\begin{aligned} \varphi_2 - \varphi_1 &= \frac{\pi}{2} + m\pi \\ A_x &= A_y = A \end{aligned} \tag{1.26}$$

(m=0, ±1, ±2, …). And at this condition, Eq. 1.23 is simplified to Eq. 1.27:

$$(\frac{E_x}{A})^2 + (\frac{E_y}{A})^2 = 1 \tag{1.27}$$

The polarization state of light can usually be presented in two mathematical formalisms: Jones vectors and Stokes parameters.

1.4.4 Jones vectors, coherency matrix and Stokes parameters

The complex representation of a field (as the complex function in Eq. 1.16) is frequently used and is called the analytic signal (9). The real signal can be found by taking the real part of the analytic signal. Jones vectors are based on a complex representation of the field. Jones vectors consist of the complex amplitude in x-axis and y-axis when assuming fully polarized light propagating along z-axis.

$$\begin{pmatrix} E_x \\ E_y \end{pmatrix} = \begin{pmatrix} A_x e^{i(\vec{k}\bullet\vec{r}-\omega t-\delta_1)} \\ A_y e^{i(\vec{k}\bullet\vec{r}-\omega t-\delta_2)} \end{pmatrix} \tag{1.28}$$

And the intensity of the field I is the sum of amplitude squares of two orthogonal components written as:

$$I = E_x E_x^{*} + E_y E_y^{*} = A_x^{2} + A_y^{2} \tag{1.29}$$

Jones vectors indicate the amplitude and relative phase retardation between two orthogonal field components. Jones matrices are 2 by 2 matrices which can be operated on Jones vectors to describe the polarization state transformation when light propagates through a series of optical elements.

Consider a quasi-monochromatic light wave with mean frequency $\bar{\omega}$ propagated in the positive z-direction, its E_x and E_y are:

$$\begin{aligned} E_x(t) &= A_x(t)e^{i[\phi_1(t)-\bar{\omega}t]} \\ E_y(t) &= A_y(t)e^{i[\phi_2(t)-\bar{\omega}t]} \end{aligned} \tag{1.30}$$

Its coherency matrix J (10) can be written as

$$J = \begin{bmatrix} J_{xx} & J_{xy} \\ J_{yx} & J_{yy} \end{bmatrix} = \begin{bmatrix} \langle E_x E_x^{*} \rangle & \langle E_x E_y^{*} \rangle \\ \langle E_y E_x^{*} \rangle & \langle E_y E_y^{*} \rangle \end{bmatrix} = \begin{bmatrix} \langle A_x^{2} \rangle & \langle A_x A_y e^{i(\phi_1-\phi_2)} \rangle \\ \langle A_x A_y e^{-i(\phi_1-\phi_2)} \rangle & \langle A_y^{2} \rangle \end{bmatrix} \tag{1.31}$$

$\langle\ \rangle$ is used to represent an ensemble average or time average under the assumption of ergodicity. The trace of the coherency matrix equals the total intensity of the light. Moreover, since the non-diagonal elements are in general complex and conjugates of each other, J is said to be a Hermitian matrix. Normalized J_{xy}, we have

$$j_{xy} = \frac{J_{xy}}{\sqrt{J_{xx}J_{yy}}} \tag{1.32}$$

The complex correlation factor j_{xy} is a measure of the correlation between the E_x and E_y, its absolute value is a measure of their degree of coherence, and its phase represents their effective phase difference. j_{xy} has the property based on Schwarz' inequality:

$$| j_{xy} | \leq 1 \tag{1.33}$$

If introducing a retardation ε to E_y with respect to E_x, the intensity of the light vibrations in the direction which makes an angle θ to the positive x-direction can be denoted as $I(\theta, \epsilon)$. Four elements in coherency matrix can be written in terms of six measurements.

$$\begin{aligned} J_{xx} &= I(0^\circ, 0) \\ J_{yy} &= I(90^\circ, 0) \\ J_{xy} &= \frac{1}{2}\{I(45^\circ, 0) - I(135^\circ, 0)\} + \frac{1}{2} i\{I(45^\circ, \frac{\pi}{2}) - I(135^\circ, \frac{\pi}{2})\} \\ J_{yx} &= \frac{1}{2}\{I(45^\circ, 0) - I(135^\circ, 0)\} - \frac{1}{2} i\{I(45^\circ, \frac{\pi}{2}) - I(135^\circ, \frac{\pi}{2})\} \end{aligned} \tag{1.34}$$

For a completely unpolarized light (natural light), the coherency matrix is

$$\frac{1}{2} I_0 \begin{bmatrix} 1 & 0 \\ 0 & 1 \end{bmatrix} \tag{1.35}$$

Where I_0 is the intensity of light and equals to $J_{xx}+J_{yy}$.

For a completely polarized light, the determinant of its coherency matrix is 0.

$$\left| J \right| = J_{xx} J_{yy} - J_{xy} J_{yx} = 0 \tag{1.36}$$

Any quasi-monochromatic light wave can be regarded as the sum of a completely unpolarized and a completely polarized wave; two waves are independent and the representation is unique. Its coherency matrix can be uniquely written as the sum of the coherency matrices of the completely unpolarized wave and completely polarized wave. Degree of polarization P of a light wave is defined as the ratio of the intensity of the polarized portion to the total intensity.

$$P = \frac{I_{pol}}{I_{tot}} = \frac{\sqrt{(J_{xx} + J_{yy})^2 - 4 | J |}}{J_{xx} + J_{yy}} = \sqrt{1 - \frac{4 | J |}{(J_{xx} + J_{yy})^2}} \tag{1.37}$$

The degree of polarization is independent of axes and has a property that

$$0 \leq P \leq 1 \tag{1.38}$$

When P=1, the wave is completely polarized, and as $|J|$=0, E_x and E_y are coherent. When P=0, the wave is completely unpolarized, and

$$\begin{aligned} J_{xx} &= J_{yy} \\ J_{xy} &= J_{yx} = 0 \end{aligned} \tag{1.39}$$

E_x and E_y are incoherent. When 0<P<1, the wave is said to be partially polarized.

The degree of polarization P and the degree of coherence $|j_{xy}|$ have a relation as

$$P \geq |\, j_{xy}\,| \tag{1.40}$$

The equality sign in Eq. 1.40 holds if and only if J_{xx}=J_{yy}, which refers to the condition that the time averaged intensities associated with the x and y directions are equal. So unlike the degree of polarization, the degree of coherence $|j_{xy}|$ depends on the choice of the x and y directions, and there always exists a pair of mutually orthogonal directions that can make J_{xx}=J_{yy}, and under this condition, the degree of coherence has its maximum value which equals the degree of polarization P.

Stokes parameters are another four-parameter representation for a quasi-monochromatic plane wave. Stokes parameters are four quantities written as:

$$\begin{aligned} s_0 &= \left\langle A_1^{\,2} \right\rangle + \left\langle A_2^{\,2} \right\rangle \\ s_1 &= \left\langle A_1^{\,2} \right\rangle - \left\langle A_2^{\,2} \right\rangle \\ s_2 &= 2\left\langle A_1 A_2 \cos\delta \right\rangle \\ s_3 &= 2\left\langle A_1 A_2 \sin\delta \right\rangle \end{aligned} \tag{1.41}$$

Where A_1 and A_2 are the instantaneous amplitudes of the two orthogonal components E_x and E_y, and δ=ϕ_1-ϕ_2 is the phase difference. Stokes parameter and the elements of the coherency matrix are related as

$$\begin{aligned} s_0 &= J_{xx} + J_{yy} \\ s_1 &= J_{xx} - J_{yy} \\ s_2 &= J_{xy} + J_{yx} \\ s_3 &= i(J_{yx} - J_{xy}) \end{aligned} \tag{1.42}$$

Similar to the elements of coherency matrix, the Stokes parameters of any quasi-monochromatic plane wave can be determined from six measurements.

$$\begin{aligned} s_0 &= I(0^\circ,0) + I(90^\circ,0) \\ s_1 &= I(0^\circ,0) - I(90^\circ,0) \\ s_2 &= I(45^\circ,0) - I(135^\circ,0) \\ s_3 &= I(45^\circ,\frac{\pi}{2}) - I(135^\circ,\frac{\pi}{2}) \end{aligned} \tag{1.43}$$

Decompose the wave into mutually independent completely unpolarized and completely polarized portions

$$\begin{aligned} s &= s_u + s_p \\ s_u &= (s_0 - \sqrt{{s_1}^2 + {s_2}^2 + {s_3}^2}, 0, 0, 0) \\ s_p &= (\sqrt{{s_1}^2 + {s_2}^2 + {s_3}^2}, s_1, s_2, s_3) \end{aligned} \tag{1.44}$$

s_u represents the Stokes parameters for completely unpolarized wave, s_p represents completely polarized wave. And the degree of polarization of the wave can be written as

$$P = \frac{I_{pol}}{I_{tol}} = \frac{\sqrt{{s_1}^2 + {s_2}^2 + {s_3}^2}}{s_0} \tag{1.45}$$

For monochromatic wave, Eq. 1.41 can be simplified as

$$\begin{aligned} s_0 &= {A_1}^2 + {A_2}^2 \\ s_1 &= {A_1}^2 - {A_2}^2 \\ s_2 &= 2A_1A_2\cos\delta \\ s_3 &= 2A_1A_2\sin\delta \end{aligned} \tag{1.46}$$

s_1, s_2 and s_3 can be regarded as the Cartesian coordinates of a point on a sphere of radius s_0, the sphere is called Poincaré sphere (Fig. 1.2). Stokes parameters and Poincaré sphere are a useful representation for polarization state of light. Sometime, people also use (I, Q, U, V) to denote Stokes parameters.

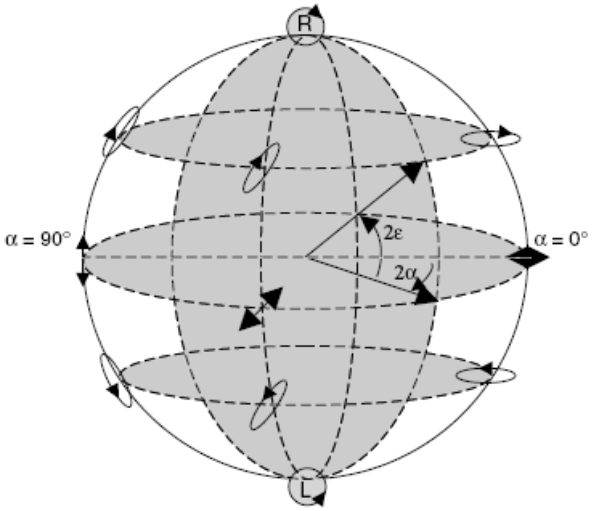

Figure 1.2: Poincaré sphere for polarized light representation.

1.5 TISSUE BIREFRINGENCE

Intrinsic birefringence and form birefringence both contribute to tissue birefringence. Intrinsic birefringence comes from the molecular anisotropy property, and form birefringence arises from a macroscopic anisotropy in the refractive index or dielectric constant. It has been reported (11) that stromal lamellae has intrinsic and form birefringence contribution of 30% and 70% of the total birefringence; bovine stroma has intrinsic and form birefringence with a relative contribution of 25% and 75% respectively.

1.5.1 Intrinsic Birefringence

Intrinsic birefringence of tissue fiber is similar to a positive uniaxial birefringent crystal. A refractive index ellipsoid is commonly used to describe the refractive indices of the uniaxial birefringence crystal (Fig. 1.3).

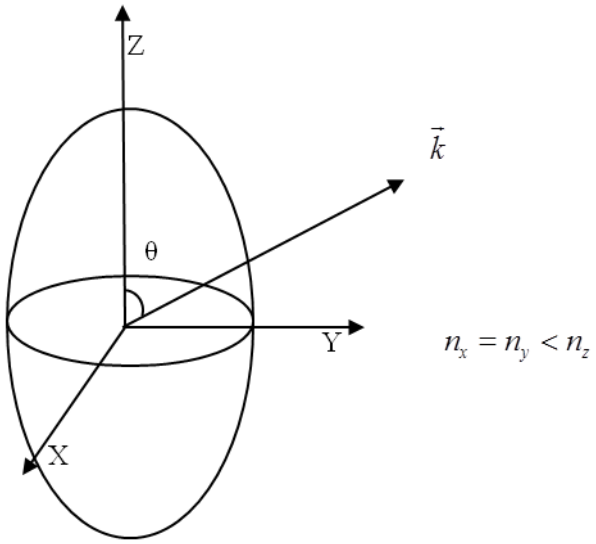

Figure 1.3: Refractive index ellipsoid for a positive uniaxial birefringent crystal.

In the ellipsoid representation above, *x*, y and *z* are chosen to be crystal's principle axes. When light travels along *z* axis of the crystal, no linear birefringence is observed, and this axis is called optical axis of the crystal.

$$\begin{aligned} n_o &= n_x = n_y \\ n_e &= n_z \end{aligned} \tag{1.47}$$

Where n_x, n_y, and n_z are the refractive indices along *x*, *y* and *z* axes, n_o and n_e are the refractive indices for ordinary and extraordinary light when light propagates in the direction orthogonal to optical axis of the crystal. The refractive indices for x and y axes are equal for uniaxial birefringent crystal. The refractive ellipsoid can be written as

$$1 = \frac{x^2}{n_o^{\,2}} + \frac{y^2}{n_o^{\,2}} + \frac{z^2}{n_e^{\,2}} \tag{1.48}$$

If light propagation direction is with an angle of θ with respect to *z* axis, the refractive index n_o' for ordinary light and n_e' for extraordinary light will be

$$n_o' = n_o$$
$$\frac{1}{n_e'^2} = \frac{\cos^2\theta}{n_o^2} + \frac{\sin^2\theta}{n_e^2} \tag{1.49}$$

And the birefringence Δn becomes

$$\Delta n = n_e' - n_o' \tag{1.50}$$

In a more general way, refractive index ellipsoid is written in terms of impermeability tensor.

$$1 = \eta_{11}x^2 + \eta_{22}y^2 + \eta_{33}z^2 + 2\eta_{12}xy + 2\eta_{23}yz + 2\eta_{13}xz \tag{1.51}$$

Where η_{ij} is impermeability tensor

$$\eta_{ij} = (\varepsilon^{-1})_{ij}$$
$$E_i = \frac{1}{\varepsilon_0}\sum_j \eta_{ij} D_j \tag{1.52}$$

In an electro-optic medium,

$$\eta_{ij} = \eta_{ij}^{(0)} + \sum_k r_{ijk}E_k + \sum_{kl} s_{ijkl}E_k E_l + \ldots \tag{1.53}$$

The linear electro-optic effect is the Pockels effect, the quadratic electro-optic effect is Kerr effect. Eq. 1.51 can be written in terms of refractive index

$$1 = (\frac{1}{n^2})_1 x^2 + (\frac{1}{n^2})_2 y^2 + (\frac{1}{n^2})_3 z^2 + (\frac{1}{n^2})_4 2yz + (\frac{1}{n^2})_5 2xz + (\frac{1}{n^2})_6 2xy \tag{1.54}$$

Where contracted notation is used

$$\begin{bmatrix} (\frac{1}{n^2})_1 \\ (\frac{1}{n^2})_2 \\ (\frac{1}{n^2})_3 \\ (\frac{1}{n^2})_4 \\ (\frac{1}{n^2})_5 \\ (\frac{1}{n^2})_6 \end{bmatrix} = \begin{bmatrix} \eta_{11} \\ \eta_{22} \\ \eta_{33} \\ \eta_{23}(\eta_{32}) \\ \eta_{13}(\eta_{31}) \\ \eta_{12}(\eta_{21}) \end{bmatrix} \tag{1.55}$$

According to Eq. 1.53, when Pockels effect exists, the increase in impermeability is written as

$$\begin{bmatrix} \Delta(\frac{1}{n^2})_1 \\ \Delta(\frac{1}{n^2})_2 \\ \Delta(\frac{1}{n^2})_3 \\ \Delta(\frac{1}{n^2})_4 \\ \Delta(\frac{1}{n^2})_5 \\ \Delta(\frac{1}{n^2})_6 \end{bmatrix} = \begin{bmatrix} r_{11} & r_{12} & r_{13} \\ r_{21} & r_{22} & r_{23} \\ r_{31} & r_{32} & r_{33} \\ r_{41} & r_{42} & r_{43} \\ r_{51} & r_{52} & r_{53} \\ r_{61} & r_{62} & r_{63} \end{bmatrix} \begin{bmatrix} E_x \\ E_y \\ E_z \end{bmatrix} \tag{1.56}$$

r_{ij} is electro-optic coefficient. This effect is usually used for a phase modulator, applying voltage on the Pockels cells to change the polarization state of light. For example, a KDP crystal is with electro-optic coefficients

$$r_{ij} = \begin{bmatrix} 0 & 0 & 0 \\ 0 & 0 & 0 \\ 0 & 0 & 0 \\ r_{41} & 0 & 0 \\ 0 & r_{41} & 0 \\ 0 & 0 & r_{63} \end{bmatrix} \tag{1.57}$$

With electrical field applied, the refractive index ellipsoid becomes

$$(\frac{1}{n_0^{\,2}})x^2 + (\frac{1}{n_0^{\,2}})y^2 + (\frac{1}{n_e^{\,2}})z^2 + 2r_{41}E_x yz + 2r_{41}E_y xz + 2r_{63}E_z xy = 1 \tag{1.58}$$

When only E_z is applied, and change coordinate system as

$$\begin{aligned} x &= \frac{x' - y'}{\sqrt{2}} \\ y &= \frac{x' + y'}{\sqrt{2}} \\ z &= z' \end{aligned} \tag{1.59}$$

We have

$$(\frac{1}{n_0^{\,2}} + r_{63}E_z)x'^2 + (\frac{1}{n_0^{\,2}} - r_{63}E_z)y'^2 + (\frac{1}{n_e^{\,2}})z'^2 = 1 \tag{1.60}$$

The refractive indices on *x'y'* plane are

$$\begin{aligned} n_{x'} &= (\frac{1}{n_0^{\,2}} + r_{63}E_z)^{-1/2} \approx n_0 - \frac{1}{2}n_0^{\,3}r_{63}E_z \\ n_{y'} &= (\frac{1}{n_0^{\,2}} - r_{63}E_z)^{-1/2} \approx n_0 + \frac{1}{2}n_0^{\,3}r_{63}E_z \end{aligned} \tag{1.61}$$

So when light propagates a distance of L along crystal's z axis, the crystal introduces a phase retardation between *x'* axis and *y'* axis and is linear to the electrical field applied

$$\delta = 2\pi(n_{x'} - n_{y'})L / \lambda_0 \tag{1.62}$$

1.5.2 Form Birefringence

For a medium consisting of a macroscopic anisotropic linear structure, such as fibrous tissue, relative strong birefringence can be present, which is called form birefringence. Biological tissues such as tendons, muscles, nerve, bone, cartilage and teeth exhibit form birefringence (Δn). In addition to birefringence, forward propagating light may also have a scattering anisotropy resulting in a differential attenuation of amplitude, which is called biattenuance ($\Delta\chi$). When light propagates over a distance L, the phase retardation (δ) and accumulated relative attenuation (e^{-s}) between fast and slow axes can be written as

$$\begin{aligned} \delta &= 2\pi\Delta nL / \lambda_0 \\ s &= 2\pi\Delta\chi L / \lambda_0 \end{aligned} \tag{1.63}$$

Fig. 1.4 shows the origin of form birefringence and biattenuance in fibrous tissues. When incident light is propagating in the tissue, electric field oscillating perpendicular ($E_\perp$) and parallel ($E_\parallel$) to fiber axis are modified anisotropically due to induced surface charges (E_0).

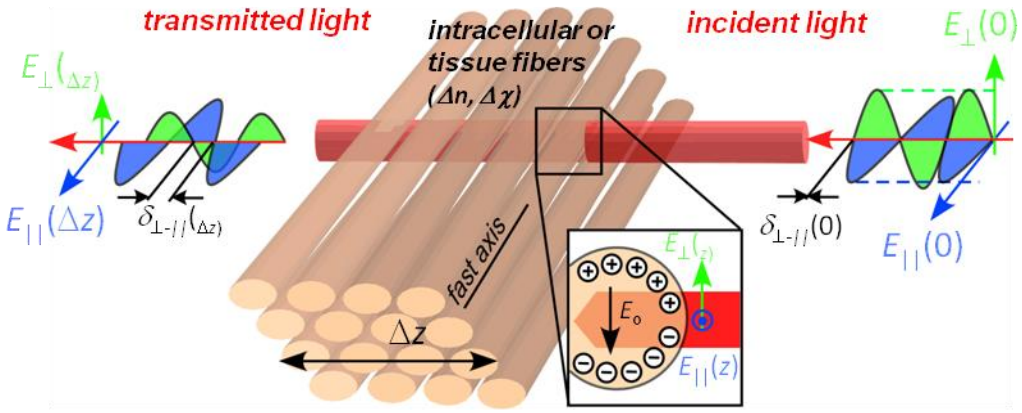

Figure 1.4: Origin of form birefringence and biattenuance.

O. Wiener has developed a general theory for the distribution of the electric field and the dielectric displacement in a heterogeneous system in 1912, and can be used to explain the form birefringence (12-13). The relationship exists between the average field $\vec{E}$ in the heterogeneous dielectric body and the average fields $\overrightarrow{E_i}$ in the various components i of the mixture:

$$V\vec{E} = \sum_i V_i \overrightarrow{E_i}$$
$$V_i \overrightarrow{E_i} = \int_{V_i} \vec{E} dv \qquad (1.64)$$

Where V_i is the volume of component i and the summation is taken over all components enclosed in the volume V of the mixed body. The same relation is applied for the electric displacement $\vec{D}$, where ε_i is the permittivity of the pure compound i.

$$V\vec{D} = \sum_i V_i \varepsilon_i \overrightarrow{E_i} \qquad (1.65)$$

Fibrous tissue structure can be considered as a suspension consisting of parallel circular cylinders with liquid-like translational order, each rod with permittivity ε_2 is surrounded by a shell of solvent with ε_1. Assume the rod particles cannot overlap, the average field

$\overrightarrow{E_2}$ inside one particle is related to the average field $\overrightarrow{E_1}$ in the solvent surrounding the particle by

$$\overrightarrow{E_2} = \frac{\overrightarrow{E_1}}{1+(\frac{\varepsilon_2-\varepsilon_1}{\varepsilon_1})DP_x} \tag{1.66}$$

Parameter DP_x is the depolarizing factor which depends on the orientation of the rods with respect to the external field. For a field parallel to the rod axes, $DP_{\|}$ is zero and the fields inside the rod and in the solvent are equal. If the field is perpendicular to the axes, $DP_{\perp}$ is 1/2, and the field inside the rod is reduced if ε_2 is greater than ε_1, or enhanced if ε_2 is smaller than ε_1. DP_x depends on the shape of particles: planar symmetric particle, for fields oriented in the plane (perpendicular to the normal), $DP_{\perp}$ is 0, and parallel to the normal $DP_{\|}$ is 1; for spherical symmetry, DP_x is isotropic and equal to 1/3.

The general expression for a suspension of parallel cylinders can be derived:

$$\varepsilon_x = \varepsilon_1 + \frac{f(\varepsilon_2-\varepsilon_1)}{1+(1-f)(\frac{\varepsilon_2-\varepsilon_1}{\varepsilon_1})DP_x} \tag{1.67}$$

Where f is the volume fraction of the particles in the suspension.

According to Eq. 1.11, for light incident normal to rod axes, the birefringence can be written as

$$\begin{aligned}\Delta n &= n_{\|} - n_{\perp} = \sqrt{\varepsilon_{\|}} - \sqrt{\varepsilon_{\perp}} \\ &= \sqrt{\frac{\varepsilon_1 + \dfrac{f(\varepsilon_2-\varepsilon_1)}{1+(1-f)(\dfrac{\varepsilon_2-\varepsilon_1}{\varepsilon_1})DP_{\|}}}{\varepsilon_0}} - \sqrt{\frac{\varepsilon_1 + \dfrac{f(\varepsilon_2-\varepsilon_1)}{1+(1-f)(\dfrac{\varepsilon_2-\varepsilon_1}{\varepsilon_1})DP_{\perp}}}{\varepsilon_0}}\end{aligned} \tag{1.68}$$

The form birefringence is essentially introduced by the anisotropy of depolarization factor DP_x. When f is close to 1, the anisotropy effect is reduced, which corresponds to the fact that the field becomes more isotropic with increasing

concentration. When intrinsic birefringence exists in the particle, ε_2 has to be replaced by the permittivity on the corresponding axis.

1.6 OCT FOR OPHTHALMOLOGY

OCT has been applied in ophthalmology, cardiology, dermatology, and neurology as a non-invasive, high resolution and high speed three-dimensional imaging technique. Nowadays, OCT is a standard of care in ophthalmology. It enables visualization of retinal pathology at resolutions not possible with other non-invasive imaging techniques. Moreover, it also shows promise for diagnosis and monitoring of diseases such as glaucoma, age-related macular degeneration.

So far, OCT has used light sources with center wavelengths at 830, 1060, 1310 and 1550 nm. Water absorption is a concern for retinal imaging. As shown in Fig. 1.5, due to water absorption in the vitreous fluid anterior to the retina, 1310 nm and 1550 nm sources are unsuitable for retina imaging. Most common ophthalmologic sources are centered at 830 nm where water absorption is minimal. And more recently, source with center wavelength at 1060 nm has been applied for retina imaging as maximum permissible exposure (MPE) at this wavelength is much higher than at 830 nm and the tissue scattering strength is lower.

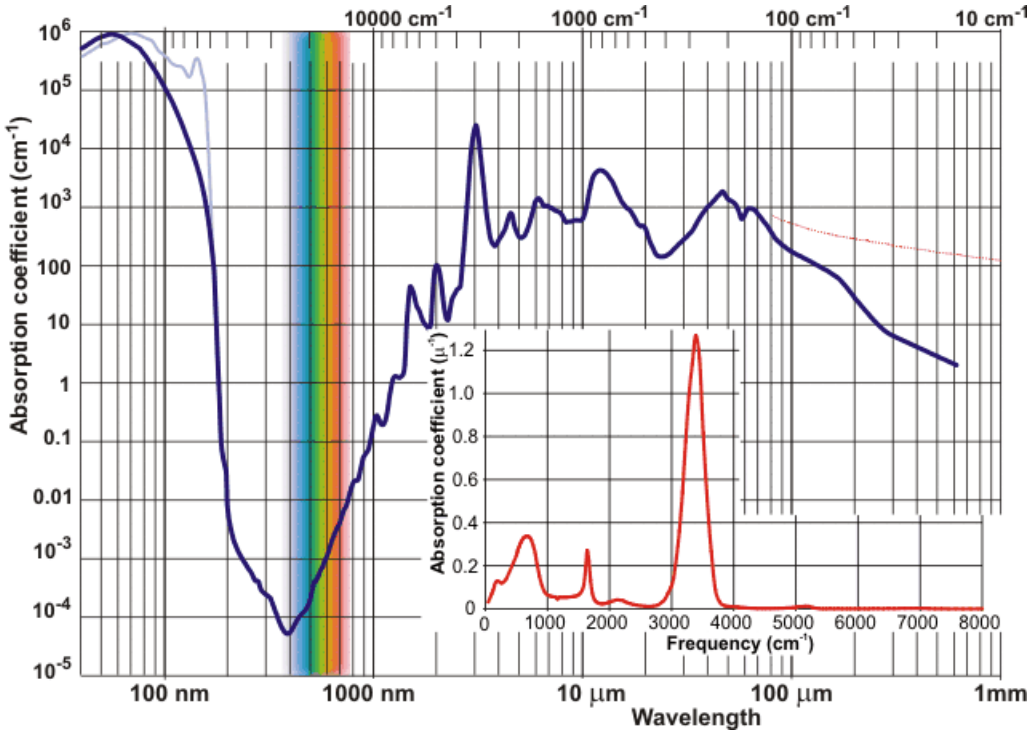

Figure 1.5: Water absorption spectrum.

To broaden the application of OCT in ophthalmology, various functional OCT imaging techniques have been developed. In this dissertation, polarization-sensitive OCT (PS-OCT) and the dual-wavelength photothermal OCT (DWP-OCT) are two functional imaging techniques for retinal imaging and diagnosis.

Retinal nerve fiber layer (RNFL) is known as a weakly birefringent layer due to oriented cylindrical structure of the ganglion cell axons (14), clinical studies have found that changes in RNFL birefringence may correlate with damage in glaucoma (15-17). In addition to traditional intensity OCT, PS-OCT is able to provide the birefringence measurement of the RNFL, which can be used as an indication of structural change in the cytoskeleton of retinal ganglion cells (RGC), and make early detection of disease such as glaucoma possible.

Non-invasive quantitative evaluation of microvasculature hemoglobin oxygen saturation (SO_2) in tissue is important for understanding and monitoring progression of inflammatory and ischemic disease such as cancer, stroke and glaucoma (18-19). DWP-OCT is designed for combining microvasculature blood SO_2 measurement function with OCT imaging. In these studies, a DWP-OCT is constructed for retina microvasculature blood SO_2 measurement and demonstrates its feasibility.

Chapter 2: Polarization-Sensitive Optical Coherence Tomography for Retinal Nerve Fiber Layer Birefringence Measurement

2.1 Introduction of PS-OCT Study

Polarization-sensitive (PS) OCT is a functional extension of OCT. In addition to intensity imaging; PS-OCT can provide a measure of a biological sample's birefringence properties (i.e., birefringence, phase retardation and optical axis orientation). PS-OCT was first implemented in a bulk optics system (20-21), since polarization state of light can be easily controlled and preserved in free space. Later fiber-based PSOCT systems were developed (22-24). Compared with PS-OCT systems using bulk optics, fiber-based systems provide convenience in alignment but at the cost of polarization mode dispersion, additional processing of detected polarization data and more complex hardware. Both polarization-maintaining fiber (PMF) and standard single mode fiber (SMF) have been implemented for PS-OCT system construction (25-35). PMF based PS-OCT systems take advantage of PMF's property that light propagation in two orthogonal linear polarization states can be maintained. Due to different propagation velocity of the light in two orthogonal states, however, length mismatch of sample and reference arms paths is normally compensated by hardware or software (25-27). Due to the fact that single mode fiber provides a unitary transformation of the polarization state of transmitted light, the polarization signal acquired by a PS-OCT system utilizing SMF has to be reinterpreted, and different methodologies have been proposed (28-35).

PS-OCT has been applied in ophthalmology to investigate birefringence of ocular structures including the cornea, crystalline lens and the retinal nerve fiber layer (RNFL). Since RNFL is known to be birefringent with microtubules within retinal ganglion cells

(RGCs) contributing significantly to the form birefringence (14), measurement of RNFL birefringence can be used to monitor structural changes in the cytoskeleton of retinal ganglion cells (RGC).

In polarization optics, degree of polarization (DOP) is usually defined as the ratio of intensity of completely polarized light to the total intensity of light. The DOP is unity for purely polarized light, smaller than unity for partially polarized light, and is zero for unpolarized light. Recently the degree of polarization uniformity (DOPU) (36) was introduced and applied by researchers to examine the depth-resolved uniformity of backscattered light's polarization state represented by Stokes parameters on Poincaré sphere for multiple A-scans within a small sample region. Factors that may contribute to the degradation of DOP with increasing depth in biological tissue include: multiple forward scattering events in which light travels through different paths but is singly backscattered; polarization state changes when light is forward or backward scattered by irregularly shaped particles; and speckle noise and signal-to-noise ratio (SNR) degradation with increasing depth (37).

In this study a single-mode-fiber based swept-source polarization-sensitive OCT clinical system was constructed and utilized to investigate the degradation in the degree of polarization (DOP) of light backscattered from human RNFL with increasing depth. I observe the reduction of the DOP with depth in human RNFL and differences in degradation in DOP in superior, temporal, inferior and nasal quadrants was measured.

2.2 CLINICAL PS-OCT SYSTEM

The clinical polarization-sensitive OCT (Fig. 2.1) system utilized a swept-source laser (HSL-1000 by Santec Corp., Komaki, Aichi, Japan) with a sweep rate of 28 kHz,

1064 nm center wavelength and a spectral scan range of 80 nm, providing an axial resolution of 12 μm in tissue. Fig. 2.2 is a digital picture of the clinical swept-source polarization-sensitive OCT system.

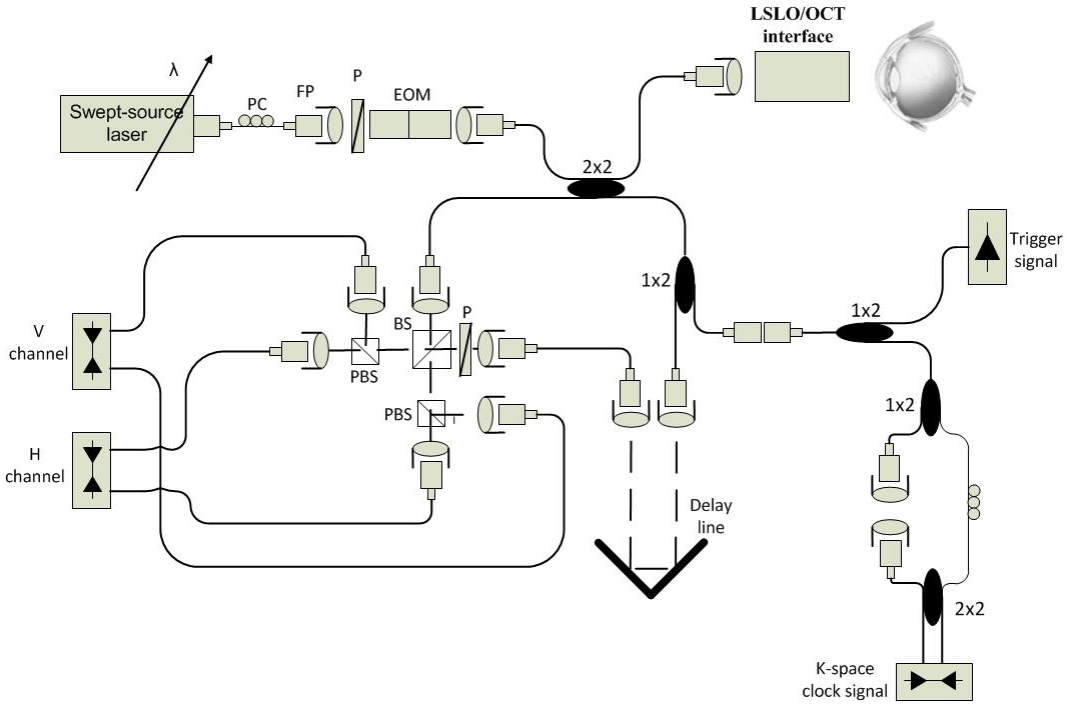

Figure 2.1: Clinical swept-source polarization-sensitive OCT system. PC: polarization controller; FP: fiber port; P: polarizer; EOM: broadband electro-optic modulator; BS: non-polarization beam splitter; PBS: polarization beam splitter.

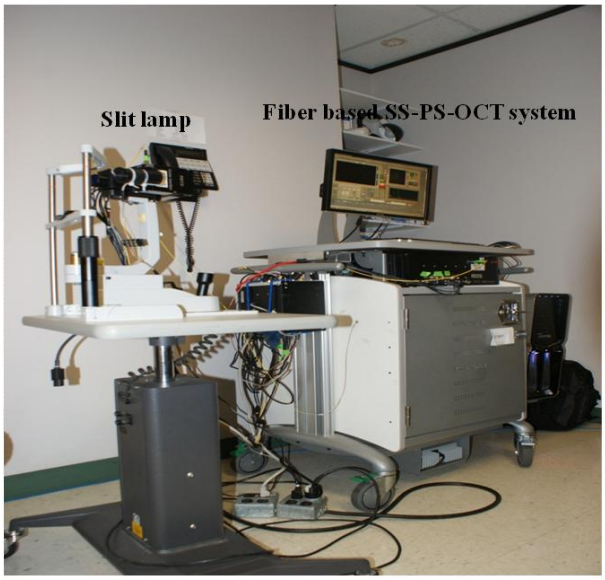

Figure 2.2: SS-PS-OCT clinical system. Slitlamp is on the left. Fiber-based swept-source PS-OCT system on the right.

A polarization controller consisting of a linear polarizer and an electro-optic phase modulator is utilized to provide three incident polarization states onto sample. The electro-optic phase modulator is composed of two lithium niobate ($LiNbO_3$) crystals with fast and slow axes oriented at 45° to the linear polarizer. The two $LiNbO_3$ crystals are equal length and fast axis of one is coaligned with the slow axis of the other to balance intrinsic birefringence and remove polarization mode dispersion. A high voltage amplifier controls the phase retardation in the two crystals. The voltage applied to the phase modulator is adjusted to provide three polarization states with Stokes vectors (Q, U, V) in the right-handed laboratory frame being (1, 0, 0), (-sin30°, 0, sin60°) and (-sin30°, 0, -sin60°) (33). In the laboratory frame, the horizontal axis is along x, vertical (along gravity) is along y and the light propagates along the z direction.

The working principle of polarization controller is explained below. The light after polarizer (E_{in}) has Jones vector as

$$E_{in} = \begin{pmatrix} 1 \\ 0 \end{pmatrix} \tag{2.1}$$

As $LiNbO_3$ phase modulator has fast and slow axes at 45° with respect to the orientation of linear polarization, a 45° rotation matrix is applied, and I assume the phase difference introduced by phase modulator is ϕ, the output electric field E_{out} becomes

$$\begin{aligned} E_{out} &= \begin{pmatrix} \cos 45° & \sin 45° \\ -\sin 45° & \cos 45° \end{pmatrix} \begin{pmatrix} e^{-\frac{1}{2}j\phi} & 0 \\ 0 & e^{\frac{1}{2}j\phi} \end{pmatrix} \begin{pmatrix} \cos 45° & -\sin 45° \\ \sin 45° & \cos 45° \end{pmatrix} E_{in} \\ &= \begin{bmatrix} \cos\frac{\phi}{2} \\ j\sin\frac{\phi}{2} \end{bmatrix} \end{aligned} \tag{2.2}$$

According to the Pockels effect, the phase difference introduced by crystal is proportional to the voltage applied on the crystal. The Stokes vector for E_{out} is as written in Eq. 2.3. By tuning the voltage applied on crystal, any polarization state on QV plane of the Poincaré sphere can be achieved.

$$(I, Q, U, V) = (1, \cos\phi, 0, \sin\phi) \tag{2.3}$$

A 30/70 fiber coupler splits the source light into sample and reference arms. In the sample arm, a patient interface delivers OCT light onto patient's cornea together with a line scanning laser ophthalmoscope (LSLO) with an average OCT power of 0.86 mW incident on the cornea. Light in the reference arm has two paths; one is connected to a balanced detection module to interfere with sample light; the other splits into system trigger and an electronic circuit for a resampling clock. A Mach-Zehnder interferometer (MZI) is used to generate a resampling clock signal and is connected to an external circuit board to quadruple the clock frequency (38).

Light reflected from the sample interferes with reference light in a bulk optics balanced detection module (Fig. 2.3). Reference light goes through a polarizer oriented at 45° before interference to ensure equal intensity and zero phase delay in horizontal and vertical polarization states. A non-polarization crystal beam splitter is used for balanced detection, and two polarization beam splitters separate interference signals into vertical and horizontal channels. The bulk optics balanced detection module used for polarization detection eliminates the unbalanced polarization transformations between the two detection arms.

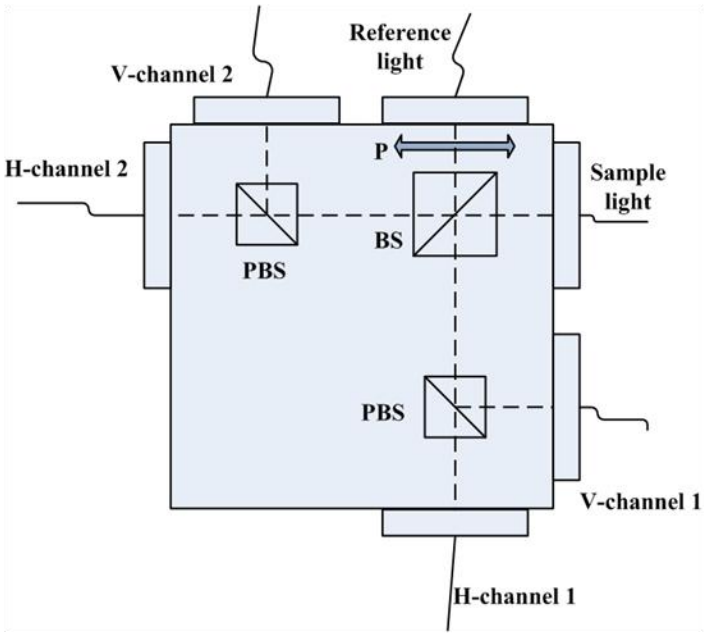

(a)

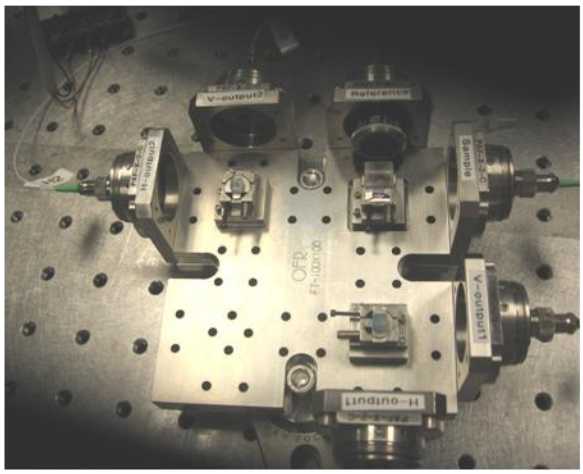

(b)

Figure 2.3: Polarization-sensitive balanced detection module. (a) schematic; (b) digital picture.

Assume I_{sv} and I_{sh} represent the vertical and horizontal components of the intensity of light reflected from sample, I_{rv} and I_{rh} are vertical and horizontal components

of the intensity of reference light, n_1 and n_2 are refractive indices of sample in vertical and horizontal direction, and the depth of imaging position is Δz. The interference signal intensity for each channel (I_{v1}, I_{v2}, I_{h1} and I_{h2}) can be written as:

$$\begin{aligned} I_{v1}(k) &= I_{sv}(k)/2 + I_{rv}(k)/2 + \sqrt{I_{sv}(k)I_{rv}(k)}\cos(n_1 k\Delta z) \\ I_{v2}(k) &= I_{sv}(k)/2 + I_{rv}(k)/2 - \sqrt{I_{sv}(k)I_{rv}(k)}\cos(n_1 k\Delta z) \\ I_{h1}(k) &= I_{sh}(k)/2 + I_{rh}(k)/2 + \sqrt{I_{sh}(k)I_{rh}(k)}\cos(n_2 k\Delta z) \\ I_{h2}(k) &= I_{sh}(k)/2 + I_{rh}(k)/2 - \sqrt{I_{sh}(k)I_{rh}(k)}\cos(n_2 k\Delta z) \end{aligned} \tag{2.4}$$

The π phase shift between I_{v1} and I_{v2}, I_{h1} and I_{h2} in the interference fringe signal terms is introduced by the beam splitter. With the balanced photodetector, the detected signal for V-channel (I_v) and H-channel (I_h) is written as

$$\begin{aligned} I_v(k) &= 2\sqrt{I_{sv}(k)I_{rv}(k)}\cos(n_1 k\Delta z) \\ I_h(k) &= 2\sqrt{I_{sh}(k)I_{rh}(k)}\cos(n_2 k\Delta z) \end{aligned} \tag{2.5}$$

With this polarization-sensitive bulk-optics balanced detection module, DC terms are cancelled while fringe signal terms are maintained (Fig. 2.4). Moreover, with the bulk optics setup for two detection arms, polarization states of interfered light after splitting by beam splitter are preserved to ensure the equality for balanced detection. According to the fact that signals sum by amplitude, noise sums by intensity, a 3 dB SNR increase is expected from this detection module.

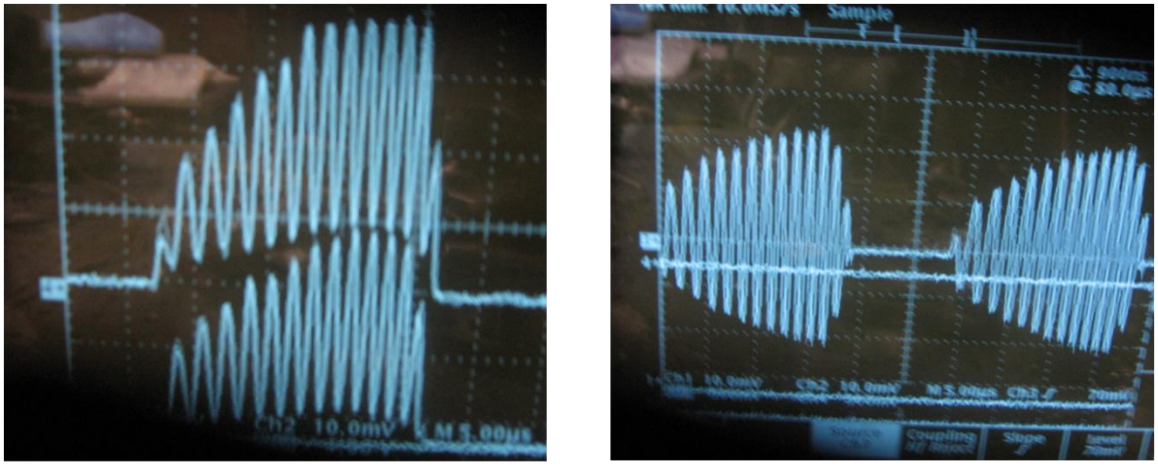

(a) (b)

Figure 2.4: (a) Interference signals in each detection arm, a π phase shift is introduced between two arms. (b) Signal detected by balanced photodetector, DC noise is balanced, fringe is maintained.

2.3 BIREFRINGENCE MEASUREMENT

2.3.1 Levenberg-Marquardt non-linear fitting algorithm on Poincaré sphere

Assume the polarization state of light after polarization controller is E_{in}, the transformation introduced by optical fiber and other optical components between polarization controller and sample surface is J_{in}, the transformation of sample is J_s (double-pass), the transformation introduced by optical fiber and optical components between sample surface and detector is J_{out}. The electric field of light reflected from sample surface E_s and imaging position inside the sample E_z can be written as:

$$\begin{aligned} E_s &= J_{out} J_{in} E_{in} \\ E_z &= J_{out} J_s J_{in} E_{in} \end{aligned} \tag{2.6}$$

From Eq. 2.6 we have

$$\begin{aligned} E_{in} &= J_{in}^{-1} J_{out}^{-1} E_s \\ E_z &= J_{out} J_s J_{out}^{-1} E_s \end{aligned} \tag{2.7}$$

The transformation introduced by the sample can be written in terms of phase retardation and optical axes rotation.

$$J_s = J_A J_R J_A^{-1} \tag{2.8}$$

Combining Eqs. 2.7 and 2.8, E_z is written as

$$E_z = J_{out} J_A J_R J_A^{-1} J_{out}^{-1} E_s \tag{2.9}$$

When the transformation matrix introduced by optical fiber and optical components can be assumed to be as a unitary matrix (light amplitude is preserved), Eq. 2.9 indicates that the composite effect of the optical fiber, optical components and sample axes orientation in the PS-OCT system only produce a coordinate system rotation on Poincaré sphere (28-29).

The coordinate system rotation can be represented in two steps: first rotate the QU plane around the V axis, and then rotate the new QV plane around the U axis. The rotation that makes Q axis aligned with optical axis of sample in laboratory frame is the rotation that describes the transformation from sample frame to laboratory frame. If assume the normalized Stokes vector for optical axis of the sample (new Q axis) is

$$(\sin\theta_0 \cos\varphi_0, \sin\theta_0 \sin\varphi_0, \cos\theta_0)$$

Then the new U axis becomes

$$(-\sin\varphi_0, \cos\varphi_0, 0)$$

And the new V axis becomes

$$(-\cos\theta_0 \cos\varphi_0, -\cos\theta_0 \sin\varphi_0, \sin\theta_0)$$

So the Euler rotation matrix can be constructed

$$\begin{pmatrix} \sin\theta_0 \cos\varphi_0 & -\sin\varphi_0 & -\cos\theta_0 \cos\varphi_0 \\ \sin\theta_0 \sin\varphi_0 & \cos\varphi_0 & -\cos\theta_0 \sin\varphi_0 \\ \cos\theta_0 & 0 & \sin\theta_0 \end{pmatrix} \tag{2.10}$$

Applying Euler rotation matrix, we are able to construct the model function describing the trajectory of depth-resolved Stokes vectors of light propagating in the sample on Poincaré sphere. In absence of diattenuation (39), when light propagates through a uniform birefringent layer, the trajectory of normalized Stokes vectors of backscattered light rotates about an eigen-axis on Poincaré sphere. Effect of polarization transformations in the single mode fiber cause an rotation of the eigen-axis away from the equator on the Poincaré sphere (28, 39). If the single mode fiber remains stable while switching incident polarization states, equivalent transformations of three incident polarization states is produced giving three arcs on Poincaré sphere with a common rotation axis.

From the PS-OCT measurement, interference fringe signals and relative phase retardation of light detected in V-channel and H-channel are used to obtain Stokes vectors of light returning from each RNFL depth. In each cluster of A-scans, 100 A-scans' Stokes vectors are averaged and normalized: ($Q_{meas,i,s}$, $U_{meas,i,s}$, $V_{meas,i,s}$) are the Stokes vector of averaged and normalized Stokes vectors at depth i with incident polarization state s; depth-resolved Stokes vector trajectory are traced, and a three-state Levenberg-Marquardt nonlinear fitting algorithm is applied to determine optical-axis orientation, phase retardation, and birefringence.

Levenberg-Marquardt nonlinear fitting algorithm is a method that provides a numerical solution to the problem of minimizing a function. When biattenuance is negligible, we assume Stokes vector of sample optical axis has azimuthal and polar angle (φ_0, θ_0), the azimuthal and polar angles for the Stokes vectors of three incident states are (φ_1, θ_1), (φ_2, θ_2), (φ_3, θ_3) and phase retardation per unit depth is δ, total 9 parameters. The model function describing the trajectory of arcs can be constructed based on Euler rotation matrix and these nine parameters.

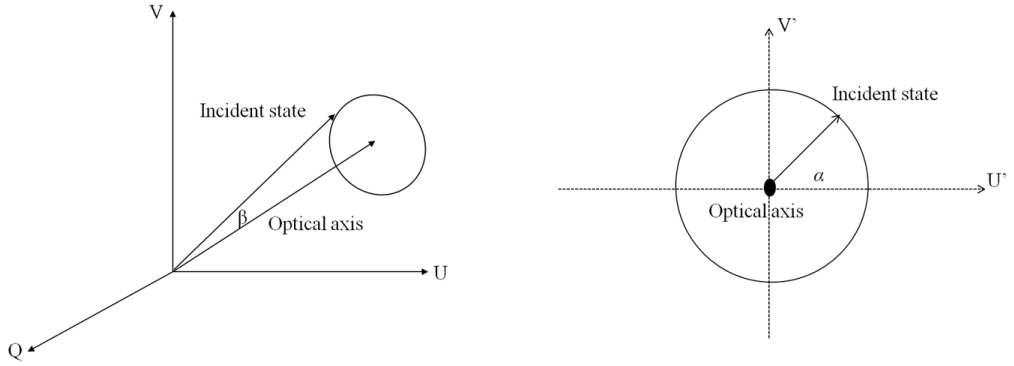

Figure 2.5: (a) Trajectory of normalized Stokes vectors of backscattered light rotates about optical axis, β is cone angle. (b) Rotation of the trajectory on the plane normal to optical axis, α is the angle between the projection of Stokes vector of incident state on *U'V'* plane and *U'* axis.

In Fig. 2.5a, the cone angle β is the angle between optical axis and incident state. Consider incident state 1, assume $\overrightarrow{OA}$ and $\overrightarrow{OI_1}$ refer to the Stokes vectors of optical axis and incident polarization state1.

$$\cos\beta = \frac{\overrightarrow{OA} \bullet \overrightarrow{OI_1}}{\left|\overrightarrow{OA}\right|\left|\overrightarrow{OI_1}\right|} = \sin\theta_o \cos\varphi_0 \sin\theta_1 \cos\varphi_1 + \sin\theta_0 \sin\varphi_0 \sin\theta_1 \sin\varphi_1 + \cos\theta_0 \cos\theta_1 \tag{2.11}$$

$$\sin\beta = \sqrt{1-\cos^2\beta}$$

Fig 2.5b shows the rotation of the trajectory on the plane normal to optical axis, and as discussed before, this rotation can also be considered as a rotation in a coordinate system where *Q'* axis is the rotation axis, *U'* and *V'* axes are (-sinφ_0, cosφ_0, 0) and (-cos$\theta_0$cosφ_0, -cos$\theta_0$sinφ_0, sinθ_0) respectively. The angle α is the angle between the projection of $\overrightarrow{OI_1}$ on *U'V'* plane and *U'* axis. α is derived based on the projections of

$\overrightarrow{OI_1}$ on U' and V' axes, where operation atan2 is used and represents inverse tangent in four quadrants.

$$\begin{aligned}\alpha &= \text{a tan } 2\frac{\overrightarrow{OI_{1V'}}}{\overrightarrow{OI_{1U'}}} \\ &= \frac{-\sin\theta_1\cos\varphi_1\cos\theta_0\cos\varphi_0 - \sin\theta_1\sin\varphi_1\cos\theta_0\sin\varphi_0 + \cos\theta_1\sin\theta_0}{-\sin\theta_1\cos\varphi_1\sin\varphi_0 + \sin\theta_1\sin\varphi_1\cos\varphi_0}\end{aligned} \tag{2.12}$$

In the $Q'U'V'$ coordinate system, the Stokes vector for light backscattered from depth i is written as

$$\begin{aligned}Q_i' &= \cos\beta \\ U_i' &= \sin\beta\cos(\alpha + 2(i-1)\delta) \\ V_i' &= \sin\beta\sin(\alpha + 2(i-1)\delta)\end{aligned} \tag{2.13}$$

Convert Stokes vectors from $Q'U'V'$ coordinate system to QUV coordinate system by simply multiplied by Euler rotation matrix derived before.

$$\begin{pmatrix} Q_i \\ U_i \\ V_i \end{pmatrix} = \begin{pmatrix} \sin\theta_0\cos\varphi_0 & -\sin\varphi_0 & -\cos\theta_0\cos\varphi_0 \\ \sin\theta_0\sin\varphi_0 & \cos\varphi_0 & -\cos\theta_0\sin\varphi_0 \\ \cos\theta_0 & 0 & \sin\theta_0 \end{pmatrix} \begin{pmatrix} Q_i' \\ U_i' \\ V_i' \end{pmatrix} \tag{2.14}$$

Model function for depth-resolved Stokes vectors of backscattered light with different incident states can be derived. Each point on the model function represents one fitted value ($Q_{model,i,s}$, $U_{model,i,s}$, $V_{model,i,s}$) at depth i for incident state s. Levenberg-Marquardt nonlinear fitting algorithm are applied to minimize the difference between fitted values and measurement values to estimate the 9 parameters (Eq. 2.15).

$$f(\varphi_0,\theta_0,\delta,\varphi_1,\theta_1,\varphi_2,\theta_2,\varphi_3,\theta_3) = \sum_s\sum_i \begin{bmatrix} abs(Q_{meas,i,s} - Q_{model,i,s}) \\ +abs(U_{meas,i,s} - U_{model,i,s}) \\ +abs(V_{meas,i,s} - V_{model,i,s}) \end{bmatrix} \tag{2.15}$$

A typical fit of three recorded arcs on the Poincaré sphere (Fig. 2.6) correspond to three incident polarization states in which all three arcs rotate around a common axis; the rotation angle represents the double pass phase retardation of light propagating through and backscattered from the RNFL.

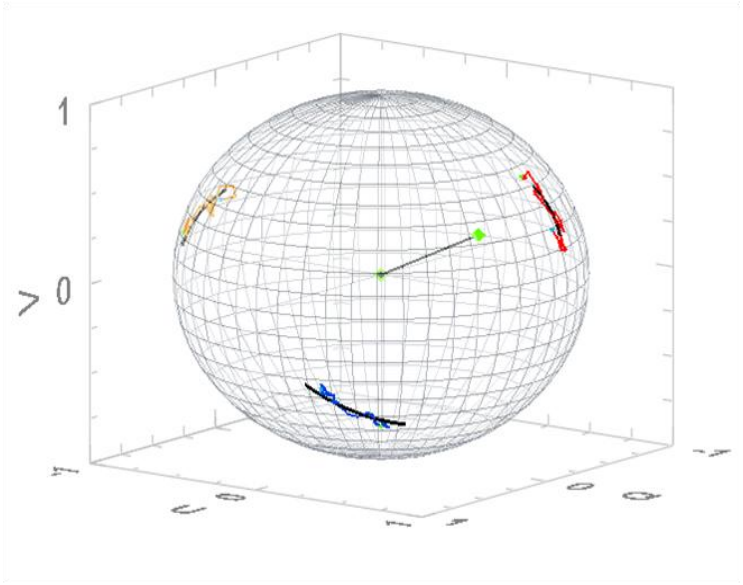

Figure 2.6: Depth-resolved Stokes vector on Poincaré sphere for one cluster corresponding to three incident polarization states. Each arc represents the fitted trajectory of one incident polarization state.

2.3.2 Clinical PS-OCT study

PS-OCT measurements were recorded from patients enrolled in a clinical study at the Eye Institute of Austin (EIA) and the Duke Eye Center. Patients were carefully selected, inclusion criteria for the study included: age between 40 and 80, visual acuity score of 20/40 or better, spherical refraction with ±5 diopters and cylinder refraction with ±3 diopters. Patient measurement protocol was: 1. PS-OCT measurement, 2. GDx nerve fiber analyzer, 3. Optovue OCT test, 4. Visual field test and eye exam (40).

80 subjects were enrolled in this study, including normal subjects, glaucoma suspects, and glaucoma patients (Tab. 2.1). In addition to SS-PS-OCT data, GDx and Optovue OCT data were also recorded.

Study Site	Glaucoma patient	Glaucoma suspect	Normal control
Eye Institute of Austin	9	19	15
Duke Eye Center	16	2	19

Table 2.1: Patients enrollment in clinical study.

A typical SS-PS-OCT data set obtained from one subject includes ten intensity cluster ring scan images (Fig. 2.7), cluster ring scan thickness map, cumulative phase retardation map and birefringence map with blood vessels superposed (Fig. 2.8).

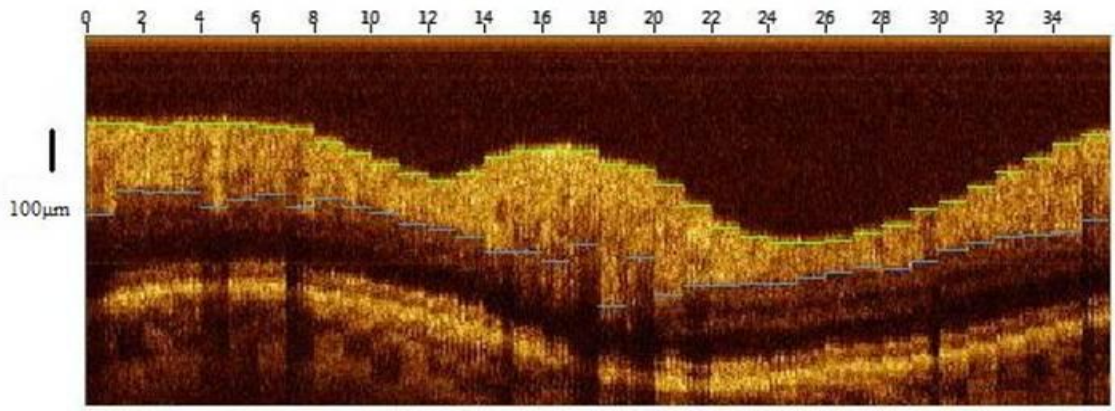

Figure 2.7: Retina cluster ring scan intensity image with segmentation.

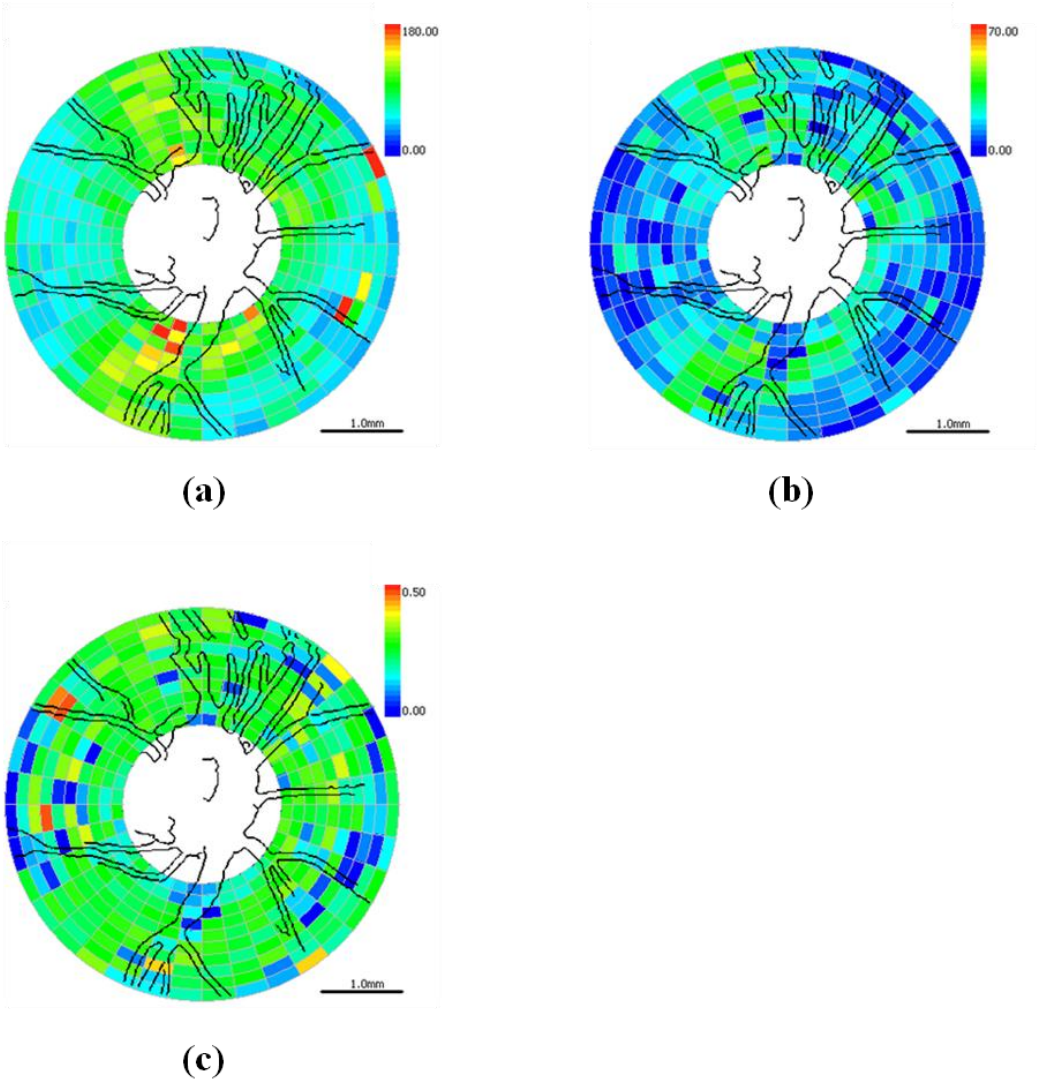

Figure 2.8: (a) Cluster thickness map (μm); (b) Phase retardation map (degree); (c) Birefringence map (degree/μm).

2.4 Degradation of Degree of Polarization

2.4.1 Polarization Processing

To investigate the degradation of degree of polarization in human RFNL, processing method as shown in Fig. 2.9 is developed. Starting from Box 1, Stokes vectors

(Box 2.1) and Jones vectors (Box 2.2) are constructed for depth-resolved A-scan signals recorded in the laboratory frame. For each incident state, depth-resolved Stokes vectors for 100 A-scans are averaged and normalized to reduce polarimetric noise by a factor of approximately 10 (Box 3); and ideally these three arcs rotate about a common axis corresponding to RNFL's optical axis. The trajectories on the Poincaré sphere corresponding to the three incident states are constructed based on averaged and normalized Stokes vectors. The Stokes vector of the optical axis is determined by using a Levenberg-Marquardt nonlinear least-square fitting algorithm to fit a single vector originating from the center of Poincaré sphere to be the rotation axis of all three arcs (Box 4). Note that whether this axis represents fast or slow axis can be determined by the direction of rotation of the trajectory with increasing RNFL depth. Fast and slow axes are orthogonal to each other in the Jones vector formalism; on the Poincaré sphere, their Stokes vector representations are on polar-opposite sides of the Poincaré sphere.

In the Jones vector calculus, (E_x, E_y) represents a polarization state where the two components E_x and E_y represent analytic signal for the complex electric field along the x- and y-axis in the laboratory frame. In a linearly form-birefringent fibrous tissue, fast and slow axes correspond to directions parallel and perpendicular to the tissue fiber orientation (12). We adopt a Jones vector formulation by assuming a coordinate system parallel and perpendicular to the fiber orientation to analyze propagation of amplitude and phase of backscattered light in the native coordinate system of the fibrous tissue sample frame (SF). Depth-resolved polarization data are transformed from the laboratory frame (LF) into SF by projecting their Jones vectors onto fast and slow axes of the fibrous tissue sample (Box 5.1 and 5.2). In Fig. 2.9, subscript x and y represent two orthogonal axes in the laboratory frame (LF); subscript x' and y' represent two

orthogonal axes in the sample frame (SF); subscript *f* and *s* represent fast and slow axes; and subscript *i* refers to a single A-scan

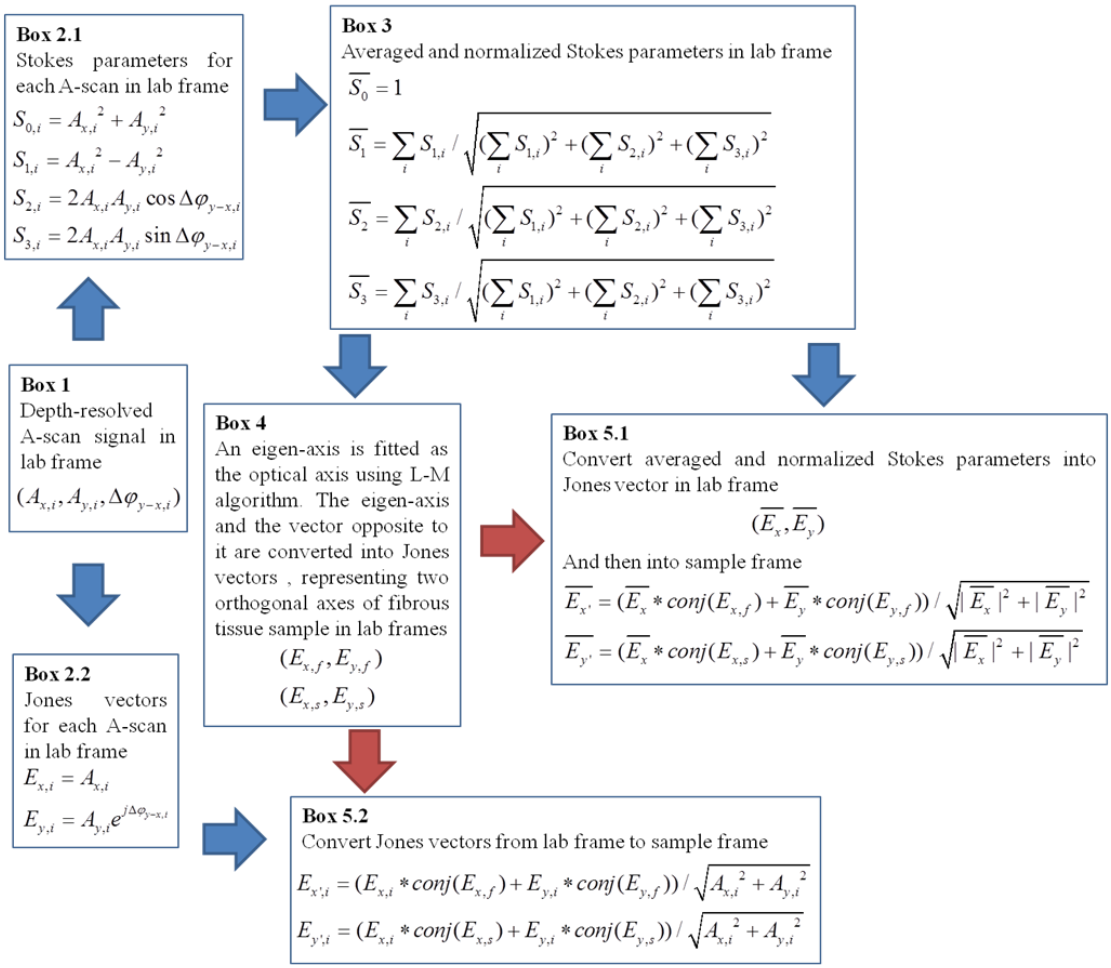

Figure 2.9: Flow chart diagram of processing to transform depth-resolved polarization data from the laboratory frame (LF) into the fibrous tissue sample frame (SF). Blue arrows indicate data transformation; red arrows indicate the fast and slow axes determined in Box 4 are applied in Box 5.1 and 5.2 for conversion from LF to SF.

After obtaining depth-resolved Jones vectors of backscattered light in the SF, the phase difference $\overline{\Delta\varphi_{y'-x'}}$ between $\overline{E_{x'}}$ and $\overline{E_{y'}}$ is the phase retardation introduced by the sample birefringence. Since the RNFL is assumed to be a linear birefringent layer, a

linear fit is applied to phase retardation data $\overline{\Delta\varphi}_{y'-x'}$ with respect to sample depth; phase retardation values on the fitted curves are taken as the theoretical phase retardation $\Delta\varphi_{y'-x',t}$ at that depth, while the slope of this linear fit indicates phase retardation per unit depth of the sample or birefringence. Each cluster is interrogated by three incident polarization states, under ideal condition, three states' phase retardation per unit depth should be identical, as a linear fit is applied separately for each incident state, phase retardation per unit depth for different incident states may vary from each other slightly, which can be caused by measurement error and polarimetric noise.

To investigate degradation in DOP with increasing RNFL depth, each cluster's 100 A-scans are also converted from the laboratory frame (LF) to the sample frame (SF) ($E_{x',i}$, $E_{y',i}$) based on the same optical axes, and the phase retardation $\Delta\varphi_{y'-x',i}$ is computed vs. depth for each A-scan.

Coherency matrix (see Chapter 1) is utilized, for convenience, we write again here (Eq. 2.16). In polarization optics, the coherency matrix J is defined as (10)

$$J = \begin{bmatrix} J_{xx} & J_{xy} \\ J_{yx} & J_{yy} \end{bmatrix} = \begin{bmatrix} < E_x E_x^* > & < E_x E_y^* > \\ < E_y E_x^* > & < E_y E_y^* > \end{bmatrix} \tag{2.16}$$

Where E_x, E_y are the complex electric fields along two orthogonal axes, the bracket represents time average and the * superscript refers to complex conjugate. J_{xx} and J_{yy} are the intensity of electric field along the two axes; J_{xy} and J_{yx} are complex conjugate to each other and the phase is the effective phase ($\arg(J_{xy})$) retardation between the two axes. The degree of polarization P is written as in Eq. 2.17

$$P = \sqrt{1 - \frac{4|J|}{(J_{xx} + J_{yy})^2}} = \sqrt{1 - \frac{4(J_{xx}J_{yy} - J_{xy}J_{yx})}{(J_{xx} + J_{yy})^2}} \tag{2.17}$$

According to Eqs. 2.16 and 2.17, a more randomized phase difference between E_x and E_y corresponds to an average value of $E_xE_y^*$ or $E_yE_x^*$ (J_{xy} or J_{yx}) closer to zero,

resulting in a smaller degree of polarization. Moreover, normalized J_{xy} is written as j_{xy} in Eq. 2.18, the absolute value | j_{xy} | represents the degree of coherence between light oscillating along the two axes. Unlike degree of polarization, the degree of coherence depends on coordinate system, and it shows the correlation between electric fields along two orthogonal axes. Randomization of phase difference between the two axes also corresponds to a reduced degree of coherence.

$$j_{xy} = \frac{J_{xy}}{\sqrt{J_{xx}}\sqrt{J_{yy}}} \tag{2.18}$$

We investigate depth-resolved changes in the degree of polarization (DOP) and degree of coherence of backscattered light in the sample frame corresponding to directions parallel and perpendicular to the nerve fibers. Variation of phase retardations of 100 A-scans from fitted values (var($\Delta\varphi$)) is calculated at each depth position (Eq. 2.19). The statistics we analyze for one cluster's polarization data corresponds to slightly offset spatial positions recorded at different times.

$$\mathrm{var}(\Delta\varphi) = \sum_i (\Delta\varphi_{y'-x',i} - \Delta\varphi_{y'-x',t})^2 \tag{2.19}$$

Larger values of var($\Delta\varphi$) corresponds to a lower DOP in the RNFL, and increased variation with increasing RNFL depth indicate degradation in DOP associated with a depolarization process when light propagates through the RNFL. In addition, amplitude variation of the 100 A-scans parallel and perpendicular to fiber axes are also calculated (Eq. 2.20).

$$\begin{aligned} \mathrm{var}(|E_{x'}|) &= \sum_i (|E_{x',i}| - |\overline{E_{x'}}|)^2 \\ \mathrm{var}(|E_{y'}|) &= \sum_i (|E_{y',i}| - |\overline{E_{y'}}|)^2 \end{aligned} \tag{2.20}$$

2.4.2 Variation of phase retardation and intensity

An RNFL cluster ring scan intensity image of a 28 year-old healthy female subject's left eye (Fig. 2.10) centered on the optic nerve head is recorded with a 4 mm ring diameter. Ring scans start in the superior quadrant, pass through temporal, inferior, and nasal quadrants. A total of 36 clusters (cluster 0 to cluster 35) are divided into four quadrants: superior quadrant (clusters 0-5 and cluster 30-35 spanning an azimuthal angle of 120°), temporal quadrant (clusters 6-10 spanning an azimuthal angle of 50°), inferior quadrant (clusters 11-22 spanning an azimuthal angle of 120°), and the nasal quadrant (clusters 23-29 spanning an azimuthal angle of 70°). In the measurement, clusters that correspond to each quadrant may vary or shift by two or three clusters due to patient movement or subject differences. As shown in Fig. 2.10, each cluster consists of 100 A-scans, the average of 100 A-scans' intensity signal is used for cluster segmentation, and anterior and posterior boundary of the RNFL is found based on intensity thresholding and when necessary manually corrected by visual inspection.

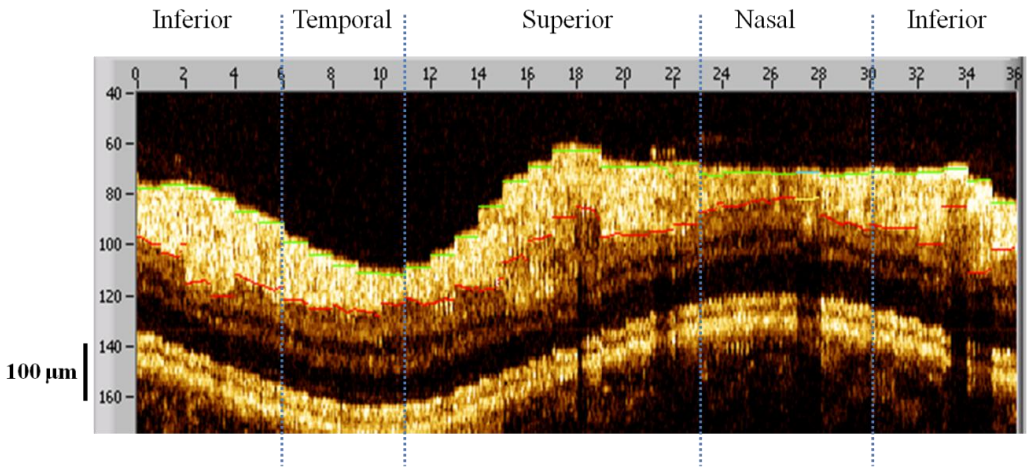

Figure 2.10: A cluster ring scan intensity image of RNFL of a 28 year-old healthy female subject's left eye. Vertical axis represents pixel in depth; horizontal axis on top represents cluster number (0-35); green bars and red bars indicate anterior and posterior boundary of RNFL.

The PS-OCT signal processing method described above (Section 2.4.1) uses a Levenberg-Marquardt fitting algorithm on the Poincaré sphere. To examine changes in the DOP when light propagates in RNFL, we present four clusters' phase retardation, phase retardation variation and intensity variation of three incident states, each with 100 A-scans (Fig. 2.11). In Fig. 2.11, each row represents one cluster, from the top-to-bottom clusters correspond to cluster 3, cluster 6, cluster 16 and cluster 24 in the intensity image (Fig. 2.10); each represents a typical cluster in superior, temporal, inferior and nasal quadrants for comparison. Leftmost column shows phase retardation between fast and slow axes with respect to depth, vertical axis represents phase retardation in the unit of radians, horizontal axis is RNFL depth in pixels (one pixel corresponds to 4.7μm physical depth in RNFL), three solid curves correspond to three incident polarization states on the retina and the dashed lines are a linear fit; middle column is phase retardation variation with respect to depth, solid curve is the sum of the variation of three incident states, and dashed line is a linear fit to estimate the increasing trend of phase retardation variation with depth. Rightmost column is intensity variation along depth, solid curve is the intensity variation of field amplitude along the fast axis, and dashed curve is the intensity variation of the field amplitude along the slow axis, intensity variation is the sum of the variation of three incident states.

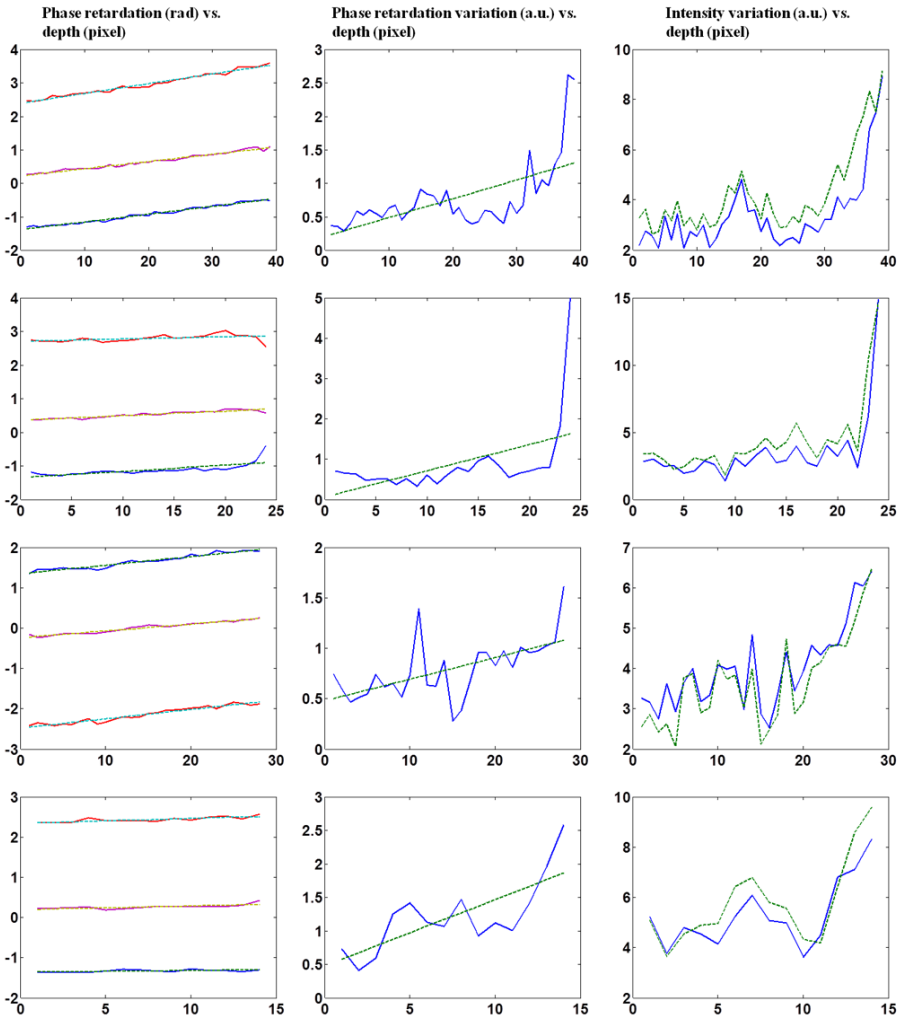

Figure 2.11: Cluster phase retardation vs. depth (leftmost column), phase retardation variation vs. depth (middle column) and intensity variation vs. depth (rightmost column). Each row represents one cluster: Top row is in the superior quadrant, second row from the top is in temporal quadrant, third row from the top is in the inferior quadrant and bottom row is in the nasal quadrant.

Phase retardation between RNFL fast and slow axes vs. depth (Fig. 2.11) is calculated based on averaged PS-OCT data of 100 A-scans and increased with depth- because the RNFL is a weakly birefringent layer. A linear fit is applied to estimate the birefringence (phase retardation per unit depth) for each incident polarization state. Three

incident polarization states are separated with different initial phase retardations introduced by the $LiNbO_3$ polarization modulator. Slope of the linear fit is phase retardation per unit depth; average of the slope over the three states gives cluster birefringence. The cluster in the superior quadrant has a birefringence of 4.44×10^{-4}, cluster in the temporal quadrant has a birefringence of 2.31×10^{-4}, cluster in the inferior quadrant has a birefringence of 3.69×10^{-4}, and cluster in the nasal quadrant has a birefringence of 1.99×10^{-4}. These birefringence values are consistent with values for human RNFL reported previously (41-44). Phase retardation variation is computed by comparing values from each A-scan with the fitted value (Eq. 2.19). The variation is considered to be introduced by polarimetric noise. As shown in the second column of Fig. 2.11, though the variation oscillates about the linear trend line, a general increasing trend is observed with increasing RNFL depth, suggesting a degradation in the DOP with increasing depth due to varying phase. To quantitatively estimate the increasing trend of variation, we use a linear fit to characterize the variation: a larger fitted slope to the trend indicates a more rapid depolarization and faster reduction in the DOP with increasing depth. A linear fit has the advantage to constrain the fitting curve to most of the data without being disturbed by abrupt changes and to clearly illustrate the data trend. Effects not related to optical activity in RNFL (such as abrupt variation increase due to boundary misdetection) can be minimized. Variations in the light amplitudes along the two fibrous tissue sample axes (parallel and perpendicular to nerve fiber) are also computed. Amplitude variations along the fast and slow sample axes follow each other closely, and increase with depth similar to phase retardation variation. The results suggest that degradation in the DOP with increasing RNFL depth is associated with both randomization of phase retardation and an energy transfer between light oscillations parallel and perpendicular to the fiber axes.

The increased variation in phase retardation and amplitude with RNFL depth is clearly observed (Fig. 2.11), Phase retardation variation slope (PRVS) and amplitude variation slope (AVS) of all 36 clusters are computed and presented in Fig. 2.12. For comparison, quadrants are separated by dashed lines in Fig. 2.12 based on the azimuthal angular boundaries indicated above. Clusters in superior and inferior quadrants have relatively small PRVS and AVS; clusters in the nasal quadrant exhibit larger PRVS and AVS, and clusters in the temporal quadrant have the highest PRVS and AVS, which corresponds to the most rapid degradation in the DOP with increased RNFL depth.

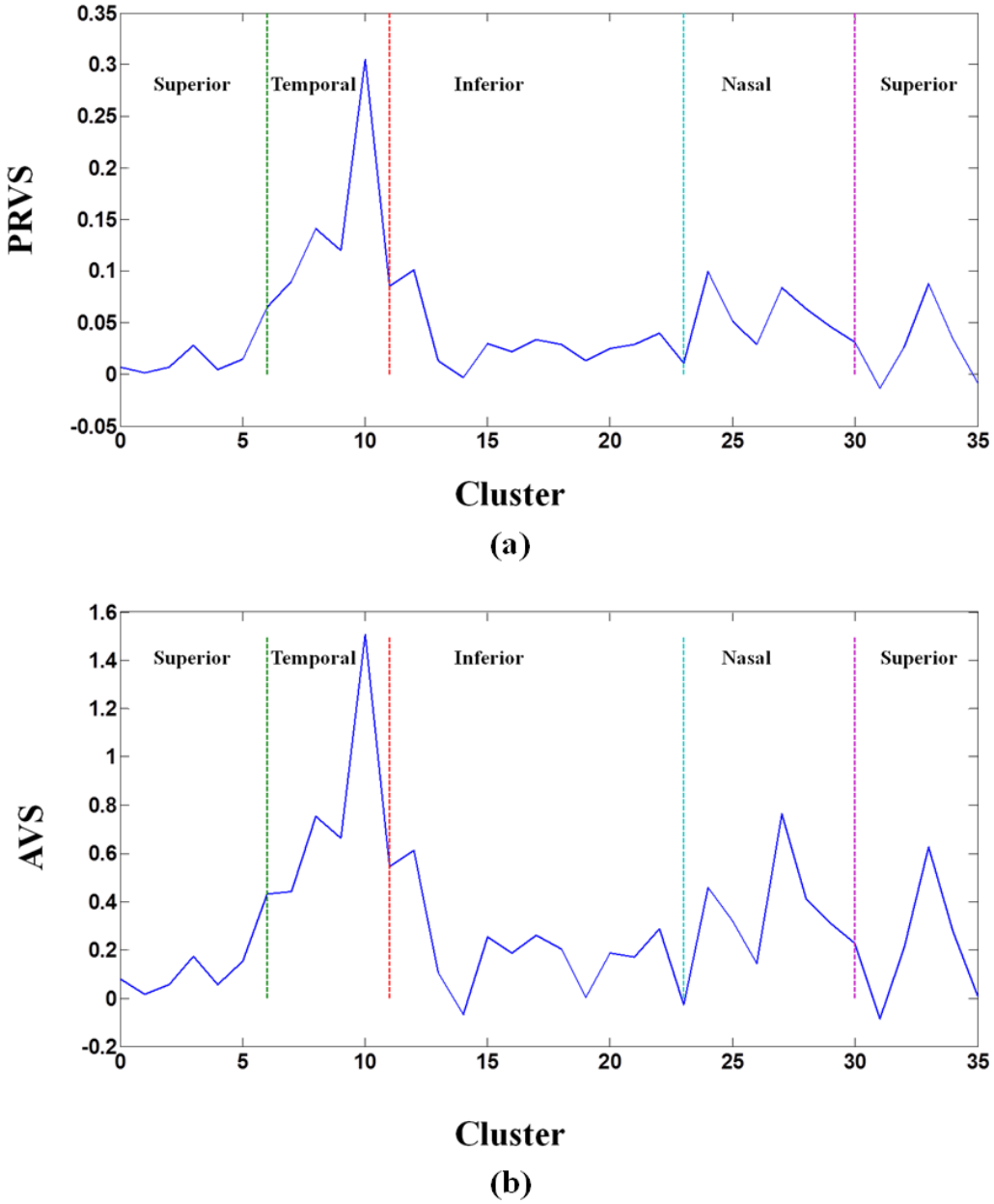

Figure 2.12: (a) PRVS vs. cluster. (b) AVS vs. cluster. Quadrants are separated by dashed lines.

PS-OCT data from 10 healthy subjects with age ranging from 20 to 70 were collected for this study. All clinical data were collected with IRB approval and the

clinical trial is registered as NCT01222065. Cluster polarization data was recorded at rings with diameter 3-4 mm centered on the optic nerve head (right eye in 3 subjects and left eye in 7 subjects), and processed to obtain the PRVS and AVS of each cluster. For each subject, the average of PRVS is calculated for each quadrant (R_1, R_2, R_3, R_4) to represent the reduction of DOP in the quadrant (Subscripts 1-4 correspond to superior, temporal, inferior and nasal respectively). The PRVS (R_1, R_2, R_3, R_4) were normalized for each subject by

$$NR_i = R_i / \sum_{j=1}^{4} R_j \tag{2.21}$$

With 10 sets of (NR_1, NR_2, NR_3, NR_4) we are able to calculate the mean and standard deviation of normalized average PRVS (Fig. 2.13a) for four quadrants. In a similar way, mean and standard deviation of normalized average AVS in each quadrant is also calculated (Fig. 2.13b). Strongest degradation in DOP with increasing RNFL depth is observed in the temporal quadrant compared with the other three quadrants.

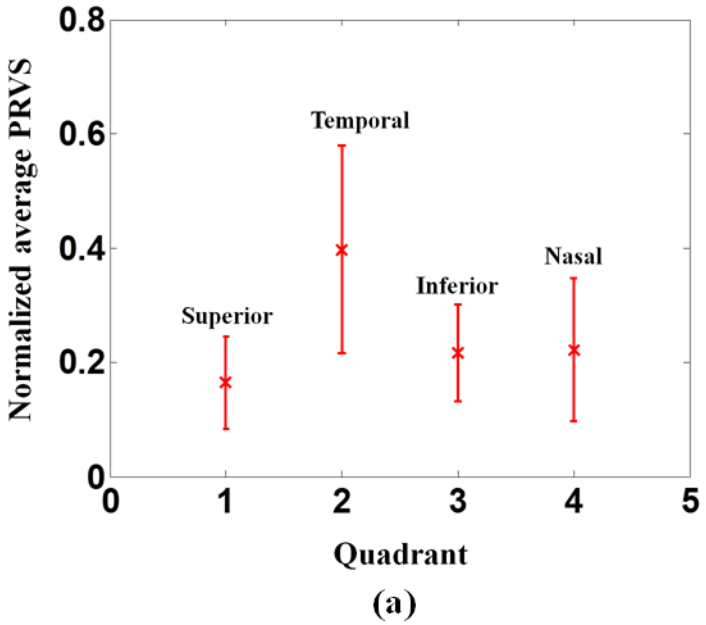

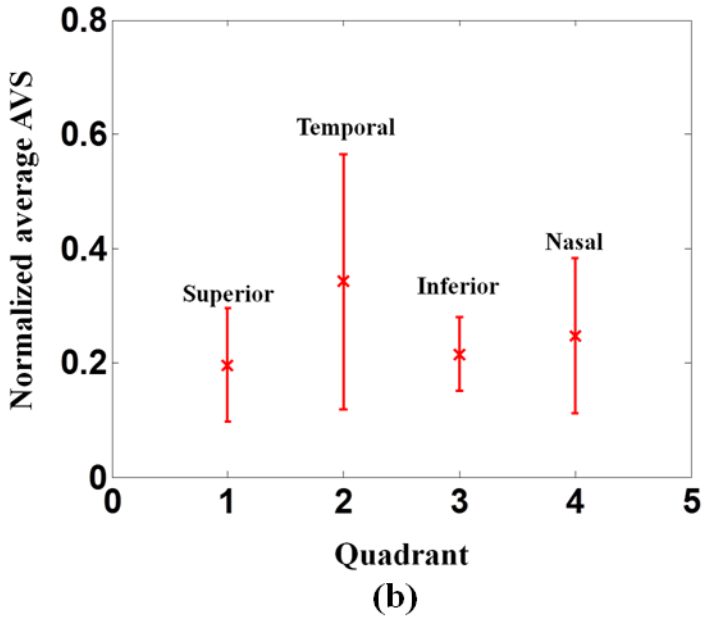

Figure 2.13: (a) Mean and standard deviation of 10 subjects' normalized average PRVS in each quadrant. (b) Mean and standard deviation of 10 subjects' normalized average AVS in each quadrant.

A paired t-test (Tab. 2.2) is applied to examine the difference in normalized average PRVS between superior and temporal, inferior and temporal, nasal and temporal. The two-tail p-values for superior compared with temporal (0.016) and inferior compared with temporal (0.028) show statistical significance (<0.05).

	p-value (two-tail)
Superior vs. Temporal	0.016
Inferior vs. Temporal	0.028
Nasal vs. Temporal	0.089

Table 2.2: Paired t-test p-value (two-tail) of normalized average PRVS for superior vs. temporal, inferior vs. temporal, and nasal vs. temporal.

The paired t-test for normalized average AVS is also presented (Tab. 2.3). But the difference between temporal and other three quadrants (superior, inferior and nasal) doesn't show statistical significance. As according to Eqs 2.16 and 2.17, phase retardation variation relates directly to the DOP, we consider normalized average PRVS as a better indicator of depolarization process and can be used to distinguish temporal from the other three quadrants.

	p-value (two-tail)
Superior vs. Temporal	0.18
Inferior vs. Temporal	0.13
Nasal vs. Temporal	0.41

Table 2.3: Paired t-test p-value (two-tail) of normalized average AVS for superior vs. temporal, inferior vs. temporal, and nasal vs. temporal.

2.5 Discussion on Degradation of Degree of Polarization in RNFL

For a PS-OCT system, polarimetric noise includes contributions from instrumentation and the sample tissue. In fiber based PS-OCT systems, polarization mode dispersion (PMD) (45) in fiber and optical components such as circulator is believed to contribute to the polarimetric noise in the birefringence measurement (46-47), and approaches have been proposed to compensate for the PMD introduced by single mode fiber and other optical components (48). The other source that contributes to polarimetric noise is the tissue. This polarimetric noise is associated with the structural properties of tissue. When light propagates in the tissue, multiple scattering events can randomize the phase retardation, and scattering caused by an irregularly shaped tissue structures can introduce an abrupt change in polarization state of backscattered light. The application of tissue's depolarization property may be included in segmentation of the depolarization layer by examining degree of polarization uniformity (41).

Reduction in the DOP with increasing RNFL depth is found to vary between RNFL quadrants. As presented in Fig. 2.13, Tabs. 2.2 and 2.3, superior and inferior quadrants exhibit less reduction in the DOP, while the nasal quadrant has relatively stronger reduction in the DOP, and temporal has the most significant reduction. In RNFL, superior and inferior quadrants have higher microtubule density than temporal and nasal quadrants; superior and inferior quadrants have highest birefringence; and the polarimetric noise has less impact on the polarization states of backscattered light when light is propagating in the structure with higher birefringence. In temporal quadrant, RGC axons are known to have the smallest diameter (49), and presumably exhibit a larger scattering angle than the other three quadrants; we expect that a larger scattering angle is associated with an increase in scattering events and can introduce higher polarimetric noise and reduce the DOP of incident light. Highest PRVS and AVS are observed in the temporal quadrant. The assumption of a larger scattering angle in the temporal quadrant can be verified by measuring and comparing the backscattering angle of different quadrants. Ten healthy human subjects' normalized average PRVS and AVS data suggests the phase retardation variation is a better indicator of depolarization than amplitude variation and can be used to distinguish temporal quadrant from other three quadrants (superior, inferior and nasal).

2.6 Angle-Resolved Optical Coherence Tomography

2.6.1 Motivation of Angle-Resolved Optical Coherence Tomography

As discussed above, degradation of the degree of polarization (DOP) of backscattered light in human RNFL, which may be associated with scattering angle and can be applied to indicate fiber tissue structural properties. A previous study (50) has also

shown that in non-human primates, decreased RNFL reflectance was the most robust correlate with glaucomatous damage. Potential candidate mechanisms for RNFL reflectance decrease include changes in the mitochondrial networks and axonal cytoskeleton changes. Mitochondria are recognized as dynamic organelles that constantly undergo fusion and fission processes. Fusion of mitochondria can form interconnected intracellular networks to maintain a mitochondrial population with a full complement of gene products that can mitigate age-related degeneration; recent study (51) has demonstrated that mitochondrial fission in differentiated retinal ganglion cell cultures is induced in response to elevated hydrostatic pressures. Studies have observed optical scattering changes in cells undergoing apoptosis that originate at least in part from the mitochondria. A Fourier microscopy approach has been applied to demonstrate that early cell apoptosis is accompanied by mitochondrial fission and fragmentation that results in more isotropic or large-angle light scattering (52); an angle-resolved OCT has been used to record similar scattering changes which may involve mitochondrial fission (53). Investigators also have applied OCT to record light scattering changes in cells undergoing apoptosis or necrosis (54-55). We believe intensified mitochondrial fission can increase large angle scattering, which can decrease the reflectance of a tissue sample, other mechanisms such as changes in the axonal membrane or microtubules may also contribute to the observed decrease in RNFL reflectance.

2.6.2 Design of Angle-Resolved Optical Coherence Tomography

Angle-resolved optical coherence tomography (AS-OCT) provides additional information that can be used to measure the structural properties of tissues. Angle-resolved OCT systems have been developed based on various imaging techniques. Mie

theory-a model for spherical scattering and the T-matrix-a method for computing aspherical scattering have been used as an inverse model to estimate scattering angle (56-58), and later combined with a fiber-optic interferometric two-dimensional scattering system (59) for data acquisition, two-dimensional solid angle resolved measurements can be achieved (60). Another approach for angle-resolved measurement is joint-aperture OCT, which uses multiple detection channels, and each channel receives backscattered light with a certain angle (61).

Here, we introduce an angle-resolved OCT system based on pathlength multiplexing. Different pathlength multiplexing elements (PME) are designed for different measurement (Fig. 2.14).

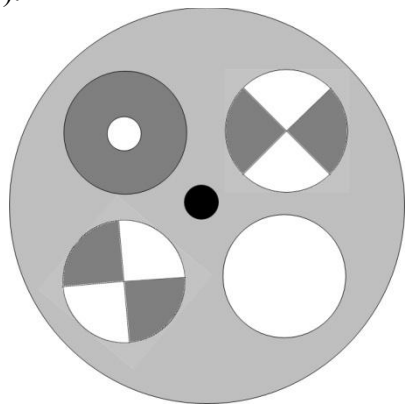

Figure 2.14: Pathlength multiplexing elements (PME) on a wheel.

In Fig. 2.14, three PMEs are attached on the same wheel, which is convenient to switch from one PME to the other, PMEs can be placed in the OCT sample arm (typically PMEs are inserted after the lens which collimates the light out of fiber tip (Fig. 2.15)). The upper left PME is a radial angle-resolved PME. The PME may be a glass plate with different optical thickness between inner ring and outer ring in order to introduce the pathlength difference: if we assume inner ring has a lower refractive index than outer ring, light that travels through inner ring has a short optical pathlength while that travels

through outer ring has a long optical pathlength (Fig. 2.16). Due to double-pass propagation, three sub-images will be constructed: short-short (incident light goes through inner ring and backscattered light goes through inner ring), short-long/long-short (incident light goes through inner ring and backscattered light goes through outer ring or incident light goes through outer ring and backscattered light goes through inner ring) and long-long (incident light goes through outer ring and backscattered light goes through outer ring). The intensity difference between sub-images indicates the difference in backscattering angle: short-short corresponds to low angle incident-low angle backscattered, short-long/long-short corresponds to low angle incident-high angle backscattered or high angle incident-low angle backscattered, and long-long corresponds to high angle incident-high angle backscattered. Based on similar principle, the PME on the upper right is design to resolve the azimuthal angle. And the PME on the lower left is identical to the one on upper right but with a 45° rotation in order to observe difference between quadrants. The lower right element is used for the case when no PME is needed.

PMEs can be combined with our current polarization-sensitive OCT system (Fig. 2.15) for an angle-resolved polarization-sensitive measurement.

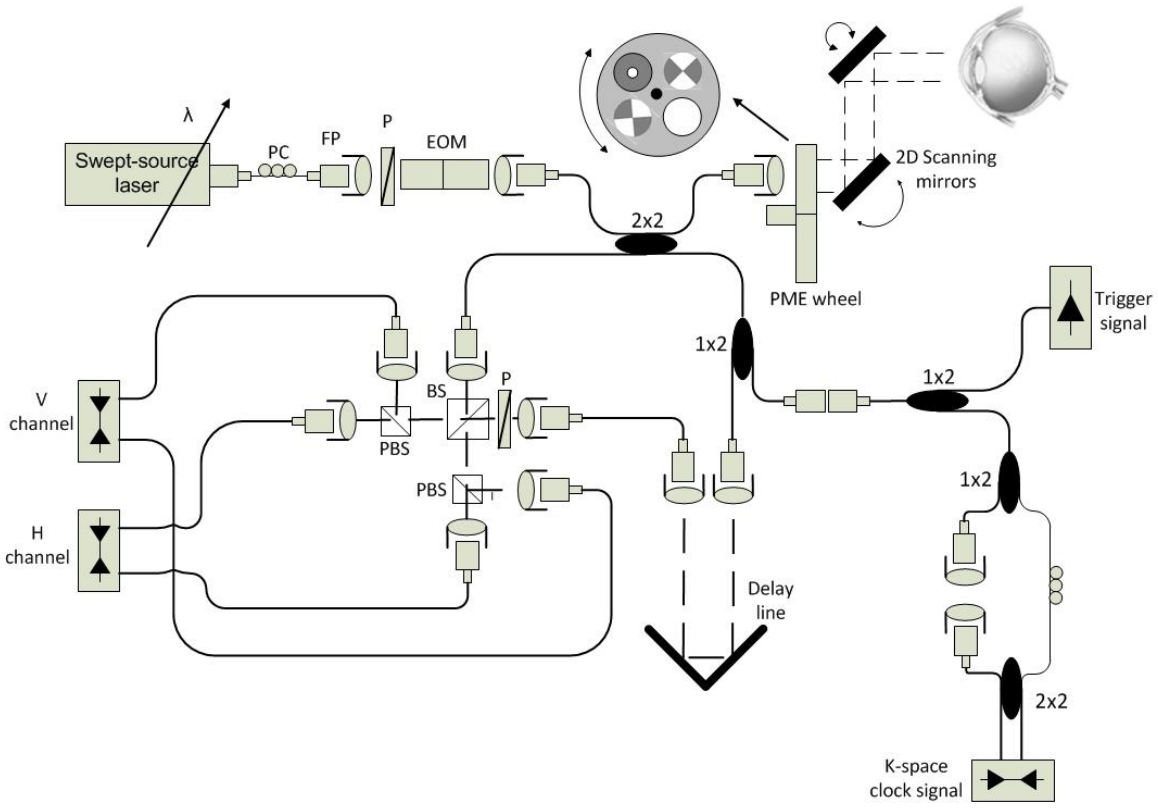

Figure 2.15: Proposed angle-resolved polarization-sensitive OCT system.

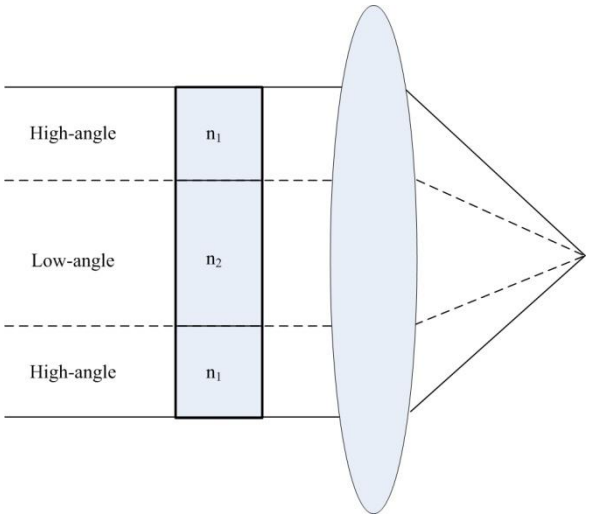

Figure 2.16: Radial angle-resolved PME.

2.7 FIBER POLARIMETER FOR POLARIZATION-SENSITIVE DETECTION

2.7.1 Motivation of Fiber Polarimeter

In last section, an angle-resolved polarization-sensitive optical coherence tomography is introduced. Compared with traditional OCT image formation, three sub-images are constructed based on different incident and backscattered angles, detected signal is split into each sub-image; when birefringence information is needed, a polarization-sensitive detection module is utilized to separate backscattered light into two orthogonal channels, which further reduce the signal level in each sub-image. Considering substantial signal loss due to alignment and coupling can exist in a polarization-sensitive bulk-optics detection module, a fiber based polarimeter is proposed for polarization-sensitive detection to improve image quality and birefringence measurement accuracy.

2.7.2 Fiber Polarimeter

Feasibility of fiber-based polarization-sensitive spectral interferometry has been demonstrated (62-63) and can be translated for our application.

Fig. 2.17 shows the polarization-sensitive OCT detection arm design based on a fiber polarimeter. Reference light and light reflected from sample is combined through a 1X2 fiber coupler. After reference light and sample light interfere, it is split into two channels (V-channel and H-channel) in alignment with polarization-maintaining (PM) fiber 1's fast and slow axes, and another segment of PM fiber PM fiber 2 is spliced to PM fiber 1 with an angle of 45° with respect to the axes in PM fiber 1. A fiber polarization

beam splitter is used to split the light into two channels of balanced photodetector, the axes of polarization beam splitter are coaligned with the axes in PM fiber 1.

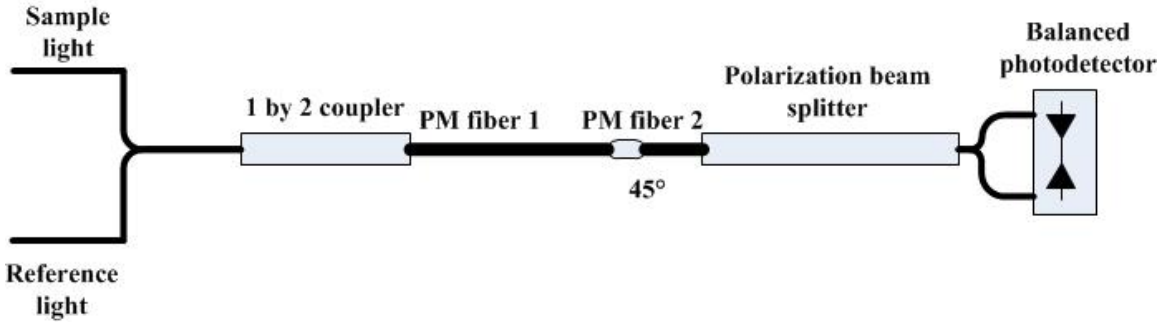

Figure 2.17: Fiber polarimeter for polarization-sensitive OCT.

A Jones matrix based method can be applied to investigate the detected OCT signal. Assume an optical pathlength difference between sample light and reference light is Δz, the sample light E_s and reference light E_r can be written as

$$E_s(k) = \begin{pmatrix} E_{sv} e^{j(k\Delta z + \Delta\varphi/2)} \\ E_{sh} e^{j(k\Delta z - \Delta\varphi/2)} \end{pmatrix}$$
$$E_r(k) = \begin{pmatrix} E_{rv} \\ E_{rh} \end{pmatrix} \tag{2.22}$$

Where E_{sv} is the electric field of sample light along vertical direction, E_{sh} is the electric field of sample light along horizontal direction; E_{rv} and E_{rh} represent the electric field of reference light along vertical and horizontal directions. $k\Delta z$ is the phase difference between sample light and reference light due to optical pathlength difference, $\Delta\varphi$ represents phase retardation of electric field in vertical and horizontal directions introduced by sample birefringence.

After entering the 1X2 fiber coupler, reference light and sample light interfere, interference electric field becomes

$$E_{in,1}(k)=\begin{pmatrix} E_{sv}e^{j(k\Delta z+\Delta\varphi/2)}+E_{rv} \\ E_{sh}e^{j(k\Delta z-\Delta\varphi/2)}+E_{rh} \end{pmatrix} \tag{2.23}$$

After the light passes through PM fiber 1 with length l_1, the phase of light in V-channel and H-channel are modified.

$$E_{in,2}(k)=\begin{pmatrix} (E_{sv}e^{j(k\Delta z+\Delta\varphi/2)}+E_{rv})e^{j\Delta nkl_1} \\ E_{sh}e^{j(k\Delta z-\Delta\varphi/2)}+E_{rh} \end{pmatrix} \tag{2.24}$$

Where Δn is the refractive index difference between PM fiber's fast and slow axes.

PM fiber 2 has a 45° axes rotation with respect to PM fiber 1, so a rotation matrix is applied and assume PM fiber 2's length is l_2.

$$\begin{aligned} E_{in,3}(k)&=\begin{pmatrix} \cos 45^\circ & \sin 45^\circ \\ -\sin 45^\circ & \cos 45^\circ \end{pmatrix}\begin{pmatrix} e^{j\Delta nkl_2} & 0 \\ 0 & 1 \end{pmatrix}\begin{pmatrix} \cos 45^\circ & -\sin 45^\circ \\ \sin 45^\circ & \cos 45^\circ \end{pmatrix}E_{in,2}(k) \\ &=1/2\begin{pmatrix} E_{sv}e^{j\left[k\Delta z+\Delta\varphi/2+\Delta nk(l_1+l_2)\right]}+E_{sv}e^{j[k\Delta z+\Delta\varphi/2+\Delta nkl_1]}+E_{rv}e^{j\Delta nk(l_1+l_2)}+E_{rv}e^{j\Delta nkl_1} \\ -E_{sh}e^{j[k\Delta z-\Delta\varphi/2+\Delta nkl_2]}+E_{sh}e^{j[k\Delta z-\Delta\varphi/2]}-E_{rh}e^{j\Delta nkl_2}+E_{rh} \\ -E_{sv}e^{j\left[k\Delta z+\Delta\varphi/2+\Delta nk(l_1+l_2)\right]}+E_{sv}e^{j[k\Delta z+\Delta\varphi/2+\Delta nkl_1]}-E_{rv}e^{j\Delta nk(l_1+l_2)}+E_{rv}e^{jk\Delta nl_1} \\ +E_{sh}e^{j[k\Delta z-\Delta\varphi/2+\Delta nkl_2]}+E_{sh}e^{j[k\Delta z-\Delta\varphi/2]}+E_{rh}e^{j\Delta nkl_2}+E_{rh} \end{pmatrix} \end{aligned} \tag{2.25}$$

Polarization beam splitter splits $E_{in,3}$ into V-channel ($E_{in,3v}$) and H-channel ($E_{in,3h}$), and the interference signal intensity I_v and I_H is written as

$$
\begin{aligned}
I_v(k) &= E_{in,3v}(k)E_{in,3v}(k)^* \\
&= \frac{1}{2}\left\{\begin{array}{l}
{E_{sv}}^2 + {E_{rv}}^2 + {E_{sh}}^2 + {E_{rh}}^2 \\
+{E_{sv}}^2\cos(\Delta nkl_2) + 2E_{sv}E_{rv}\cos(k\Delta z + \Delta\varphi/2) \\
+E_{sv}E_{rv}\cos(k\Delta z + \Delta\varphi/2 + \Delta nkl_2) + E_{sv}E_{sh}\cos[\Delta\varphi + \Delta nk(l_1 + l_2)] \\
+E_{sv}E_{rh}\cos[k\Delta z + \Delta\varphi/2 + \Delta nk(l_1 + l_2)] \\
+E_{sv}E_{rv}\cos(k\Delta z + \Delta\varphi/2 - \Delta nkl_2) - E_{sv}E_{sh}\cos[\Delta\varphi + \Delta nk(l_1 - l_2)] \\
-E_{sv}E_{rh}\cos[k\Delta z + \Delta\varphi/2 + \Delta nk(l_1 - l_2)] + {E_{rv}}^2\cos(\Delta nkl_2) \\
+E_{rv}E_{sh}\cos[-k\Delta z + \Delta\varphi/2 + \Delta nk(l_1 + l_2)] + E_{rv}E_{rh}\cos\Delta nk(l_1 + l_2) \\
-E_{rv}E_{sh}\cos[-k\Delta z + \Delta\varphi/2 + \Delta nk(l_1 - l_2)] - E_{rv}E_{rh}\cos\Delta nk(l_1 - l_2) \\
-{E_{sh}}^2\cos(\Delta nkl_2) + 2E_{sh}E_{rh}\cos(k\Delta z - \Delta\varphi/2) \\
-E_{sh}E_{rh}\cos(k\Delta z - \Delta\varphi/2 + \Delta nkl_2) - E_{sh}E_{rh}\cos(k\Delta z - \Delta\varphi/2 - \Delta nkl_2) \\
-{E_{rh}}^2\cos(\Delta nkl_2)
\end{array}\right\}
\end{aligned}
\tag{2.26}
$$

$$
\begin{aligned}
I_h(k) &= E_{in,3h}(k)E_{in,3h}(k)^* \\
&= \frac{1}{2}\left\{\begin{array}{l}
{E_{sv}}^2 + {E_{rv}}^2 + {E_{sh}}^2 + {E_{rh}}^2 \\
-{E_{sv}}^2\cos(\Delta nkl_2) + 2E_{sv}E_{rv}\cos(k\Delta z + \Delta\varphi/2) \\
-E_{sv}E_{rv}\cos(k\Delta z + \Delta\varphi/2 + \Delta nkl_2) - E_{sv}E_{sh}\cos[\Delta\varphi + \Delta nk(l_1 + l_2)] \\
-E_{sv}E_{rh}\cos[k\Delta z + \Delta\varphi/2 + \Delta nk(l_1 + l_2)] \\
-E_{sv}E_{rv}\cos(k\Delta z + \Delta\varphi/2 - \Delta nkl_2) + E_{sv}E_{sh}\cos[\Delta\varphi + \Delta nk(l_1 - l_2)] \\
+E_{sv}E_{rh}\cos[k\Delta z + \Delta\varphi/2 + \Delta nk(l_1 - l_2)] - {E_{rv}}^2\cos(\Delta nkl_2) \\
-E_{rv}E_{sh}\cos[-k\Delta z + \Delta\varphi/2 + \Delta nk(l_1 + l_2)] - E_{rv}E_{rh}\cos\Delta nk(l_1 + l_2) \\
+E_{rv}E_{sh}\cos[-k\Delta z + \Delta\varphi/2 + \Delta nk(l_1 - l_2)] + E_{rv}E_{rh}\cos\Delta nk(l_1 - l_2) \\
+{E_{sh}}^2\cos(\Delta nkl_2) + 2E_{sh}E_{rh}\cos(k\Delta z - \Delta\varphi/2) \\
+E_{sh}E_{rh}\cos(k\Delta z - \Delta\varphi/2 + \Delta nkl_2) + E_{sh}E_{rh}\cos(k\Delta z - \Delta\varphi/2 - \Delta nkl_2) \\
+{E_{rh}}^2\cos(\Delta nkl_2)
\end{array}\right\}
\end{aligned}
\tag{2.27}
$$

For a balanced detector, the signal output $I(k)$ will be the difference between $I_v(k)$ and $I_h(k)$.

$$
\begin{aligned}
I(k) &= E_{sv}{}^2\cos(\Delta nkl_2) + E_{sv}E_{rv}\cos(k\Delta z + \Delta\varphi/2 + \Delta nkl_2) \\
&+ E_{sv}E_{sh}\cos[\Delta\varphi + \Delta nk(l_1 + l_2)] + E_{sv}E_{rh}\cos[k\Delta z + \Delta\varphi/2 + \Delta nk(l_1 + l_2)] \\
&+ E_{sv}E_{rv}\cos(k\Delta z + \Delta\varphi/2 - \Delta nkl_2) - E_{sv}E_{sh}\cos[\Delta\varphi + \Delta nk(l_1 - l_2)] \\
&- E_{sv}E_{rh}\cos[k\Delta z + \Delta\varphi/2 + \Delta nk(l_1 - l_2)] + E_{rv}{}^2\cos(\Delta nkl_2) \\
&+ E_{rv}E_{sh}\cos[-k\Delta z + \Delta\varphi/2 + \Delta nk(l_1 + l_2)] + E_{rv}E_{rh}\cos\Delta nk(l_1 + l_2) \\
&- E_{rv}E_{sh}\cos[-k\Delta z + \Delta\varphi/2 + \Delta nk(l_1 - l_2)] - E_{rv}E_{rh}\cos\Delta nk(l_1 - l_2) \\
&- E_{sh}{}^2\cos(\Delta nkl_2) - E_{sh}E_{rh}\cos(k\Delta z - \Delta\varphi/2 + \Delta nkl_2) \\
&- E_{sh}E_{rh}\cos(k\Delta z - \Delta\varphi/2 - \Delta nkl_2) - E_{rh}{}^2\cos(\Delta nkl_2)
\end{aligned}
\tag{2.28}
$$

Rearrange terms in Eq. 2.28, we have

$$I(k) = I_1(k) + I_2(k) + I_3(k)$$

$$
\begin{aligned}
I_1(k) &= E_{sv}{}^2\cos(\Delta nkl_2) + E_{rv}{}^2\cos(\Delta nkl_2) - E_{sh}{}^2\cos(\Delta nkl_2) \\
&- E_{rh}{}^2\cos(\Delta nkl_2) + E_{sv}E_{rv}\cos[k(-\Delta z + \Delta nl_2) - \Delta\varphi/2] \\
&- E_{sh}E_{rh}\cos[k(\Delta z + \Delta nl_2) - \Delta\varphi/2] + E_{sv}E_{rv}\cos[k(\Delta z + \Delta nl_2) + \Delta\varphi/2] \\
&- E_{sh}E_{rh}\cos[k(-\Delta z + \Delta nl_2) + \Delta\varphi/2]
\end{aligned}
\tag{2.29}
$$

$$
\begin{aligned}
I_2(k) &= E_{sv}E_{sh}\cos[\Delta nk(l_1 + l_2) + \Delta\varphi] + E_{rv}E_{rh}\cos\Delta nk(l_1 + l_2) \\
&+ E_{sv}E_{rh}\cos[k(\Delta z + \Delta n(l_1 + l_2)) + \Delta\varphi/2] + E_{sh}E_{rv}\cos[k(-\Delta z + \Delta n(l_1 + l_2)) + \Delta\varphi/2]
\end{aligned}
$$

$$
\begin{aligned}
I_3(k) &= -E_{sv}E_{sh}\cos[\Delta nk(l_1 - l_2) + \Delta\varphi] - E_{rv}E_{rh}\cos\Delta nk(l_1 - l_2) \\
&- E_{sv}E_{rh}\cos[k(\Delta z + \Delta n(l_1 - l_2)) + \Delta\varphi/2] - E_{sh}E_{rv}\cos[k(-\Delta z + \Delta n(l_1 - l_2)) + \Delta\varphi/2]
\end{aligned}
$$

In Eq. 2.29, $I(k)$ is decomposed into $I_1(k)$, $I_2(k)$ and $I_3(k)$. After Fourier transform, $I_1(k)$ will generate the image that corresponds to the original image but shifted by Δnl_2, $I_2(k)$ will generate the image that corresponds to the original image but shifted by $\Delta n(l_1+l_2)$, and $I_3(k)$ will generate the image that corresponds to the original image but shifted by $\Delta n(l_1-l_2)$. With this fiber polarimeter, DC noise is balanced, while Stokes parameters of sample can be constructed from the multiplexed signals (62-63).

The fiber polarimeter provides convenience in construction and alignment compared with polarization-sensitive bulk-optics balanced detection module, improves

the signal-to-noise ratio, and depth-resolved Stokes parameters of backscattered light can be constructed from the multiplexed signals. A swept-source laser with longer coherence length is needed as well as a high-speed data acquisition system in order to extend the imaging depth and avoid aliasing.

2.8 CONCLUSION ON PS-OCT STUDY

In this study, a single mode fiber based swept-source PS-OCT clinical system is constructed. The PS-OCT system includes a polarization controller which is able to introduce three incident polarization states onto the sample. A polarization-sensitive bulk-optics balanced detection module is designed and constructed, gives an approximately 3 dB SNR improvement and reduces the polarimetric noise introduced by single mode fiber.

PS-OCT demonstrates its capability of human RNFL birefringence measurement in the clinical study conducted in Eye Institute of Austin and Duke Eye Center, 80 subjects' PS-OCT data are recorded.

A polarization processing method is developed for investigation of degradation in the degree of polarization (DOP) with increasing depth in RNFL. An increase in phase retardation variation with increasing RNFL depth is observed and demonstrates the degradation in the DOP. Ten healthy subjects' cluster ring scan polarization data is analyzed and suggests that difference in degradation of the DOP between quadrants may be associated with known structural properties of microtubules in RNFL axons.

An angle-resolved polarization-sensitive OCT system is proposed in the end of this chapter, which is able to resolve backscattering angle in the PS-OCT measurement based on pathlength multiplexing technique. And a fiber polarimeter is designed for

polarization-sensitive detection, which provides convenience in alignment and improves system SNR.

Chapter 3: Dual-Wavelength Photothermal Optical Coherence Tomography for Blood Oxygen Saturation Measurement

3.1 Introduction of DWP-OCT Study

Non-invasive quantitative evaluation of microvasculature hemoglobin oxygen saturation (SO_2) in tissue is important in early detection and monitoring progression of inflammatory and ischaemic diseases such as cancer, stroke and glaucoma (18-19). Various approaches have been used to assess in vivo microvascular oxygen saturation including oxygen-sensitive microelectrodes (64-68), magnetic resonance imaging (MRI) (69-73), reflection spectroscopic oximetry (74-79) and phosphorescence quenching (PQ) (78, 80-85). Measurement by oxygen-sensitive microelectrodes is a point measurement and primarily limited to animal studies; MRI has limited spatial (100-150 μm) and temporal (tens of second to minutes) resolution; the phosphorescence quenching technique has limited spatial resolution (e.g. 50 μm) and no oxygen sensitive dyes that are approved by the United States FDA are available for clinical translation.

Biomedical investigators are interested in applying OCT approaches to measure microvasculature SO_2 in tissues. Spectroscopic Fourier Domain OCT (SFD-OCT) (86-87) has been reported to measure depth-resolved microvasculature oxygenation, but an appropriate model has not been given to estimate attenuation coefficients required to determine blood SO_2 levels using OCT light in the near infrared spectral region (88). SFD-OCT has been shown to provide sufficient sensitivity to quantify microvascular SO_2 levels using visible wavelengths (460-700 nm) where hemoglobin absorption is relatively large (89-90). However, SFD-OCT using visible wavelength sources is compromised due to limited imaging depth which is restricted by increased scattering.

Photothermal OCT is a functional imaging technique that is able to measure optical pathlength variation of OCT light backscattered from tissues in response to an excitation beam. Adler has demonstrated photothermal OCT using a gold nanoparticle contrast agent (91); Skala has developed photothermal OCT for high resolution molecular imaging (92); and Paranjape has reported using photothermal OCT to detect macrophages in tissue (93). So far, reported applications of photothermal OCT have focused primarily on light absorption by nanoparticles. Previously, our group reported using dual-wavelength photothermal OCT (DWP-OCT) to measure microvasculature SO_2 both in phantom (94) and in vivo (95) blood vessels using a common-path Phase-Sensitive (PhS) OCT system (96). Because a common path interferometer was used, imaging by scanning the beam was difficult and results were limited to point microvasculature SO_2 measurement. Compared to two-beam interferometers, common path interferometry provides higher sensitivity and stability to measure phase of interference fringes of light backscattered from transparent and scattering media. Despite these advantages, several drawbacks of prior common-path DWP-OCT system (94-96) design are recognized: 1) recording en-face images is challenged by incorporating a 2D scanning system into the sample arm; 2) a short working distance associated with common-path DWP-OCT introduces problems for the operator to position the OCT probe beam at a desired sample measurement location; 3) the short working distance makes intravascular, retinal and endoscopic applications challenging.

In this study I constructed a DWP-OCT system that uses two-beam interferometer and allows for both imaging and measurement of SO_2 levels. Phantom blood vessels are used for blood SO_2 measurement, DWP-OCT measurement results are compared with commercial oximeter measurement values. Error analysis is provided, and the influence of blood flow and thermal diffusion on DWP-OCT measurement is investigated.

3.2 HARDWARE IMPLEMENT OF DWP-OCT

In this study, a DWP-OCT system using a fiber Michelson interferometer was constructed for imaging and blood SO_2 measurement. Interferometric fringe phase stabilization is a critical feature required for SO_2 measurement. In a generic phase-sensitive swept-source (SS) OCT system, two mechanisms contribute to phase noise: 1) inconsistency of the start wavelength between successive A-scans; and 2) non-specific mechanical movement of optical elements in sample and reference arms. To resolve the first issue, 5% of light in the sample arm is coupled to a high-reflectivity mirror which is sufficient to form a high SNR interference fringe signal with reference light but too weak to introduce an artifactual autocorrelation and interference signal with light backscattered from the sample. Light reflecting from a high-reflectivity mirror in the sample path introduces a feature-line in recorded B-scans positioned below the image sample and does not compromise image quality. To minimize the second source of phase noise (due to non-specific mechanical movement of optical elements), the sample beam scanning system is constructed using a stable mechanical cage system.

Blood SO_2 measurement value is dependent on the ratio (χ) of optical pathlength (*op*) signal amplitude at modulation frequencies introduced by 770 nm and 800 nm photothermal excitation light. To balance incident fluence of photothermal excitation beams, the scanning optics is designed to provide nearly equivalent spot sizes for 770 nm and 800 nm light. Fig. 3.1 shows molar extinction coefficient for oxygenated hemoglobin (HbO_2) and deoxygenated hemoglobin (Hb). The absorption coefficients of HbO_2 and Hb are similar at 800 nm while they differ significantly from each other at 770 nm.

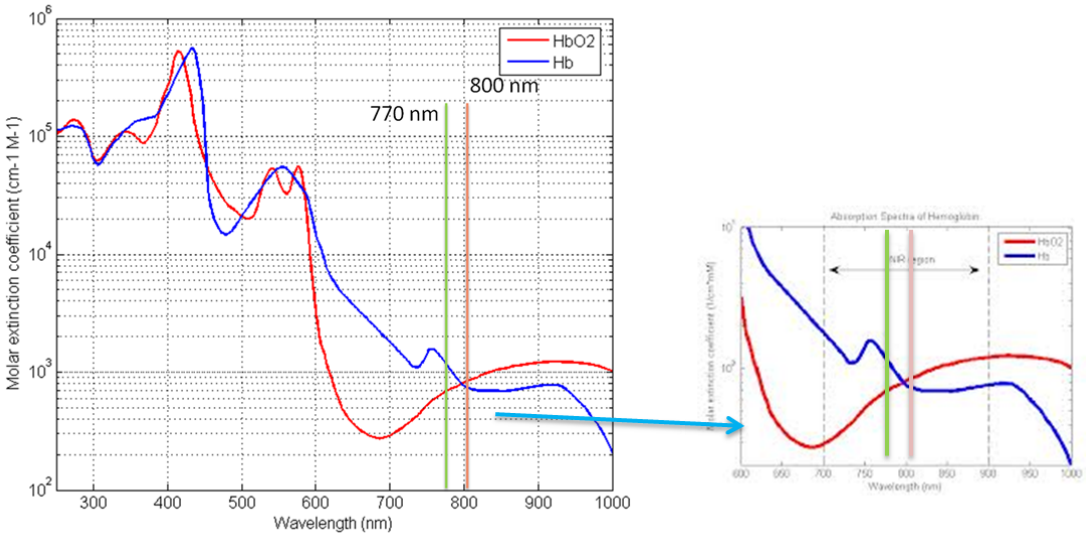

Figure 3.1: Molar extinction coefficient for oxygenated hemoglobin (HbO_2) and deoxygenated hemoglobin (Hb).

DWP-OCT system (Fig. 3.2) for imaging and blood SO_2 measurement consists of two major systems: 1) a swept-source Phase-Sensitive (PhS) OCT system that provides accurate depth-resolved phase measurement with a 300 pm lower bound of detectable *op* signal amplitude; and 2) two excitation lasers (770 nm and 800 nm) that are intensity modulated at 400 Hz and 380 Hz, respectively, and introduce a nanometer-scale harmonic *op* signal amplitude due to blood absorption.

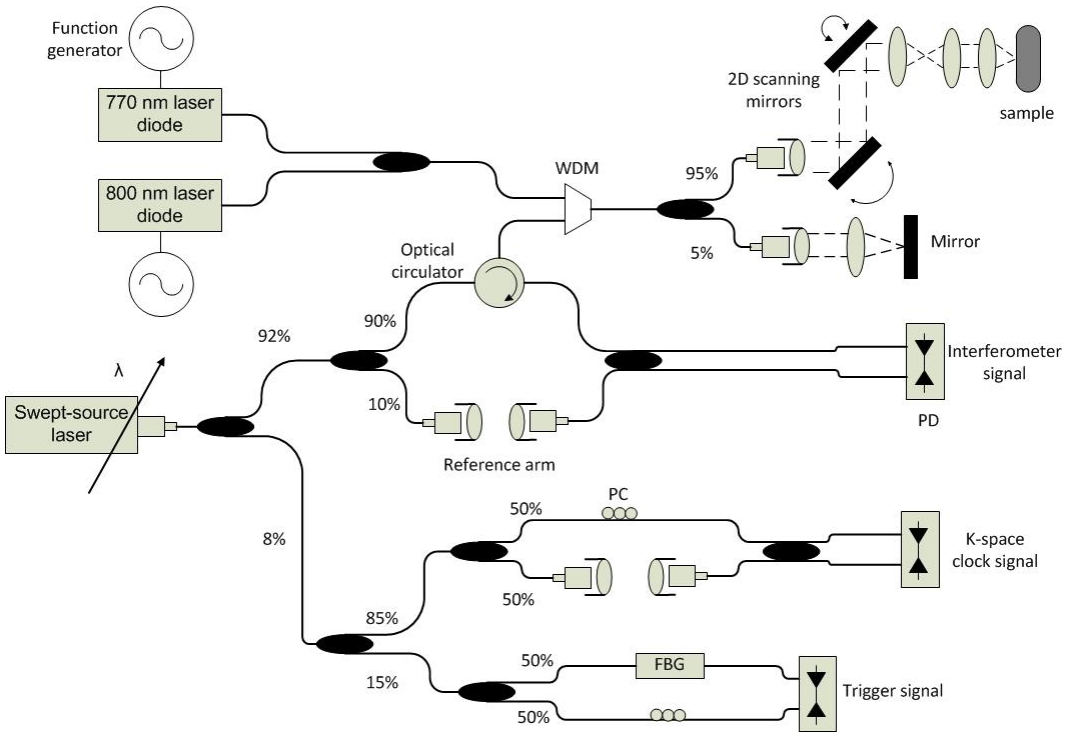

Figure 3.2: DWP-OCT system schematic, WDM: wavelength division multiplexer, FBG: fiber Bragg grating, PC: polarization controller, PD: photodetector.

The phase sensitive OCT system uses a swept source laser (HSL-1000 by Santec Corp. Komaki, Aichi, Japan) with a 28 kHz A-line rate, center wavelength at 1060nm and full-wave-half-maximum spectral width of 58 nm. Single-mode optical fiber (HI1060 by Corning Inc., Corning, NY) is utilized to construct the interferometer. Light emitted by the swept-source laser is split into three subsystems: 1) trigger; 2) sampling clock; and 3) signal interferometer.

The trigger subsystem utilizes a fiber Bragg grating (FBG) to ensure the digitizer starts data acquisition at a consistent and repeatable wavenumber for each A-scan. The sampling clock subsystem consists of a Mach-Zehnder interferometer with clock rate set by adjusting the interferometric light delay. The sampling clock signal received by a balanced photodetector is input into an external analog circuit, frequency quadrupled; and

used as a sampling trigger for the analog-to-digital converter (38). The third subsystem is the Michelson signal interferometer with sample and reference arms. An optical circulator (1060 PI TGG by Agiltron Inc. Woburn, MA) is used in the sample arm of the Michelson interferometer to increase SNR (97). The sample arm contains two light paths: 1) a path to the phantom blood vessel with an achromatic scanning system consisting of two galvanometers and an afocal telescope; 2) a high-reflectivity mirror used for phase stabilization. The achromatic scanning system is designed and simulated in optical design software (Zemax by Radiant Zemax, LLC Redmond, WA) and provides micrometer-scale lateral resolution and imaging three co-aligned beams; the computed diffraction encircled energy computation gives a 13 μm lateral resolution for 770 nm and 800nm excitation beams, and 14 μm for the 1060 nm PhS-OCT probe beam.

After acquisition of the interference fringe signal uniformly in wavenumber (or optical frequency), computing a fast Fourier transform (FFT) of the signal, we obtain a complex number data array for each A-scan; complex number amplitude is used to construct an OCT intensity image, and complex number angle is used to determine phase of the depth-resolved fringe signal. Signal phase of light reflecting from the mirror in the sample path is utilized to correct for any error introduced by delay in data acquisition. Phase errors at any sample depth (d_s) are eliminated by subtracting the reference phase scaled by depth from the sample phase as in Eq. 3.1 (98):

$$\varphi_{sc} = \varphi_s - \frac{d_s}{d_r}\varphi_r \tag{3.1}$$

Where φ_{sc} is corrected sample phase, φ_s is sample phase acquired from the raw signal FFT, φ_r is reference phase obtained from interference between light reflected from the mirror in the sample path and reference arm, and d_s and d_r are sample and reference depths respectively.

The system operates in real-time in either OCT intensity imaging or M-mode phase imaging. Data acquisition and signal processing software are written in Labview (National Instrument Corp. Austin, TX). System sensitivity is 102 dB (shot-noise limited sensitivity is 107 dB), and axial resolution is 13 μm in tissue with application of a real-time digital dispersion compensation algorithm (99-100). The axial resolution is limited by polarization mode dispersion in the circulator. After Fourier transform of M-mode phase data (i.e. one second duration), with a calibration process, phase of light backscattered from a selected sample depth is converted to optical pathlength ($op=\lambda*\varphi_{sc}/2\pi$, where λ is center wavelength and φ_{sc} is corrected sample phase). Mean noise level in the signal frequency region corresponding to intensity modulation of photothermal excitation light (360-420 Hz) is taken as the *op* signal noise floor and measured at 300 pm.

Photothermal excitation beams are emitted from two 100mW single-mode fiber (HI780 by Corning Inc. Corning, NY) pigtailed laser diodes (QFLD-780-100S by QPhotonics, LLC, Ann Arbor, MI for 770 nm and QFLD-795-100S for 800 nm), light from these sources are coupled into the DWP-OCT system's sample arm through a wavelength division multiplexer (WDM) (PSK-000851 by Gould Fiber Optics, Millersville, MD). Both the WDM and PhS-OCT system are constructed using HI1060 corning fiber which is single-mode for 1060 nm probe light and allows two or three propagation modes at photothermal excitation wavelengths of 770 nm and 800 nm. Temperature of each laser diode is precisely controlled within a fraction of a degree (K) and selected to ensure emission at the desired wavelength as calibrated using a spectrometer. Photothermal excitation power incident on the sample for 800nm and 770nm wavelengths is 2.78 mW and 2.87 mW, respectively, both within ANSI limits for skin. Intensity modulation frequencies for photothermal excitation light [770 nm (400

Hz) and 800 nm (380 Hz)] are selected in a signal frequency range where phase noise is low (0.3 nm) and optical pathlength (*op*) signal amplitude is high. Procedure to determine the optimum photothermal excitation frequency to maximize *op* signal-to-noise ratio for blood was reported previously (95). OCT probe (1064 nm) and photothermal excitation (770 nm and 800 nm) beams are co-aligned and coincident on the sample.

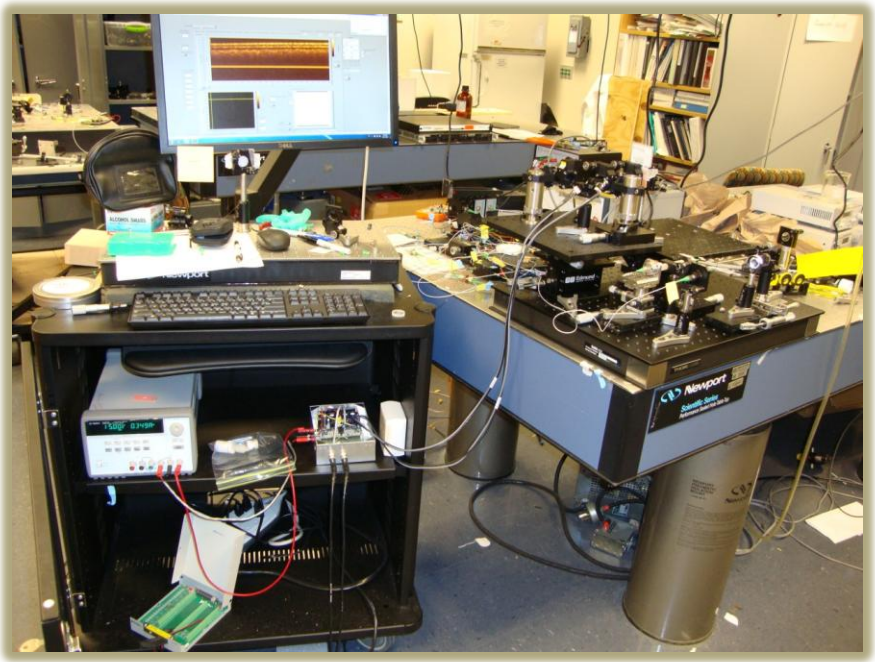

Figure 3.3: A digital picture of DWP-OCT system.

3.3 Blood Oxygen Saturation Calculation

We assume that *op* signal amplitude due to absorption by blood is linear with fluence of photothermal excitation light, neglecting the effect of thermal diffusion (Eq. 3.2). Where τ is photothermal excitation period, I is the average intensity of excitation

light, μ is absorption coefficient, subscripts 1 and 2 correspond to 770 nm and 800 nm wavelength of excitation light respectively.

$$op_{1(2)} \propto \tau_{1(2)} I_{1(2)} (1 - e^{-\mu_{1(2)} l}) \approx \tau_{1(2)} I_{1(2)} \mu_{1(2)} l \tag{3.2}$$

Fluence over one period Φ and absorption coefficient μ can be written as

$$\begin{aligned} \phi_{1(2)} &= \tau_{1(2)} I_{1(2)} \\ \mu_{1(2)} &= \alpha_{d1(2)} c_d + \alpha_{o1(2)} c_o \end{aligned} \tag{3.3}$$

Where α_o and α_d are tabulated molar extinction coefficients of oxygenated and deoxygenated hemoglobin ($cm^{-1}mM^{-1}$).

$$\begin{aligned} \alpha_{o1} &= 0.65 cm^{-1} mM^{-1} \\ \alpha_{o2} &= 0.79 cm^{-1} mM^{-1} \\ \alpha_{d1} &= 1.312 cm^{-1} mM^{-1} \\ \alpha_{d2} &= 0.793 cm^{-1} mM^{-1} \end{aligned} \tag{3.4}$$

c_o and c_d are concentrations of oxygenated and deoxygenated hemoglobin (mM).

Based on the equations above, blood oxygen saturation (SO_2) can be derived as

$$\begin{aligned} SO_2 &= \frac{c_0}{c_0 + c_d} \\ &= \frac{\alpha_{d1} - \chi_{12} \alpha_{d2}}{\chi_{12}(\alpha_{o2} - \alpha_{d2}) - (\alpha_{o1} - \alpha_{d1})} \end{aligned} \tag{3.5}$$

Where

$$\chi_{12} = (op_1 / \Phi_1) / (op_2 / \Phi_2) \tag{3.6}$$

op is measured optical pathlength amplitude. Ratio of the two excitation beams' fluence (Φ_2/Φ_1) at the sample is calibrated before measurement. The *op* signal amplitude at each photothermal excitation wavelength (op_1 and op_2) is determined by computing magnitude of the signal phase oscillation at respective modulation frequencies of excitation light (Fig. 3.4).

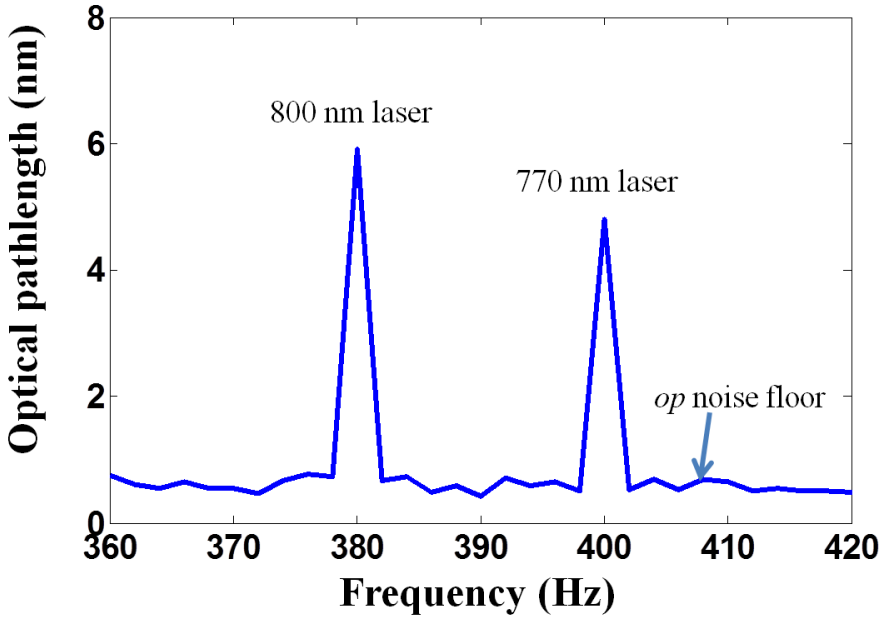

Figure 3.4: Spectra of *op* signal amplitude induced by 770 nm (5 nm, 400 Hz) and 800 nm (6 nm, 380 Hz) excitation light.

3.4 Phantom Vessel Blood Oxygen Saturation Measurement

3.4.1 50-µm inner-diameter phantom vessel experiment

A 50-µm inner diameter polytetrafluoroethylene (PTFE) conduit (SUBL 060 by Braintree scientific, INC, Braintree, MA) containing porcine blood is used as a blood vessel phantom. A desired blood SO_2 level is achieved by adding sodium dithionite to the blood sample to deoxygenate. Six blood samples were prepared at different SO_2 levels (99.6%, 89.2%, 84.1%, 69.0%, 57.3% and 3.0%). To provide a scattering background for imaging, the phantom blood vessel is placed on a sheet of white-colored copy paper. After imaging, blood SO_2 measurements are recorded in an M-mode acquisition at a selected position in the lumen of the phantom vessel (Fig. 3.5).

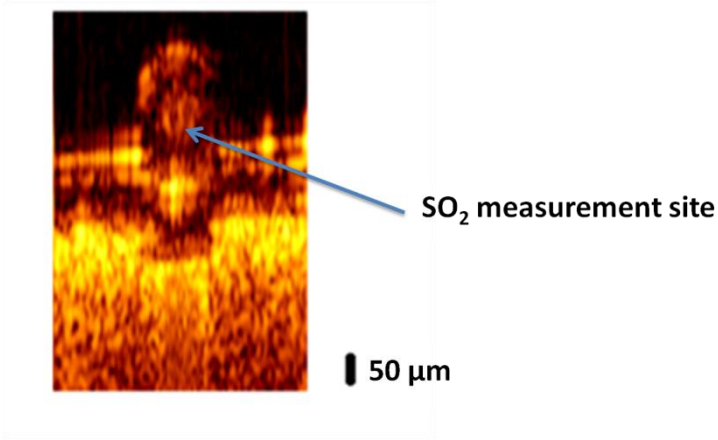

Figure 3.5: B-Scan image of a 50 µm inner-diameter phantom vessel containing blood positioned on a sheet of white-colored copy paper.

We observed *op* signal amplitude in the phantom vessel containing blood resulting from photothermal excitation with 770 nm and 800 nm light. In a control experiment, with the phantom vessel containing water, no *op* signal was detected in response to photothermal excitation.

A two-vessel phantom was constructed to demonstrate DWP-OCT imaging of an arterial-venous vessel pair. Two 50 µm inner-diameter phantom vessels are attached to a sheet of white-colored copy paper to provide a scattering background for imaging. The two phantom vessels are filled with porcine blood, and digital syringe pumps are used to introduce flow (2.8 mm/s) in opposite directions in each phantom vessel (Fig. 3.6), average flow speed is calculated by dividing the syringe pump infusion flow rate (0, 20, 40, 60, 80, 100 and 120 µL/hour) by the phantom vessel's lumen cross-sectional area (1.96×10^3 μm^2).

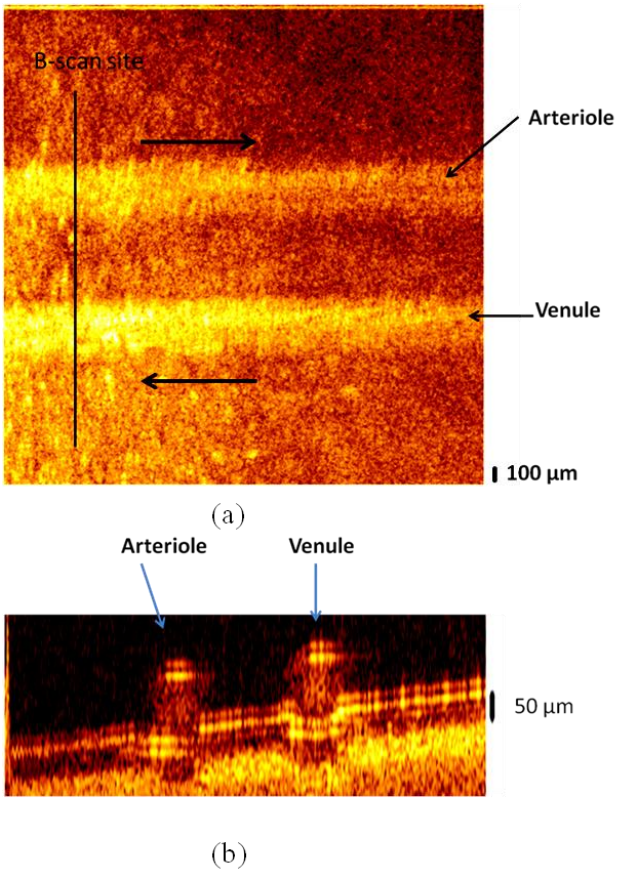

Figure 3.6: (a) En-face image of an arterial-venous phantom vessel pair; (b) B-scan image at the indicated site. Arrows in (a) indicate blood flow direction.

DWP-OCT phase data was recorded over a time period of one-second at the bottom of the lumen in one of the phantom vessels (Fig. 3.5). Optical pathlength (*op*) signal amplitude was determined for each 0.5 second data acquisition period by computing the fast Fourier transform (FFT) of phase (φ_{sc}) data. For each one-second of acquired DWP-OCT data, 15 sub-segments were analyzed with a 1/28 second offset between successive 0.5 second data segments. For each 0.5 second data segment, *op* signal amplitudes at 380 Hz and 400 Hz were calculated, and SO_2 level was estimated according to Eq. 3.5. In the experiment, DWP-OCT data segments longer than 1 second were not recorded due to phase drift. Estimates of *op* were obtained using a moving

window average approach which is preferred for short signal durations to reduce high frequency noise. Phase noise in the *op* signal amplitude increases variance in computed SO_2 levels (see error propagation model in section 3.5). Mean of SO_2 values derived from 15 sub-segments' gives a better estimate and a moving window smoothes time variation of oxygen saturation. Averaging SO_2 values over the sub-segments suppresses phase noise in the *op* signal amplitude.

To demonstrate DWP-OCT for blood SO_2 measurement, the six blood samples prepared at different SO_2 levels were measured (99.6%, 89.2%, 84.1%, 69.0%, 57.3% and 3.0%) with a commercial blood oximeter (AVOXimeter 1000E by International Technidyne Corp. Edison, NJ); each blood sample is separated into two volumes to ensure DWP-OCT and oximeter measurements can be carried out simultaneously, thus reducing measurement variation due to differences in reoxygenation. DWP-OCT measurement time of a single blood sample was shorter than 30 minutes to minimize effect of drift in the blood SO_2 levels (blood sample is deoxygenated by sodium Dithionite) (101). DWP-OCT SO_2 measurement results of blood samples are shown in Fig. 3.7. Each plot indicates SO_2 level deduced from Eq. 3.5 and derived from the fifteen 0.5 second segments'. The solid line (green) and dashed lines (red and blue) represent mean and standard deviation of fifteen segments' DWP-OCT SO_2 values. SO_2 levels measured by a commercial oximeter are indicated in the right portion of each plot.

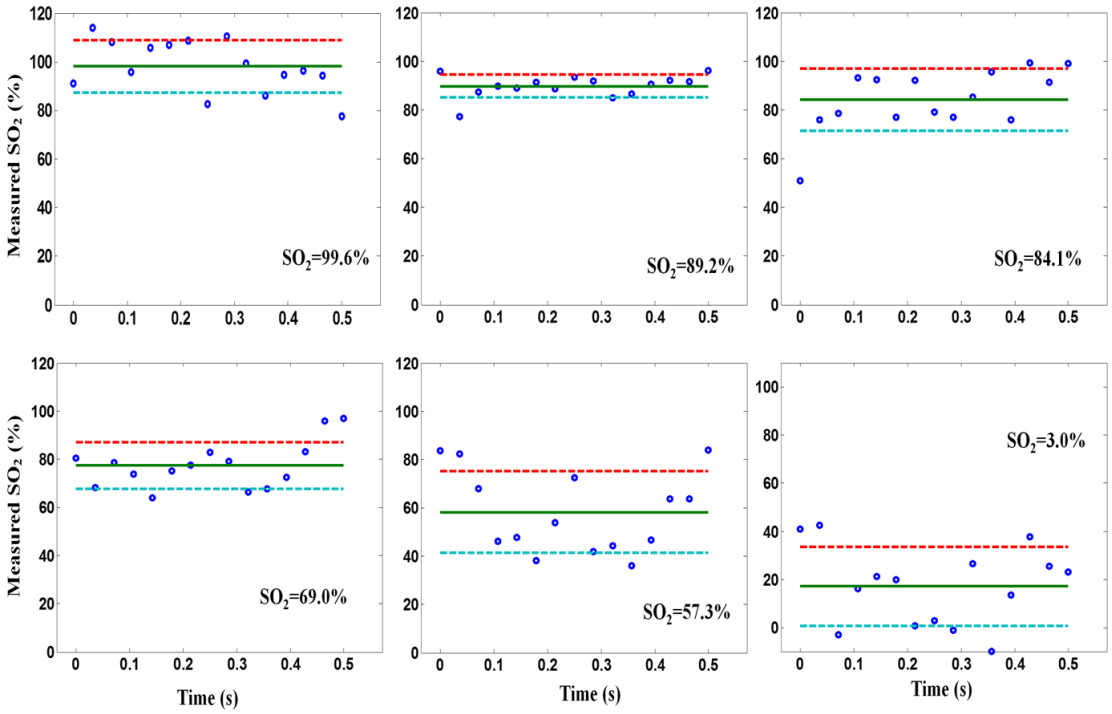

Figure 3.7: Blood SO_2 levels measured in 50-μm inner-diameter phantom vessels by DWP-OCT. Solid line (green) represents mean of fifteen 0.5 second segments and dashed lines (red and blue) represent standard deviation. SO_2 level measured by a commercial oximeter are indicated in the right portion of each plot. Blood is stationary for all measurements.

The six blood samples' SO_2 levels cover a substantially wider range than physiological variation (from 70% (veins) to 97-99% (arteries)). For each measured level, oximeter SO_2 measurement results are within experimental error (approximately ±10%) of DWP-OCT measurement values (Fig. 3.8). The AVOXimeter 1000E features a specified accuracy of ±1% and precision of ±0.5% for blood SO_2 measurements.

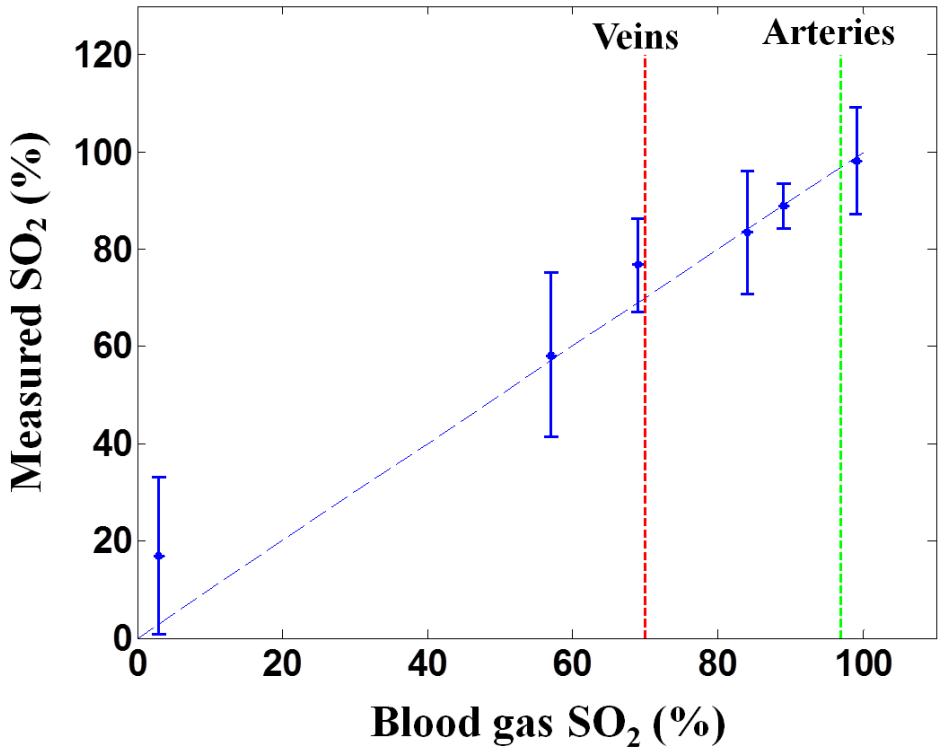

Figure 3.8: Blood SO_2 levels in 50-μm inner-diameter phantom vessel measured by DWP-OCT (vertical) vs. oximeter values (horizontal). Blood is stationary for all measurements.

3.4.2 300-μm inner-diameter phantom vessel experiment

Another microvessel phantom is constructed using a 300 μm inner diameter polytetrafluoroethylene (PTFE) conduit (SUBL 060 by Braintree scientific, INC, Braintree, MA). Six porcine blood samples at different SO_2 levels (99%, 96%, 85%, 75%, 38%and 19%) are prepared for imaging. En-face (Fig. 3.9a) and B-scan (Fig. 3.9b) images were recorded of a phantom microvessel in contact with a sheet of white-colored copy paper. Due to limited penetration depth of 1060 nm probe light in blood, the SO_2 measurement is taken at a side position of the lumen as indicated in Fig. 3.9b.

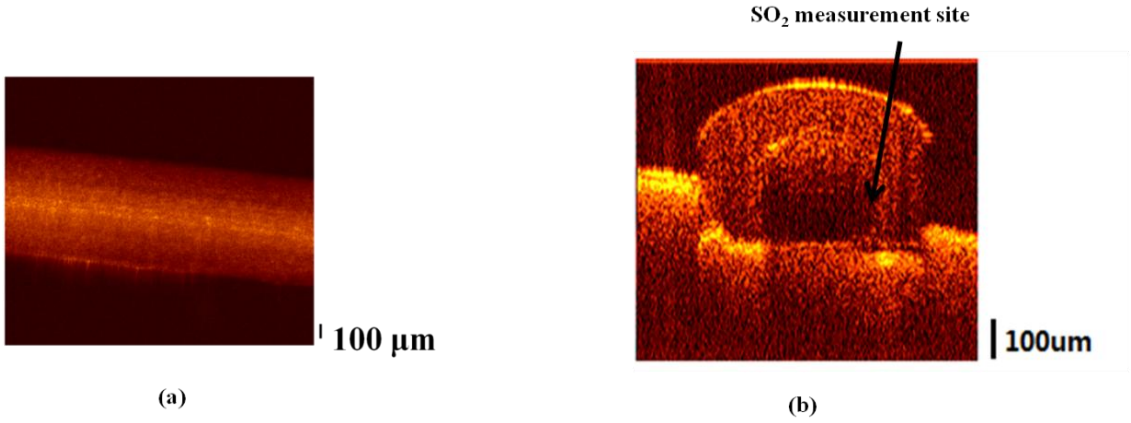

Figure 3.9: (a) En-face image of a phantom microvessel constructed from a polytetrafluoroethylene (PTFE) conduit with inner (300 µm) and outer (630 µm) diameter; (b) B-scan image of a 300 µm inner diameter phantom microvessel containing porcine blood, the arrow indicates SO_2 measurement site at a side position in the lumen.

Similar to the 50-µm inner-diameter phantom vessel experiment, blood SO_2 levels are measured by both DWP-OCT and commercial oximeter; the measurement results are shown in Fig. 3.10 and Fig. 3.11. Except the measurement result for the blood sample with 19% SO_2 level, DWP-OCT measurement results for other five blood samples match well with commercial oximeter measurement values, the means of the measurement deviate less than 5% from the actual blood SO_2 value.

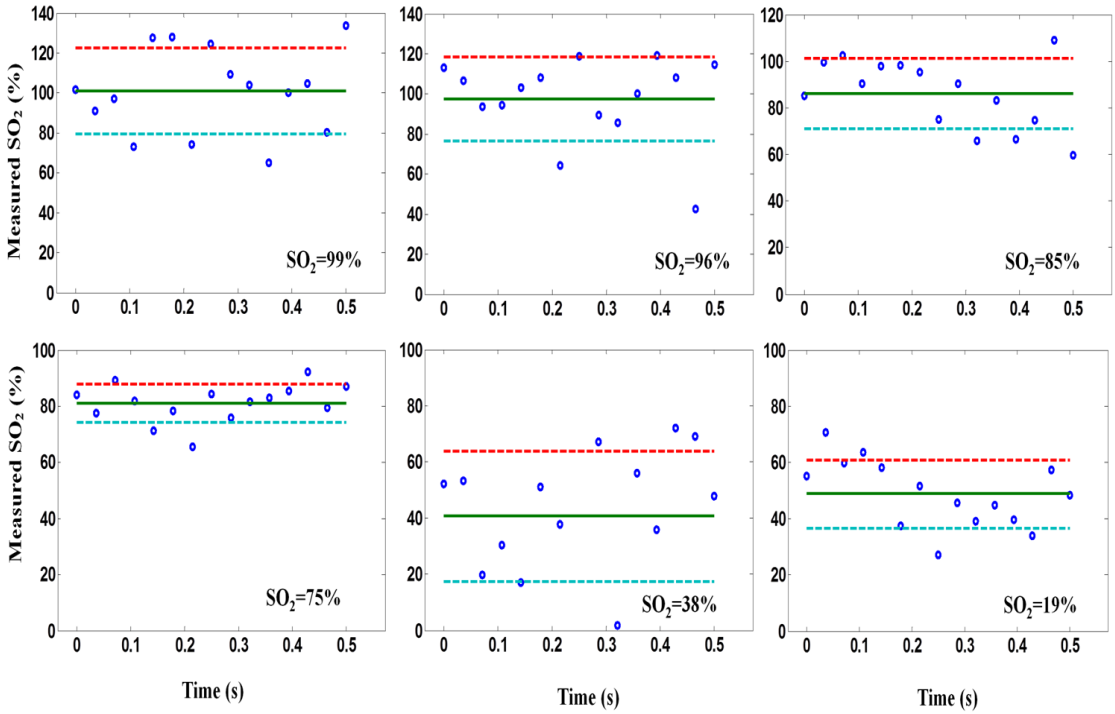

Figure 3.10: Blood SO_2 levels measured in 300-μm inner-diameter phantom vessel by DWP-OCT. Solid line (green) represents mean of fifteen 0.5 second segments and dashed lines (red and blue) represent standard deviation. SO_2 level measured by a commercial oximeter are indicated in the right portion of each plot. Blood is stationary for all measurements.

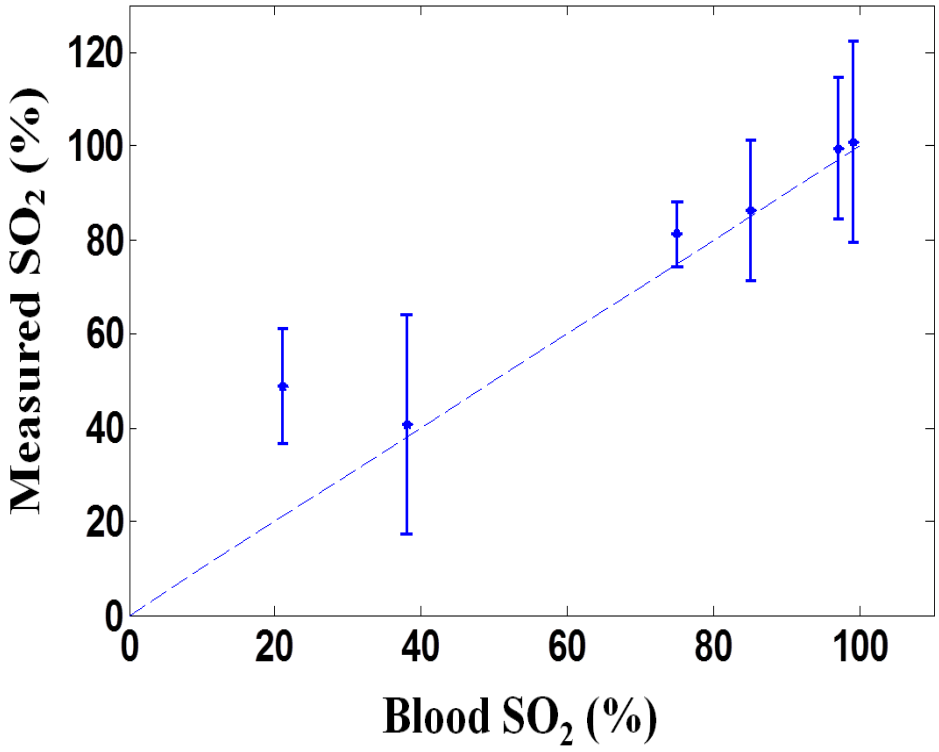

Figure 3.11: Blood SO_2 levels in 300-μm inner-diameter phantom vessel measured by DWP-OCT (vertical) vs. oximeter values (horizontal). Blood is stationary for all measurements.

3.5 DWP-OCT Propagation of Error and Uncertainty Analysis

From Eq. 3.5, we find relative uncertainty in DWP-OCT blood SO_2 values can be written as:

$$\frac{\delta SO_2}{SO_2} = \frac{(\alpha_{d2}\alpha_{o1} - \alpha_{d1}\alpha_{o2})(\delta\chi_{12} / \chi_{12})}{[\chi_{12}(\alpha_{o2} - \alpha_{d2}) - (\alpha_{o1} - \alpha_{d1})](\alpha_{d1} / \chi_{12} - \alpha_{d2})} \tag{3.7}$$

Variation in χ_{12} ($\delta\chi_{12}/\chi_{12}$ Eq. 3.8) can originate from phase variation in optical pathlength (op_1 or op_2) or fluence (Φ_1 or Φ_2) of photothermal excitation beams.

$$(\frac{\delta\chi_{12}}{\chi_{12}})^2 \approx (\frac{\delta op_1}{op_1})^2 + (\frac{\delta op_2}{op_2})^2 + (\frac{\delta\Phi_1}{\Phi_1})^2 + (\frac{\delta\Phi_2}{\Phi_2})^2 \tag{3.8}$$

We define *op* signal-to-noise ratio (SNR, Eq. 3.9) where *op* is optical pathlength signal amplitude in response to photothermal excitation (380 Hz or 400 Hz), δop corresponds to the optical pathlength variation due to either the DWP-OCT system or relative motion between the DWP-OCT source beams (PhS-OCT probe beam and photothermal excitation beams) and sample constituents.

$$SNR(dB) = 10\log(\frac{op}{\delta op}) \tag{3.9}$$

In phantom vessel static blood SO_2 measurement, low-power (~2.8 mW) photothermal excitation light gives *op* amplitudes of 2-5 nm, and a 0.3 nm uncertainty in *op* amplitude gives a relative uncertainty $\delta op/op$ = 6%-15% (*op* SNR 8.2-12.2 dB), while laser power fluctuation can introduce a 2% uncertainty in $\delta\Phi/\Phi$. Based on Eqs. 3.7 and 3.8, effect of *op* SNR on relative blood SO_2 measurement error ($\delta SO_2/SO_2$) is estimated (Fig. 3.12). Relative uncertainty in χ_{12} decreases with increasing *op* SNR (Fig. 3.12a). Relative uncertainty in DWP-OCT blood SO_2 increases with decreased SO_2 values (Fig. 3.12b). At any blood SO_2 level, $\delta SO_2/SO_2$ increases with increasing relative uncertainty in χ_{12}. Each of the six measured blood samples' relative SO_2 measurement error in a single (0.5 s) segment are deduced and plotted (Fig. 3.12b), and have values close to curves corresponding to 20% and 30% relative uncertainty in χ_{12}.

To reduce DWP-OCT's relative blood SO_2 measurement error to within 5% (SO_2 above 60%), relative uncertainty in χ_{12} must be less than 5%, requiring an *op* SNR above 15 dB ($\delta op/op$ below 3%). A substantial increase in DWP-OCT SO_2 measurement errors observed in 57.3% and 3% SO_2 blood levels are consistent with computed values (Fig. 3.12b). As the *op* is obtained from the phase measurement, to increase DWP-OCT blood SO_2 measurement accuracy and reliability, system phase stabilization is critical.

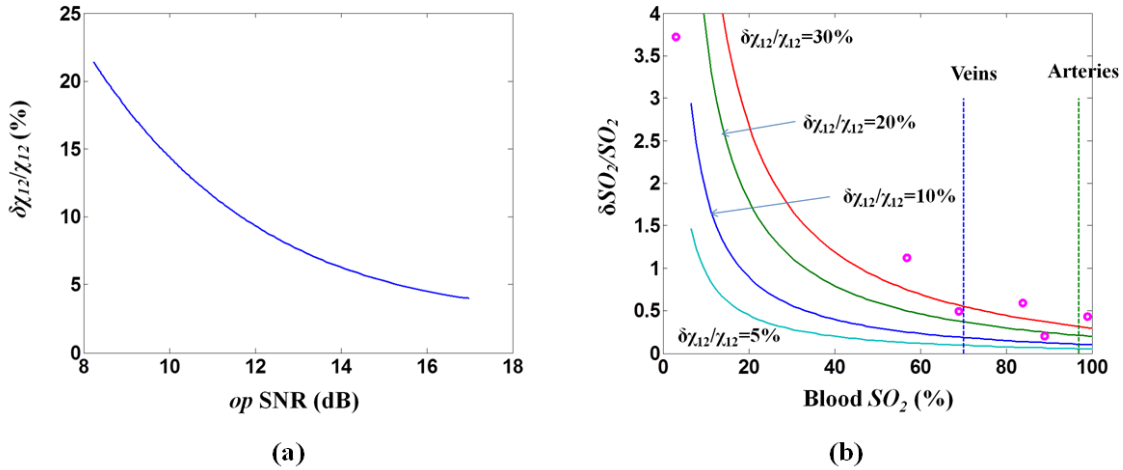

Figure 3.12: (a) Relative χ_{12} error ($\delta\chi_{12}/\chi_{12}$) vs. *op* SNR. (b) Relative blood SO_2 measurement error ($\delta SO_2/SO_2$) vs. SO_2 for various levels of relative χ_{12} error. Horizontal axis: blood SO_2 level; vertical axis: relative error of SO_2. Solid curves represent conditions when relative variation of χ_{12} is 5%, 10%, 20%, and 30%; blue dashed line: SO_2 of veins (70%); green dashed line: SO_2 of arteries (97%); magenta circles: relative blood SO_2 measurement error in six blood samples.

3.6 Influence of Blood Flow on DWP-OCT SO_2 Measurement

To investigate effect of blood flow on SO_2 measured by DWP-OCT, a digital syringe pump (AL-1000 by World Precision Instruments, Sarasota, FL) is used to introduce blood flow in the phantom vessel at a fixed SO_2 level (98.2%) corresponding to an arteriole. At the fixed SO_2 level, DWP-OCT SO_2 measurements are recorded at blood flow speeds from 0-17 mm/s. For each blood flow speed, SO_2 levels are also measured at the same position in the lumen of the phantom vessel. At increasing blood flow speeds, *op* signal amplitude induced by blood absorption of each photothermal excitation beam is reduced (Fig. 3.13a). A substantial reduction (80%) in *op* signal amplitude is observed at greatest average blood flow speed (17 mm/s).

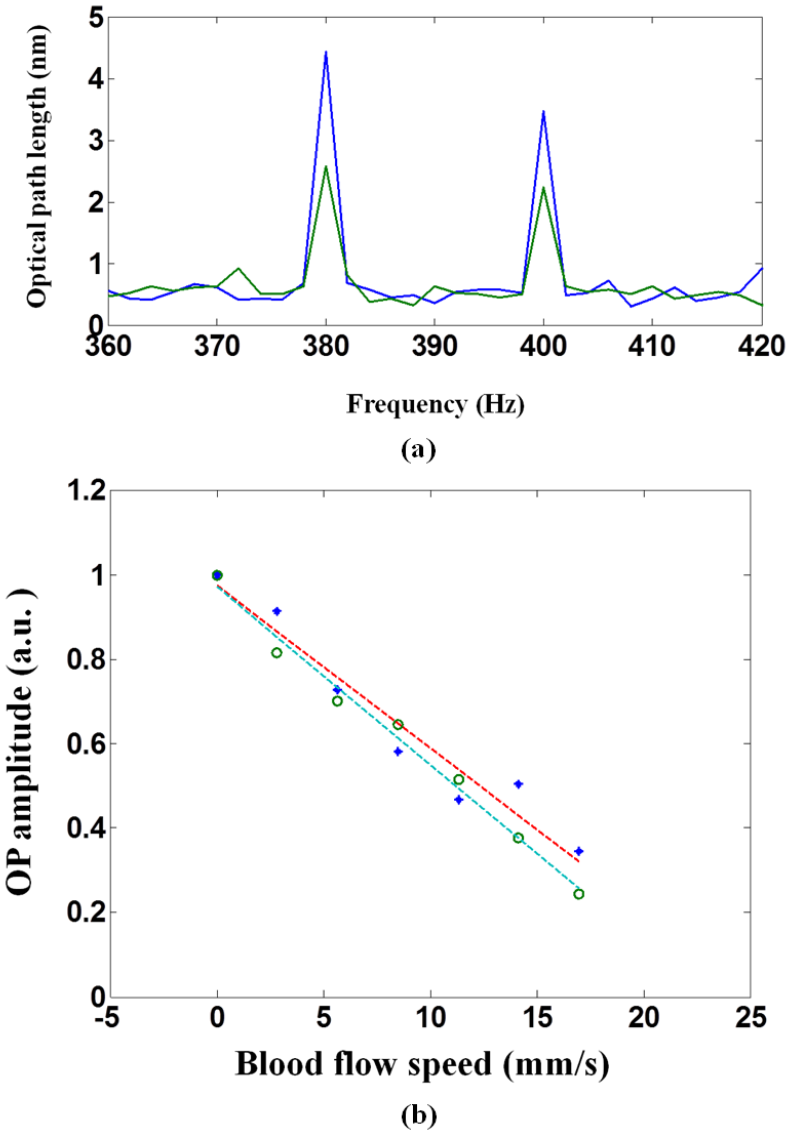

Figure 3.13: (a) Reduction in *op* signal amplitude at 800 nm (380 Hz) and 770 nm (400 Hz) from stationary (blue) to increased average blood flow speed (green, 8.5 mm/s) in a 50-μm inner-diameter phantom blood vessel. (b) Normalized *op* signal amplitude vs average blood flow speed. Circle: *op* signal amplitude in response to 770 nm excitation, blue dashed line is linear fit; diamond: *op* signal amplitude in response to 800 nm excitation, red dashed line is linear fit.

DWP-OCT measurements are recorded at average blood flow speeds from stationary to 17 mm/s. *op* signal amplitudes for 770 nm (400 Hz) and 800 nm (380 Hz) light are normalized by respective amplitudes at the stationary condition (Fig. 3.13b).

Accuracy of DWP-OCT SO_2 measurement at various blood flow speeds can be determined by analysis of SNR of the *op* signal in response to laser excitation (Eq. 3.9). SNR degradation with respect to increasing blood flow speed (Fig. 3.14a) suggests that most reliable DWP-OCT SO_2 measurements can be obtained at blood flow speeds up to 13 mm/s.

SO_2 level is calculated for average blood flow speeds up to 17 mm/s (Fig. 3.14b). SO_2 measured by DWP-OCT is within experimental error of values measured by a commercial oximeter for average blood flow speeds less than 13 mm/s. A 13 mm/s average blood flow speed is found in 30-40 μm diameter retinal arterioles (102). Relative blood SO_2 measurement error increases with increasing blood flow speed (Fig. 3.14c). *op* SNR is a critical factor that determines accuracy of measured SO_2 levels (Fig. 3.14b), results suggest that when *op* signal SNR degradation exceeds 10 dB, SO_2 levels measured by DWP-OCT are no longer reliable. Experimental results suggest that a DWP-OCT system utilizing low power (~2.8 mW) photothermal excitation has sufficient stability and sensitivity to measure SO_2 levels in a 50-μm inner-diameter stationary blood vessel phantom with average blood flow speeds from stationary up to 13 mm/s.

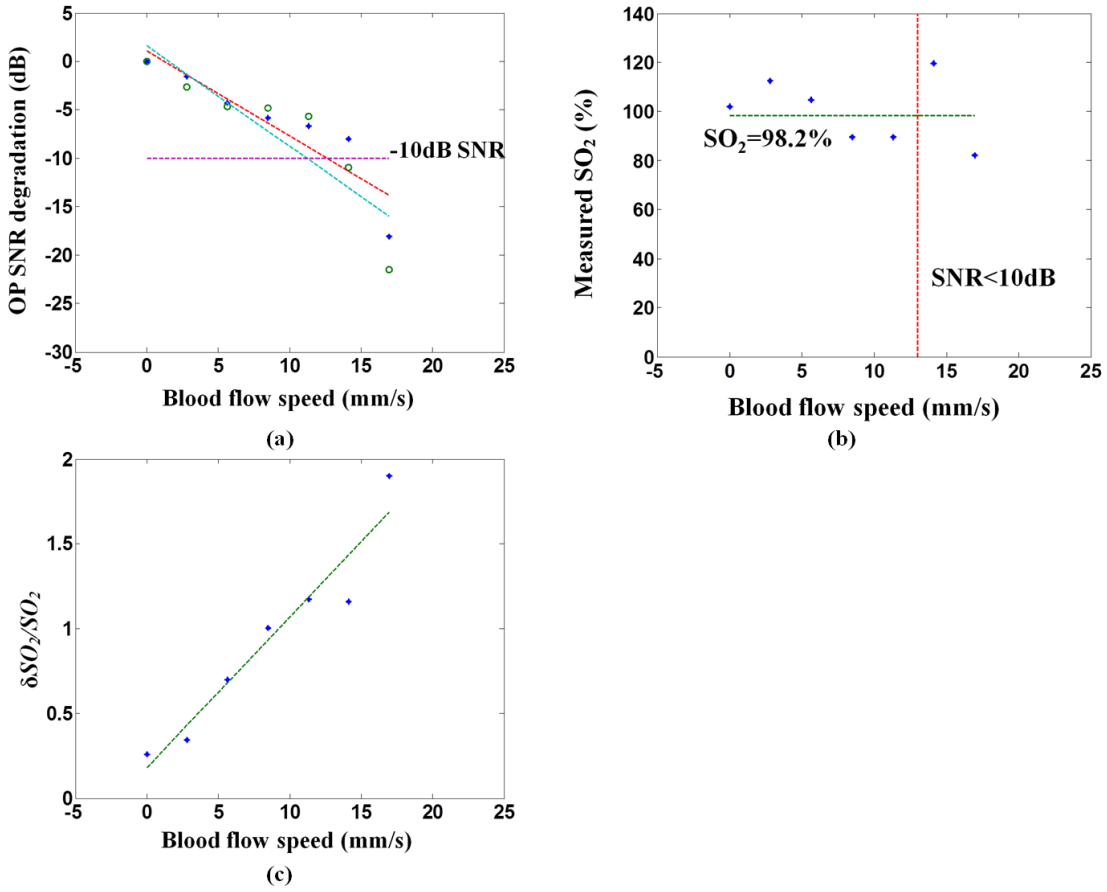

Figure 3.14: (a) SNR degradation vs. blood flow speed. Circle: SNR in response to 770 nm excitation, blue dashed line is linear fit; diamond: SNR in response to 800nm excitation, red dashed line is linear fit; purple dashed line is 10 dB SNR *op* degradation. (b) SO_2 measurement in blood vessel phantom at various blood flow speeds. Diamond: SO_2 measured by DWP-OCT; green dashed line: SO_2 measured by oximeter (98.2%); red dashed line: threshold speed above which SNR degradation exceeds 10 dB. (c) Relative blood SO_2 measurement error ($\delta SO_2/SO_2$) for one single segment (0.5 s) vs. blood flow speed. Green dashed line is linear fit.

Brownian motion and blood flow can also contribute to an increased *op* signal noise floor; in the blood flow experiments reported here, difference in refractive indices between red blood cells (RBC) and blood plasma is one source which increases *op* signal

noise. Time dependent optical pathlength ($op(t)$) of the probe beam traveling through the phantom vessel lumen can be expressed as:

$$op(t) = n_{RBC} l_{RBC}(t) + n_{plasma} l_{plasma}(t) \tag{3.10}$$

Where n_{RBC} and n_{plasma} are the group refractive indices of red blood cells and plasma, l_{RBC} and l_{plasma} are the physical pathlengths that probe beam travels through RBC and blood plasma respectively. Values of l_{RBC} and l_{plasma} vary randomly due to blood flow; a higher blood flow speed will cause *op* signal amplitude to change more rapidly as indicated in Eq. 3.10, which results in an increased *op* signal noise floor between successive A-scans. In case of stationary blood, Brownian RBC motion contributes to *op* signal noise. For the 50-μm inner-diameter phantom blood vessel tested here, effect of Brownian RBC motion on *op* signal noise is approximately equivalent to the increase associated with a 6 mm/s blood flow speed relative to the stationary state (103). An increased *op* signal noise floor is observed in a larger diameter vessel (300 μm inner-diameter) due to a longer physical pathlength. SO_2 measurement has also been recorded in a 300 μm diameter phantom blood vessel. At equivalent average blood flow speed (11.8 mm/s), *op* signal noise floor (1.82 nm) in the larger diameter phantom vessel (300 um inner-diameter) is increased by 1.3 nm over that (0.52 nm) in the 50 um inner-diameter phantom vessel.

3.7 Thermal Diffusion Influence on DWP-OCT SO_2 Measurement

Because Eq. 3.5 does not include effects of thermal diffusion, we constructed a mathematical model to investigate the impact of heat flow on measured DWP-OCT SO_2 values. The model uses the Green's function solution of the bioheat equation in a semi-infinite medium (104), and assumes negligible radiative and/or convective thermal energy losses. We assume an insulating boundary condition and a circular microvessel

lumen and derive an algebraic expression for the temperature increase (ΔT) in the tissue at lateral position r and depth z in response to two photothermal excitation beams at time t.

$$
\begin{aligned}
&\Delta T(r,z,t) = \Delta T_1(r,z,t) + \Delta T_2(r,z,t) \\
&\Delta T_i(r,z,t) = T_{0,i} \cdot K_{r,i} \cdot K_{z,i} \\
&T_{0,i} = \mu_i \Phi_i / \rho c \\
&K_{r,i} = \frac{r_{ph,i}^{\ 2}}{4\alpha t + r_{ph,i}^{\ 2}} e^{-\frac{r^2}{4\alpha t + r_{ph,i}^{\ 2}}} \\
&K_{z,i} = \frac{e^{\alpha t \mu_i^{\ 2} + \mu_i z_a}}{2} \{ e^{-\mu_i z} [erfc(\frac{z_a - z + 2\alpha t \mu_i}{2\sqrt{\alpha t}}) - erfc(\frac{z_b - z + 2\alpha t \mu_i}{2\sqrt{\alpha t}})] + \\
&e^{\mu_i z} [erfc(\frac{z_a + z + 2\alpha t \mu_i}{2\sqrt{\alpha t}}) - erfc(\frac{z_b + z + 2\alpha t \mu_i}{2\sqrt{\alpha t}})] \}
\end{aligned}
\tag{3.11}
$$

In Eq. 3.11, subscript i denotes excitation wavelength (*1* for 770 nm, *2* for 800 nm), μ_i is blood absorption coefficient at the ith wavelength of the photothermal excitation, Φ_i is fluence over one period of photothermal excitation at the ith wavelength, ρc is the product of density and specific heat capacity, α is the thermal diffusivity of tissue; z_a, z_b are depths of the upper (z_a) and lower (z_b) boundary of the source layer; r_{pr} and $r_{ph,i}$ are the radii of OCT probe beam and photothermal excitation beam at the ith wavelength. $K_{r,i}$ and $K_{z,i}$ are two functions which represent heat diffusion along lateral and longitudinal axes respectively in response to excitation at the ith wavelength. $K_{r,i}$ and $K_{z,i}$ are derived based on the Green's function for the temperature response in a semi-infinite half-space. $K_{r,i}$ is derived by convolving the Green's function for lateral diffusion with the photothermal excitation beam, and can be weighted by the OCT probe beam's field intensity distribution (Gaussian distribution) to calculate average *op* detected by OCT; $K_{z,i}$ is obtained by integrating the Green's function along longitudinal axis with an exponential decaying (Beer's law) source profile between upper (z_a) and lower (z_b)

boundaries. The optical pathlength (*op*) in response to photothermal excitation is calculated from the temperature increase as in Eq. 3.12.

$$op(r, z_0, t) = \int_0^{z_0} \Delta T(r, z, t)[\frac{dn}{dT} + \beta \times n(T)]dz$$
$$\beta = \frac{dl}{ldT} \tag{3.12}$$

Where z_0 is the DWP-OCT probe depth position, dn/dT is refractive index change in response to a temperature increase, β is linear thermal expansion coefficient, and $n(T)$ is refractive index of tissue with temperature dependence. With low-power photothermal excitation such as used in experiments reported here, we assume that dn/dT, β and n are constant within the temperature range, so Eq. 3.12 can be simplified.

$$op(r, z_0, t) = [\frac{dn}{dT} + \beta \times n(T_{in})]\int_0^{z_0} \Delta T(r, z, t)dz \tag{3.13}$$

T_{in} is the initial temperature; Eq. (3.13) shows that *op* signal is proportional to the accumulated temperature increase along the tissue depth up to the probe depth (z_0). According to the analytical expression for the temperature increase (Eq. 3.11), we can simulate the *op* signal in response to 770 nm and 800 nm photothermal excitation beams incident on the microvessel phantom.

We assume a blood sample with SO_2 level 90%, two photothermal excitation beams are intensity modulated at 400 Hz (770 nm) and 380 Hz (800 nm) and incident on the vessel, measurement site is 10 um below the top of lumen (Fig. 3.15).

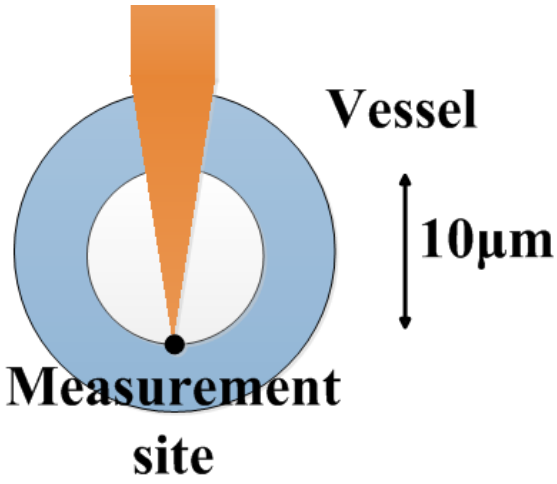

Figure 3.15: A vessel model.

Assume OCT A-scan rate is 30 kHz. Photothermal excitation lasers are turned on at time t=0, the *op* variation in response to two photothermal excitation wavelengths during 0.1 s are presented in Fig. 3.16a, power spectrum of the *op* signal is obtained (Fig. 3.16b). Calculated ratio of *op* signal amplitudes at the two excitation frequencies and calculation of the ratio (χ), the SO_2 level is estimated at 93.4%; the difference indicates a systematic error due to thermal diffusion may be present in the model equation (Eq. 3.5) to deduce SO_2 level.

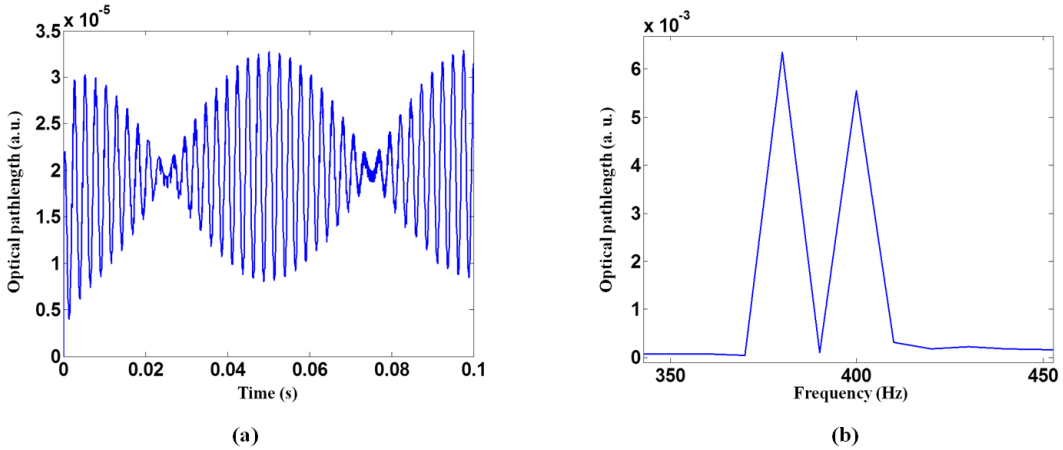

Figure 3.16: (a) Simulated *op* variation in a blood sample with 90% SO_2 level during 0.1 s, two photothermal excitation beams (770 nm and 800 nm) are incident on the sample, the investigated depth is 10 um below the top of lumen; (b) Power spectrum of *op*, 400 Hz frequency component corresponds to 770 nm wavelength excitation and 380 Hz frequency component corresponds to 800 nm wavelength excitation.

Similarly, we simulate six blood samples' optical pathlength (*op*) signals in response to the two photothermal excitation wavelengths (770 nm and 800 nm) with the SO_2 levels equal to oximeter values measured in the 300-μm inner-diameter phantom vessel experiment. Actual (assumed in model) blood SO_2 levels and SO_2 levels predicted by Eq. 3.5 are compared in Fig. 3.17. Six blood samples' SO_2 level predicted by DWP-OCT are over-estimated by an average of 3.57%. Though the systematic error is found to compromise the model (Eq. 3.5) for DWP-OCT measurement of SO_2, magnitude of the error for each case is relatively small but evident at all blood oxygenation levels. Examining Fig. 3.17, a systematic error that suggests DWP-OCT may over-estimate blood oxygenation levels is evident (over-estimate by 2-6% for each blood sample in the experiment). Results of the mathematical model suggest the systematic error observed in blood microvessel phantom data may be due at least in part to thermal diffusion that is not accounted for in the model (Eq. 3.5).

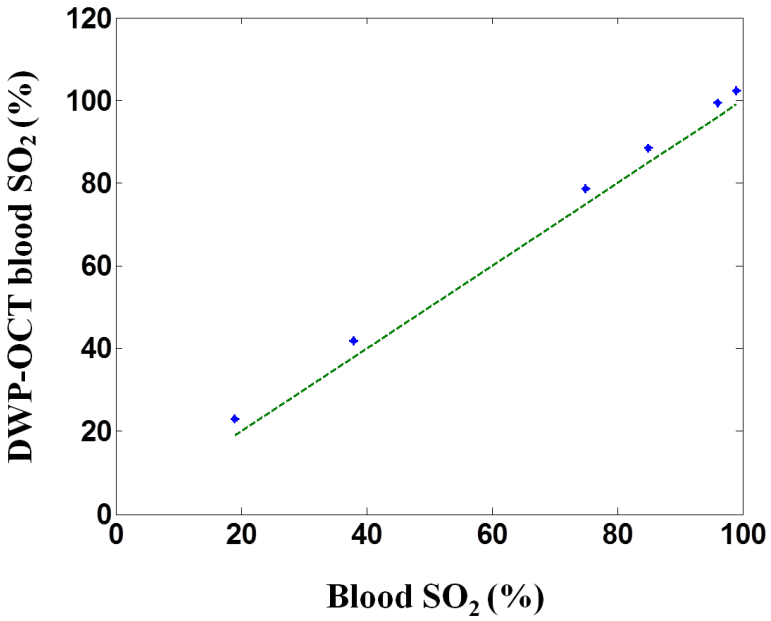

Figure 3.17: DWP-OCT blood SO_2 level predicted by Eq. 3.5 and simulated optical pathlength (*op*) signal (Eq. 3.13) vs. assumed blood SO_2. Stars correspond to six blood samples with SO_2 level matching that of the samples in 300-μm inner-diameter phantom vessel experiment. Green dashed line represents where DWP-OCT blood SO_2 levels equal assumed SO_2 levels.

3.8 CONCLUSION ON DWP-OCT STUDY

In this study, we designed and demonstrated a two-beam DWP-OCT system for measurement of microvasculature hemoglobin oxygen saturation (SO_2) levels and imaging phantom microvessels. For each blood sample, mean of one second's DWP-OCT SO_2 measurement results match commercial oximeter values. Propagation of errors and uncertainty analysis indicates DWP-OCT is feasible for measurement of blood SO_2 levels above 60%. Further stabilization of phase can reduce measurement uncertainty. Influence of blood flow on DWP-OCT SO_2 measurement was investigated by introducing blood flow in phantom microvessel and analyzing *op* signal SNR. Results suggest DWP-

OCT remains stable for average blood flow speed less than 13 mm/s in phantom microvessel. Effect of thermal diffusion on measured DWP-OCT SO_2 values was investigated by utilizing a mathematical model. Predicted DWP-OCT SO_2 levels derived from the simulation suggest that thermal diffusion can introduce a 3% systematic artifact that over-estimates SO_2 values determined from the model and is consistent with measured data.

For *in vivo* measurements, relative motion between the DWP-OCT source beams and the bulk tissue is an additional noise source that degrades *op* SNR. Tissue motion artifacts can be either suppressed by increasing modulation frequency or DWP-OCT A-scan rate. Swept-source laser sweep rates up to 5 MHz have been demonstrated (5). Higher modulation frequency will require photothermal excitation lasers with a greater instantaneous power (corresponding to a shorter excitation period) to maintain fluence at the same level as the system presented here. In studies reported here, incident radiant power (~2.8 mW) is within ANSI limits for skin. For retinal applications, photothermal excitation power must be less than 0.75 mW.

Chapter 4: Spectrally-Encoded High-Extinction Polarization Microscope

4.1 Introduction of Polarized Light Microscopy Study

Polarized light microscopy is an imaging technique to provide molecular structure and orientation based on probe light's polarization state information. Polarized light microscopy has been used for imaging spindle microtubules (105) and visualizing cytoskeletal dynamics (106). Many cellular structures can be detected with high contrast under polarized light including various filament systems (actin, microtubule, intermediate filaments and collagen), membrane boundaries including those of the plasma membrane, cellular vesicles and various organelles and cellular structures which show crystalline-like organization. Contrast in polarized light images arises from changes in phase and amplitude due to differential retardation or attenuation of orthogonally polarized light as it travels through the specimen. As mentioned in Chapter 1 and Chapter 2, intrinsic birefringence and form birefringence exist in cells and tissues; and another type of birefringence that exists in cells is edge birefringence (107), which is observed at the boundary between dielectric interfaces such as between water and cell membranes.

The signals introduced by these cellular sources of birefringence are typically quite small and are easily obscured by background light and optical aberrations. The intensity of the signal also depends on the orientation of the specimen or the polarization state of incident light. To obtain the sample birefringence, modulated polarization microscopy was developed by modulating the polarization state of light illuminating the specimen and then determining the birefringence quantitatively from the changing amplitude.

In this study, an apparatus for a spectrally-encoded high-extinction polarization microscope is proposed. The algorithm is developed to calculate the specimen phase retardation based on Stokes parameter analysis on Poincaré sphere and followed by a system signal-to-noise ratio analysis.

4.2 SPECTRALLY-ENCODED HIGH-EXTINCTION POLARIZATION MICROSCOPE

Proposed design of the polarization microscope (Fig. 4.1) uses a wavelength tunable light source to provide rapidly tunable monochromatic spatially incoherent light at discrete wavelength (λ_i) incident on the sample. After emission from the source, light goes through a collimator, a linear polarizer oriented at 0°, a retarder oriented at 45°, a rotator with rotation angle θ, a condenser, then illuminates the specimen; the transmitted light is collected by an objective, then propagates though a rotator with rotation angle $-\theta$, a retarder oriented at -45° introducing phase retardation equal to the phase retardation introduced by the first retarder, an analyzer oriented at 90°, and then light is imaged by a high-speed CCD camera.

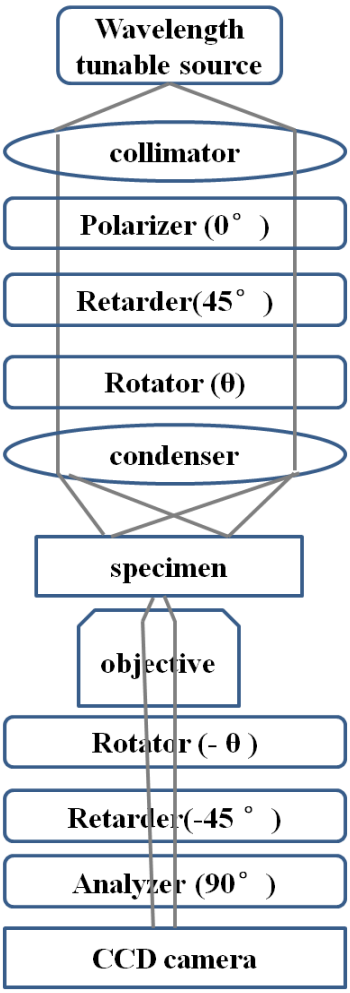

Figure 4.1: Block diagram of polarization microscope.

To calculate the birefringence introduced by a specimen, we adopt a Stokes vector analysis similar to the approach presented in Chapter 2. After the polarizer, linearly polarized light at wavelength (λ_i) is transformed to a pre-calibrated elliptical polarization state after propagation through the first retarder-rotator combination. After the light is transformed by the first retarder-rotator set, the azimuthal and polar angles on Poincaré sphere between the incident light's Stokes vector and specimen's optical axis are (φ_0, θ_0). The specimen introduces a rotation of incident light's Stokes vector around specimen's

optical axis on Poincaré sphere, the rotation angle equals the phase retardation. After transmitted light is collected by an imaging objective lens, the second rotator-retarder combination is used to reverse the transformation introduced by the first retarder-rotator combination. For a null measurement, if assume after the polarizer, the Stokes vector of the light is (1, 1, 0, 0), the intensity detected after analyzer is (1-Q_f)/2 where Q_f is the Q value for the Stokes vector of light before passing through analyzer.

Assume the specimen is with phase retardation δ_i at wavelength λ_i, we have Eq. 4.1, where δ_0 and λ_0 are phase retardation and wavelength at the reference incident wavelength.

$$\delta_i = \delta_0 * \lambda_0 / \lambda_i \tag{4.1}$$

When input light intensity is normalized to 1, the signal S_0 measured after the final polarizer at wavelength λ_0 is written as

$$\begin{aligned} S_0 = \frac{1}{2}(1-Q_f) = \frac{1}{2}(1-\sin^2\theta_0\cos^2\varphi_0 - \sin^2\varphi_0\cos\delta_0 + \\ \cos\theta_0\sin\varphi_0\cos\varphi_0\sin\delta_0 - \cos^2\theta_0\cos^2\varphi_0\cos\delta_0 - \cos\theta_0\sin\varphi_0\cos\varphi_0\sin\delta_0) \end{aligned} \tag{4.2}$$

Since phase retardation of specimen δ_0 is so small, we can use the approximation:

$$\begin{aligned} \cos\delta_0 &= 1-\frac{1}{2}\delta_0^2 \\ \sin\delta_0 &= \delta_0 \end{aligned} \tag{4.3}$$

Eq. 4.2 can be simplified according to Eq. 4.3

$$S_0 = \frac{1}{4}\delta_0^2(\sin^2\theta_0\sin^2\varphi_0 + \cos^2\theta_0) \tag{4.4}$$

At wavelength λ_i, with pre-calibration we assume the specimen introduces $\Delta\varphi_i$ and $\Delta\theta_i$ angle which are the azimuthal and polar angles with respect to the reference wavelength λ_0, and can be used as offset angles. For n spectral measurements (in addition to the reference) the signal may be written:

$$
\begin{aligned}
S_1 &= \frac{1}{4}\left(\frac{\delta_0\lambda_0}{\lambda_1}\right)^2 [\sin^2(\theta_0+\Delta\theta_1)\sin^2(\varphi_0+\Delta\varphi_1)+\cos^2(\theta_0+\Delta\theta_1)] \\
S_2 &= \frac{1}{4}\left(\frac{\delta_0\lambda_0}{\lambda_2}\right)^2 [\sin^2(\theta_0+\Delta\theta_2)\sin^2(\varphi_0+\Delta\varphi_2)+\cos^2(\theta_0+\Delta\theta_2)] \\
&\vdots \\
S_n &= \frac{1}{4}\left(\frac{\delta_0\lambda_0}{\lambda_n}\right)^2 [\sin^2(\theta_0+\Delta\theta_n)\sin^2(\varphi_0+\Delta\varphi_n)+\cos^2(\theta_0+\Delta\theta_n)]
\end{aligned}
\tag{4.5}
$$

For a non-null measurement, the polarizer is slightly mis-aligned from the analyzer by a small angle so that when no specimen is present, a background intensity is present; assume after the polarizer, the Stokes vector of light is (1, sinβcosα, sinβsinα, cosβ), where α and β are the azimuthal and polar angles of the Stokes vector of the incident light. Following a derivation similar to that presented above, the signal detected after the analyzer is written as

$$S_0 = \frac{1}{2}\left\{\begin{array}{l} 1-\sin\beta\cos\alpha+\delta_0[\cos\theta_0\sin\alpha\sin\beta-\sin\theta_0\sin\varphi_0\cos\beta]+ \\ \frac{1}{2}\delta_0^2[\cos\alpha\sin\beta-\sin^2\theta_0\cos\varphi_0\sin\beta\cos(\varphi_0-\alpha)-\sin\theta_0\cos\theta_0\cos\varphi_0\cos\beta] \end{array}\right\}$$

$$S_1 = \frac{1}{2}\left\{\begin{array}{l} 1-\sin\beta\cos\alpha+(\frac{\delta_0\lambda_0}{\lambda_1})[\cos(\theta_0+\Delta\theta_1)\sin\alpha\sin\beta \\ -\sin(\theta_0+\Delta\theta_1)\sin(\varphi_0+\Delta\varphi_1)\cos\beta]+ \\ \frac{1}{2}(\frac{\delta_0\lambda_0}{\lambda_1})^2[\cos\alpha\sin\beta-\sin^2(\theta_0+\Delta\theta_1)\cos(\varphi_0+\Delta\varphi_1)\sin\beta\cos(\varphi_0+\Delta\varphi_1-\alpha) \\ -\sin(\theta_0+\Delta\theta_1)\cos(\theta_0+\Delta\theta_1)\cos(\varphi_0+\Delta\varphi_1)\cos\beta] \end{array}\right\}$$

$$S_2 = \frac{1}{2}\left\{\begin{array}{l} 1-\sin\beta\cos\alpha+(\frac{\delta_0\lambda_0}{\lambda_2})[\cos(\theta_0+\Delta\theta_2)\sin\alpha\sin\beta \\ -\sin(\theta_0+\Delta\theta_2)\sin(\varphi_0+\Delta\varphi_2)\cos\beta]+ \\ \frac{1}{2}(\frac{\delta_0\lambda_0}{\lambda_2})^2[\cos\alpha\sin\beta-\sin^2(\theta_0+\Delta\theta_2)\cos(\varphi_0+\Delta\varphi_2)\sin\beta\cos(\varphi_0+\Delta\varphi_2-\alpha) \\ -\sin(\theta_0+\Delta\theta_2)\cos(\theta_0+\Delta\theta_2)\cos(\varphi_0+\Delta\varphi_2)\cos\beta] \end{array}\right\}$$

$$\vdots$$

$$S_n = \frac{1}{2}\left\{\begin{array}{l} 1-\sin\beta\cos\alpha+(\frac{\delta_0\lambda_0}{\lambda_n})[\cos(\theta_0+\Delta\theta_n)\sin\alpha\sin\beta \\ -\sin(\theta_0+\Delta\theta_n)\sin(\varphi_0+\Delta\varphi_n)\cos\beta]+ \\ \frac{1}{2}(\frac{\delta_0\lambda_0}{\lambda_n})^2[\cos\alpha\sin\beta-\sin^2(\theta_0+\Delta\theta_n)\cos(\varphi_0+\Delta\varphi_n)\sin\beta\cos(\varphi_0+\Delta\varphi_n-\alpha) \\ -\sin(\theta_0+\Delta\theta_n)\cos(\theta_0+\Delta\theta_n)\cos(\varphi_0+\Delta\varphi_n)\cos\beta] \end{array}\right\} \quad (4.6)$$

With multiple measurements at different wavelengths, a set of non-linear equations can be generated and then solved for phase retardation δ_0 and linear birefringence optical axis (φ_0, θ_0). Compare Eqs. 4.5 and 4.6, we see that in the non-null measurement, a linear term of phase retardation (δ_0) appears in the signal, the variation of $\Delta\varphi_n$ and $\Delta\theta_n$ is not just quadratic but rather linear with respect to δ_0.

4.3 SNR ANALYSIS

To estimate the SNR of the polarization microscope system, we assume parameters as below:

P_0: power of the source incident on the circular area with inscribed field (W);

η: Quantum efficiency of the detector;

F: Frame rate of the imager (Hz);

N: pixel number for the imager in one dimension;

τ : integration period of the array in fractions of a frame;

λ: wavelength of the source (m);

δ: phase retardation of the specimen (radian);

c: speed of light (m/s);

h: Plank's constant (m^2kg/s).

For a null measurement, assume shot noise dominates and specimen is placed at the orientation or the incident polarization is adjusted to give the maximum signal, the estimated SNR can be written as:

$$SNR = \left(\frac{P_0 \lambda \eta \tau \delta^2}{2\pi hcFN^2} \right)^{1/2} \tag{4.7}$$

Using the following values to estimate SNR:

η: Quantum efficiency of the detector (70%);

F: Frame rate of the imager (100 Hz);

N: pixel number for the imager in one dimension (256);

τ : integration period of the array in fractions of a frame (0.5);

λ: wavelength of the source (0.515 μm);

δ: phase retardation of the specimen (8.54×10^{-4} radian);

c: speed of light (3×10^8 m/s);

h: Plank's constant (6.63×10^{-34} m^2kg/s).

$$SNR = p_o^{1/2} * 126.72 \tag{4.8}$$

With 4 mW P_0, the SNR could be 8.01.

According to Eq. 4.6, for a non-null measurement, the signal is

$$\begin{aligned} S_0 &= S_a + S_b + S_c \\ S_a &= \frac{1}{2}(1-\sin\beta\cos\alpha) \\ S_b &= \frac{1}{2}\delta_0[\cos\theta_0\sin\alpha\sin\beta - \sin\theta_0\sin\varphi_0\cos\beta] \\ S_c &= \frac{1}{4}\delta_0^2[\cos\alpha\sin\beta - \sin^2\theta_0\cos\varphi_0\sin\beta\cos(\varphi_0-\alpha) - \sin\theta_0\cos\theta_0\cos\varphi_0\cos\beta] \end{aligned} \tag{4.9}$$

As δ_0 is small, the quadratic term S_c can be ignored, the signal is S_b; the primary shot noise comes from background S_a. SNR can be written as

$$SNR \approx \left(\frac{2P_0\lambda\eta\tau}{\pi hcFN^2}\right)^{1/2}\left(\frac{S_b}{(S_a+S_b)^{1/2}}\right) \tag{4.10}$$

When assume $\beta=\pi/2$, α is close to 0, which corresponds to the condition that the incident light's Stokes vector is slightly off the Q axis with an angle of α on QU plane.

$$\frac{S_b}{(S_a+S_b)^{1/2}} = \frac{\frac{1}{2}\delta_0\cos\theta_0\sin\alpha}{\sqrt{\frac{1}{2}(1-\cos\alpha)+\frac{1}{2}\delta_0\cos\theta_0\sin\alpha}} \approx \frac{\alpha\delta_0\cos\theta_0}{\sqrt{\alpha^2+2\alpha\delta_0\cos\theta_0}} \tag{4.11}$$

When θ_0 is close to 0, SNR for a non-null measurement reaches its maximum value

$$SNR_{\max} \approx \left(\frac{2P_0\lambda\eta\tau\delta_0^2}{\pi hcFN^2}\frac{\alpha}{\alpha+2\delta_0}\right)^{1/2} \tag{4.12}$$

Use the same values for null measurement, the SNR for non-null measurement is 16.03 under the assumption that ($\alpha \gg \delta_0$).

Eq. 4.7 and Eq. 4.12 suggest that under the assumed condition, non-null measurement has a higher SNR (approximately 2 folds) than traditional null measurement.

4.4 Features of Polarization Microscope

Several important features guided this polarization microscope system to harness the power of polarized light microscopy.

The first feature is the ability to modulate the polarization state of incident light over the entire Poincaré sphere. As discussed in section 4.2, with the first retarder-rotator combination, the Stokes vector of the incident light first rotates around U axis by retarder, and then rotator provides another rotation around V axis; by these two orthogonal rotations the polarization state of light incident on specimen can be adjusted to achieve any polarization state. Secondly, the system can be developed to image at high speed with high numerical precision and high resolution by combining high wavelength-tuning-rate light source and a high quality CCD camera. Thirdly, the system can be operated for both null and non-null measurement, and as demonstrated in section 4.3, when the phase retardation introduced by specimen is small, a non-null measurement tends to improve the SNR.

4.5 Conclusion on Polarization Microscope Study

In this study, a spectrally-encoded high-extinction polarization microscope is designed for birefringence measurement of biological sample. The polarization microscope system is able to introduce any incident polarization state onto the specimen by a retarder-rotator combination. The processing algorithm is developed to estimate the phase retardation introduced by specimen based on changing amplitude of signal when sample is illuminated by different spectral components of the light. The system can be operated for both null and non-null measurement; processing algorithm is developed for

both cases. A signal-to-noise ratio analysis demonstrates the SNR advantage for a non-null measurement.

References

1. Huang D, Swanson EA, Lin CP, Schuman JS, Stinson WG, Chang W, et al. Optical coherence tomography. Science. 1991;254(5035):1178.
2. Fercher AF, Hitzenberger CK, Kamp G, El-Zaiat SY. Measurement of intraocular distances by backscattering spectral interferometry. Optics Communications. 1995;117(1):43-8.
3. Ha G, Lindner MW. "Coherence Radar" and "Spectral Radar"—New Tools for Dermatological Diagnosis. journal of Biomedical Optics. 1998;3(1):21-31.
4. Danielson BL, Whittenberg CD. Guided-wave reflectometry with micrometer resolution. Appl Opt. 1987;26(14):2836-42.
5. Wieser W, Biedermann BR, Klein T, Eigenwillig CM, Huber R. Multi-Megahertz OCT: High quality 3D imaging at 20 million A-scans and 4.5 GVoxels per second. Opt Express. 2010;18(14):14685-704.
6. Adler DC, Chen Y, Huber R, Schmitt J, Connolly J, Fujimoto JG. Three-dimensional endomicroscopy using optical coherence tomography. Nature Photonics. 2007;1(12):709-16.
7. Leitgeb R, Hitzenberger C, Fercher A. Performance of fourier domain vs. time domain optical coherence tomography. Optics Express. 2003;11(8):889-94.
8. Sorin WV, Baney DM. A simple intensity noise reduction technique for optical low-coherence reflectometry. Photonics Technology Letters, IEEE. 1992;4(12):1404-6.
9. Goodman JW. Statistical optics. New York, Wiley-Interscience, 1985, 567 p. 1985;1.
10. Born M, Wolf E. Principles of Optics, seventh expanded edition. Cambridge, England. 1999.
11. Maitland D, Walsh Jr J. Quantitative measurements of linear birefringence during heating of native collagen. Lasers in surgery and medicine. 1997;20(3):310-8.
12. Bragg WL, Pippard AB. The form birefringence of macromolecules. Acta Crystallographica. 1953;6(11-12):865-7.
13. Ruiz ROaT. Birefringence of macromolecules Wiener's theory revisited, with applications to DNA and tobacco mosaic virus. Biophysical Journal. 1989.
14. Huang X-R, Knighton RW. Microtubules contribute to the birefringence of the retinal nerve fiber layer. Investigative ophthalmology & visual science. 2005;46(12):4588-93.
15. Weinreb RN, Bowd C, Zangwill LM. Glaucoma detection using scanning laser polarimetry with variable corneal polarization compensation. Archives of ophthalmology. 2003;121(2):218.
16. Bagga H, Greenfield DS, Feuer W, Knighton RW. Scanning laser polarimetry with variable corneal compensation and optical coherence tomography in normal and glaucomatous eyes. American journal of ophthalmology. 2003;135(4):521-9.
17. Mohammadi K, Bowd C, Weinreb RN, Medeiros FA, Sample PA, Zangwill LM. Retinal nerve fiber layer thickness measurements with scanning laser polarimetry predict

glaucomatous visual field loss. American journal of ophthalmology. 2004;138(4):592-601.
18. Carmeliet P, Jain RK. Angiogenesis in cancer and other diseases. Nature. 2000;407(6801):249-57.
19. Carmeliet P. Angiogenesis in life, disease and medicine. Nature. 2005;438(7070):932-6.
20. Hee MR, Huang D, Swanson EA, Fujimoto JG. Polarization-sensitive low-coherence reflectometer for birefringence characterization and ranging. J Opt Soc Am B. 1992;9(6):903-8.
21. de Boer JF, Milner TE, van Gemert MJC, Nelson JS. Two-dimensional birefringence imaging in biological tissue by polarization-sensitive optical coherence tomography. Opt Lett. 1997;22(12):934-6.
22. Saxer CE, de Boer JF, Park BH, Zhao Y, Chen Z, Nelson JS. High-speed fiber based polarization-sensitive optical coherence tomography of in vivo human skin. Opt Lett. 2000;25(18):1355-7.
23. Park B, Saxer C, Srinivas S, Nelson J, de Boer J. In vivo burn depth determination by high-speed fiber-based polarization sensitive optical coherence tomography. journal of Biomedical Optics. 2001;6:474.
24. Cense B, Chen TC, Park BH, Pierce MC, de Boer JF. In vivo depth-resolved birefringence measurements of the human retinal nerve fiber layer by polarization-sensitive optical coherence tomography. Opt Lett. 2002;27(18):1610-2.
25. Davé DP, Akkin T, Milner TE. Polarization-maintaining fiber-based optical low-coherence reflectometer for characterization and ranging of birefringence. Opt Lett. 2003;28(19):1775-7.
26. Götzinger E, Baumann B, Pircher M, Hitzenberger CK. Polarization maintaining fiber based ultra-high resolution spectral domain polarization sensitive optical coherence tomography. Opt Express. 2009;17(25):22704-17.
27. Al-Qaisi MK, Akkin T. Swept-source polarization-sensitive optical coherence tomography based on polarization-maintaining fiber. Opt Express. 2010;18(4):3392-403.
28. Park B, Pierce M, Cense B, de Boer J. Jones matrix analysis for a polarization-sensitive optical coherence tomography system using fiber-optic components. Optics letters. 2004;29:2512-4.
29. Park BH, Pierce MC, Cense B, de Boer JF. Optic axis determination accuracy for fiber-based polarization-sensitive optical coherence tomography. Opt Lett. 2005;30(19):2587-9.
30. Kemp N, Zaatari H, Park J, Rylander III H, Milner T. Depth-resolved optic axis orientation in multiple layered anisotropic tissues measured with enhanced polarization-sensitive optical coherence tomography (EPS-OCT). Optics Express. 2005;13(12):4507-18.
31. Yamanari M, Makita S, Yasuno Y. Polarization-sensitive swept-source optical coherence tomography with continuous source polarization modulation. Opt Express. 2008;16(8):5892-906.

32. Park J, Kemp NJ, Rylander HG, Milner TE. Complex polarization ratio to determine polarization properties of anisotropic tissue using polarization-sensitive optical coherence tomography. Opt Express. 2009;17(16):13402-17.
33. Elmaanaoui B, Wang B, Dwelle JC, McElroy AB, Liu SS, Rylander HG, et al. Birefringence measurement of the retinal nerve fiber layer by swept source polarization sensitive optical coherence tomography. Opt Express. 2011;19(11):10252-68.
34. Baumann B, Choi W, Potsaid B, Huang D, Duker JS, Fujimoto JG. Swept source / Fourier domain polarization sensitive optical coherence tomography with a passive polarization delay unit. Opt Express. 2012;20(9):10229-41.
35. Torzicky T, Marschall S, Pircher M, Baumann B, Bonesi M, Zotter S, et al. Retinal polarization-sensitive optical coherence tomography at 1060 nm with 350 kHz A-scan rate using an Fourier domain mode locked laser. journal of Biomedical Optics. 2013;18(2):026008-.
36. Götzinger E, Pircher M, Geitzenauer W, Ahlers C, Baumann B, Michels S, et al. Retinal pigment epithelium segmentation by polarization sensitive optical coherence tomography. Optics Express. 2008;16(21):16410-22.
37. de Boer JF, Milner TE. Review of polarization sensitive optical coherence tomography and Stokes vector determination. journal of Biomedical Optics. 2002;7:359.
38. Santhanam K. Clock System Design for quadrupling the frequency of Reference Clock for a Swept Source Spectral Domain Optical Coherence Tomography. master thesis. 2009.
39. Park J, Kemp N, Zaatari H, Rylander III H, Milner T. Differential geometry of normalized Stokes vector trajectories in anisotropic media. JOSA A. 2006;23(3):679-90.
40. Liu S, Wang B, Yin B, Milner TE, Markey MK, McKinnon SJ, et al. Retinal Nerve Fiber Layer Reflectance for Early Glaucoma Diagnosis. Age (y). 2013;54(7.60):65.56-6.39.
41. Torzicky T, Pircher M, Zotter S, Bonesi M, Götzinger E, Hitzenberger CK. Automated measurement of choroidal thickness in the human eye by polarization sensitive optical coherence tomography. Opt Express. 2012;20(7):7564-74.
42. Mujat M, Park BH, Cense B, Chen TC, de Boer JF. Autocalibration of spectral-domain optical coherence tomography spectrometers for in vivo quantitative retinal nerve fiber layer birefringence determination. journal of Biomedical Optics. 2007;12:041205.
43. Yamanari M, Miura M, Makita S, Yatagai T, Yasuno Y. Phase retardation measurement of retinal nerve fiber layer by polarization-sensitive spectral-domain optical coherence tomography and scanning laser polarimetry. journal of Biomedical Optics. 2008;13:014013.
44. Götzinger E, Pircher M, Baumann B, Hirn C, Vass C, Hitzenberger C. Retinal nerve fiber layer birefringence evaluated with polarization sensitive spectral domain OCT and scanning laser polarimetry: a comparison. Journal of biophotonics. 2008;1(2):129-39.
45. Gordon J, Kogelnik H. PMD fundamentals: Polarization mode dispersion in optical fibers. Proceedings of the National Academy of Sciences. 2000;97(9):4541-50.
46. Zhang EZ, Vakoc BJ. Polarimetry noise in fiber-based optical coherence tomography instrumentation. Opt Express. 2011;19(18):16830-42.

47. Villiger M, Zhang EZ, Nadkarni S, Oh W-Y, Bouma BE, Vakoc BJ. Artifacts in polarization-sensitive optical coherence tomography caused by polarization mode dispersion. Opt Lett. 2013;38(6):923-5.
48. Zhang EZ, Oh W-Y, Villiger ML, Chen L, Bouma BE, Vakoc BJ. Numerical compensation of system polarization mode dispersion in polarization-sensitive optical coherence tomography. Opt Express. 2013;21(1):1163-80.
49. Pocock GM, Aranibar RG, Kemp NJ, Specht CS, Markey MK, Rylander HG. The relationship between retinal ganglion cell axon constituents and retinal nerve fiber layer birefringence in the primate. Investigative ophthalmology & visual science. 2009;50(11):5238-46.
50. Dwelle J, Liu S, Wang B, McElroy A, Ho D, Markey MK, et al. Thickness, phase retardation, birefringence, and reflectance of the retinal nerve fiber layer in normal and glaucomatous non-human primates. Investigative ophthalmology & visual science. 2012;53(8):4380-95.
51. Ju W-K, Liu Q, Kim K-Y, Crowston JG, Lindsey JD, Agarwal N, et al. Elevated hydrostatic pressure triggers mitochondrial fission and decreases cellular ATP in differentiated RGC-5 cells. Investigative ophthalmology & visual science. 2007;48(5):2145-51.
52. Pasternack RM, Zheng JY, Boustany NN. Detection of mitochondrial fission with orientation‐dependent optical Fourier filters. Cytometry Part A. 2011;79(2):137-48.
53. Chalut KJ, Ostrander JH, Giacomelli MG, Wax A. Light scattering measurements of subcellular structure provide noninvasive early detection of chemotherapy-induced apoptosis. Cancer research. 2009;69(3):1199-204.
54. van der Meer FJ, Faber DJ, Aalders MC, Poot AA, Vermes I, van Leeuwen TG. Apoptosis-and necrosis-induced changes in light attenuation measured by optical coherence tomography. Lasers in Medical Science. 2010;25(2):259-67.
55. Farhat G, Mariampillai A, Yang VX, Czarnota GJ, Kolios MC. Detecting apoptosis using dynamic light scattering with optical coherence tomography. journal of Biomedical Optics. 2011;16(7):070505--3.
56. Pyhtila J, Graf R, Wax A. Determining nuclear morphology using an improved angle-resolved low coherence interferometry system. Optics Express. 2003;11(25):3473-84.
57. Zhu Y, Terry NG, Wax A. Scanning fiber angle-resolved low coherence interferometry. Optics letters. 2009;34(20):3196-8.
58. Giacomelli MG, Chalut KJ, Ostrander JH, Wax A. Review of the application of T-matrix calculations for determining the structure of cell nuclei with angle-resolved light scattering measurements. Selected Topics in Quantum Electronics, IEEE Journal of. 2010;16(4):900-8.
59. Zhu Y, Giacomelli MG, Wax A. Fiber-optic interferometric two-dimensional scattering-measurement system. Optics letters. 2010;35(10):1641-3.
60. Giacomelli M, Zhu Y, Lee J, Wax A. Size and shape determination of spheroidal scatterers using two-dimensional angle resolved scattering. Optics Express. 2010;18(14):14616-26.

61. Klein T, André R, Wieser W, Pfeiffer T, Huber R. Joint aperture detection for speckle reduction and increased collection efficiency in ophthalmic MHz OCT. Biomed Opt Express. 2013;4(4):619-34.
62. Kim E, Dave D, Milner TE. Fiber-optic spectral polarimeter using a broadband swept laser source. Optics Communications. 2005;249(1–3):351-6.
63. Kim E, Milner TE. Fiber-based single-channel polarization-sensitive spectral interferometry. J Opt Soc Am A. 2006;23(6):1458-67.
64. Linsenmeier R, Yancey C. Effects of hyperoxia on the oxygen distribution in the intact cat retina. Investigative ophthalmology & visual science. 1989;30(4):612-8.
65. Padnick-Silver L, Derwent JJK, Giuliano E, Narfström K, Linsenmeier RA. Retinal oxygenation and oxygen metabolism in Abyssinian cats with a hereditary retinal degeneration. Investigative ophthalmology & visual science. 2006;47(8):3683-9.
66. Yu D-Y, Cringle SJ, Su E-N. Intraretinal oxygen distribution in the monkey retina and the response to systemic hyperoxia. Investigative ophthalmology & visual science. 2005;46(12):4728-33.
67. Glud R, Ramsing N, Gundersen J, Klimant I. Planar optrodes: a new tool for fine scale measurements of two-dimensional O~ 2 distribution in benthic communities. Marine Ecology-Progress Series. 1996;140:217-26.
68. Yu C, Boyd N, Cringle S, Alder V, Yu D. Oxygen distribution and consumption in rat lower incisor pulp. Archives of oral biology. 2002;47(7):529-36.
69. Cheng H, Nair G, Walker TA, Kim MK, Pardue MT, Thulé PM, et al. Structural and functional MRI reveals multiple retinal layers. Proceedings of the National Academy of Sciences. 2006;103(46):17525-30.
70. Berkowitz BA, Kowluru RA, Frank RN, Kern TS, Hohman TC, Prakash M. Subnormal retinal oxygenation response precedes diabetic-like retinopathy. Investigative ophthalmology & visual science. 1999;40(9):2100-5.
71. Duong TQ, Pardue MT, Thule PM, Olson DE, Cheng H, Nair G, et al. Layer‐specific anatomical, physiological and functional MRI of the retina. NMR in biomedicine. 2008;21(9):978-96.
72. Ungerleider LG. Functional MRI evidence for adult motor cortex plasticity during motor skill learning. Nature. 1995;377:155-8.
73. Koopmans PJ, Barth M, Norris DG. Layer‐specific BOLD activation in human V1. Human brain mapping. 2010;31(9):1297-304.
74. Denninghoff KR, Smith MH, Lompado A, Hillman LW. Retinal venous oxygen saturation and cardiac output during controlled hemorrhage and resuscitation. Journal of Applied Physiology. 2003;94(3):891-6.
75. Hammer M, Schweitzer D. Quantitative reflection spectroscopy at the human ocular fundus. Physics in Medicine and Biology. 2002;47(2):179.
76. Madsen PL, Secher NH. Near-infrared oximetry of the brain. Progress in neurobiology. 1999;58(6):541-60.
77. Sowa MG, Mansfield JR, Scarth GB, Mantsch HH. Noninvasive assessment of regional and temporal variations in tissue oxygenation by near-infrared spectroscopy and imaging. Applied spectroscopy. 1997;51(2):143-51.

78. Dunn AK, Devor A, Bolay H, Andermann ML, Moskowitz MA, Dale AM, et al. Simultaneous imaging of total cerebral hemoglobin concentration, oxygenation, and blood flow during functional activation. Optics letters. 2003;28(1):28-30.
79. Izhaky D, Nelson DA, Burgansky-Eliash Z, Grinvald A. Functional imaging using the retinal function imager: direct imaging of blood velocity, achieving fluorescein angiography-like images without any contrast agent, qualitative oximetry, and functional metabolic signals. Japanese journal of ophthalmology. 2009;53(4):345-51.
80. Shonat RD, Kight AC. Oxygen tension imaging in the mouse retina. Annals of biomedical engineering. 2003;31(9):1084-96.
81. Zuckerman R, Cheasty JE, Wang Y. Optical mapping of inner retinal tissue PO2. Current eye research. 1993;12(9):809-25.
82. Golub AS, Tevald MA, Pittman RN. Phosphorescence quenching microrespirometry of skeletal muscle in situ. American Journal of Physiology-Heart and Circulatory Physiology. 2011;300(1):H135-H43.
83. Tsai AG, Friesenecker B, Mazzoni MC, Kerger H, Buerk DG, Johnson PC, et al. Microvascular and tissue oxygen gradients in the rat mesentery. Proceedings of the National Academy of Sciences. 1998;95(12):6590-5.
84. Lo L-W, Koch CJ, Wilson DF. Calibration of oxygen-dependent quenching of the phosphorescence of Pd-meso-tetra (4-carboxyphenyl) porphine: a phosphor with general application for measuring oxygen concentration in biological systems. Analytical biochemistry. 1996;236(1):153-60.
85. Helmlinger G, Yuan F, Dellian M, Jain RK. Interstitial pH and pO2 gradients in solid tumors in vivo: high-resolution measurements reveal a lack of correlation. Nature medicine. 1997;3(2):177-82.
86. Robles F, Graf RN, Wax A. Dual window method for processing spectroscopic optical coherence tomography signals with simultaneously high spectral and temporal resolution. Opt Express. 2009;17(8):6799-812.
87. Leitgeb R, Wojtkowski M, Kowalczyk A, Hitzenberger CK, Sticker M, Fercher AF. Spectral measurement of absorption by spectroscopic frequency-domain optical coherence tomography. Opt Lett. 2000;25(11):820-2.
88. Faber DJ, van Leeuwen TG. Are quantitative attenuation measurements of blood by optical coherence tomography feasible? Opt Lett. 2009;34(9):1435-7.
89. Yi J, Li X. Estimation of oxygen saturation from erythrocytes by high-resolution spectroscopic optical coherence tomography. Optics letters. 2010;35(12):2094-6.
90. Robles FE, Wilson C, Grant G, Wax A. Molecular imaging true-colour spectroscopic optical coherence tomography. Nature Photonics. 2011;5(12):744-7.
91. Adler DC, Huang S-W, Huber R, Fujimoto JG. Photothermal detection of gold nanoparticlesusing phase-sensitive optical coherencetomography. Opt Express. 2008;16(7):4376-93.
92. Skala MC, Crow MJ, Wax A, Izatt JA. Photothermal optical coherence tomography of epidermal growth factor receptor in live cells using immunotargeted gold nanospheres. Nano letters. 2008;8(10):3461-7.

93. Paranjape AS, Kuranov R, Baranov S, Ma LL, Villard JW, Wang T, et al. Depth resolved photothermal OCT detection of macrophages in tissue using nanorose. Biomed Opt Express. 2010;1(1):2-16.
94. Kuranov RV, Qiu J, McElroy AB, Estrada A, Salvaggio A, Kiel J, et al. Depth-resolved blood oxygen saturation measurement by dual-wavelength photothermal (DWP) optical coherence tomography. Biomed Opt Express. 2011;2(3):491-504.
95. Kuranov RV, Kazmi S, McElroy AB, Kiel JW, Dunn AK, Milner TE, et al. In vivo depth-resolved oxygen saturation by dual-wavelength photothermal (DWP) OCT. Opt Express. 2011;19(24):23831-44.
96. Kuranov RV, McElroy AB, Kemp N, Baranov S, Taber J, Feldman MD, et al. Gas-Cell Referenced Swept Source Phase Sensitive Optical Coherence Tomography. Photonics Technology Letters, IEEE. 2010;22(20):1524-6.
97. Rollins AM, Izatt JA. Optimal interferometer designs for optical coherence tomography. Opt Lett. 1999;24(21):1484-6.
98. Vakoc B, Yun S, de Boer J, Tearney G, Bouma B. Phase-resolved optical frequency domain imaging. Opt Express. 2005;13(14):5483-93.
99. Wojtkowski M, Srinivasan V, Ko T, Fujimoto J, Kowalczyk A, Duker J. Ultrahigh-resolution, high-speed, Fourier domain optical coherence tomography and methods for dispersion compensation. Opt Express. 2004;12(11):2404-22.
100. Wu T, Ding Z, Wang L, Chen M. Spectral phase based k-domain interpolation for uniform sampling in swept-source optical coherence tomography. Optics Express. 2011;19(19):18430-9.
101. Briely-Sabo K, A B. Accurate de-oxygenation of ex vivo whole blood using sodium Dithionite. Proc Intl Sot Mag Reson Med. 2000;8:2025.
102. Ma YP, Koo A, Kwan HC, Cheng KK. On-line measurement of the dynamic velocity of erythrocytes in the cerebral microvessels in the rat. Microvascular Research. 1974;8(1):1-13.
103. Binzoni T, Leung TS, Boggett D, Delpy D. Non-invasive laser Doppler perfusion measurements of large tissue volumes and human skeletal muscle blood RMS velocity. Physics in Medicine and Biology. 2003;48(15):2527.
104. Milner TE, Goodman DM, Tanenbaum BS, Anvari B, Nelson JS. Noncontact determination of thermal diffusivity in biomaterials using infrared imaging radiometry. journal of Biomedical Optics. 1996;1(1):92-7.
105. Wang W-H, Meng L, Hackett RJ, Odenbourg R, Keefe DL. Limited recovery of meiotic spindles in living human oocytes after cooling–rewarming observed using polarized light microscopy. Human Reproduction. 2001;16(11):2374-8.
106. Kuhn JR, Wu Z, Poenie M. Modulated polarization microscopy: a promising new approach to visualizing cytoskeletal dynamics in living cells. Biophysical Journal. 2001;80(2):972-85.
107. Oldenbourg R. Analysis of edge birefringence. Biophysical Journal. 1991;60(3):629-41.

Vita

Biwei Yin was born in Fuzhou, Fujian, China in August, 1985, as the son of Junqin Yin and Suyan Zhang. Biwei graduated from Fuzhou No. 1 Middle School in 2004 and graduated from Zhejiang University in 2008, where he received a Bachelor's degree in optical engineering. In fall 2008, Biwei moved to the United States and started his graduate study in the University of Texas at Austin. He was in the Ph.D. program of Electrical and Computer Engineering and worked as a graduate research assistant under the supervision of Dr. Thomas E. Milner throughout the period of his graduate study. His research focused on development and application of optical coherence tomography technique. He earned his Master of Science degree in Electrical and Computer Engineering in 2010.

Email: biwei.yin@gmail.com
This dissertation was typed by Biwei Yin.